The turbulent/non-turbulent interface of a round jet

Measurements on a large range of Reynolds numbers

L.E. van Dalen

Technical University Delft

Master thesis Mechanical Engineering
Energy, Flow and Process Technology track

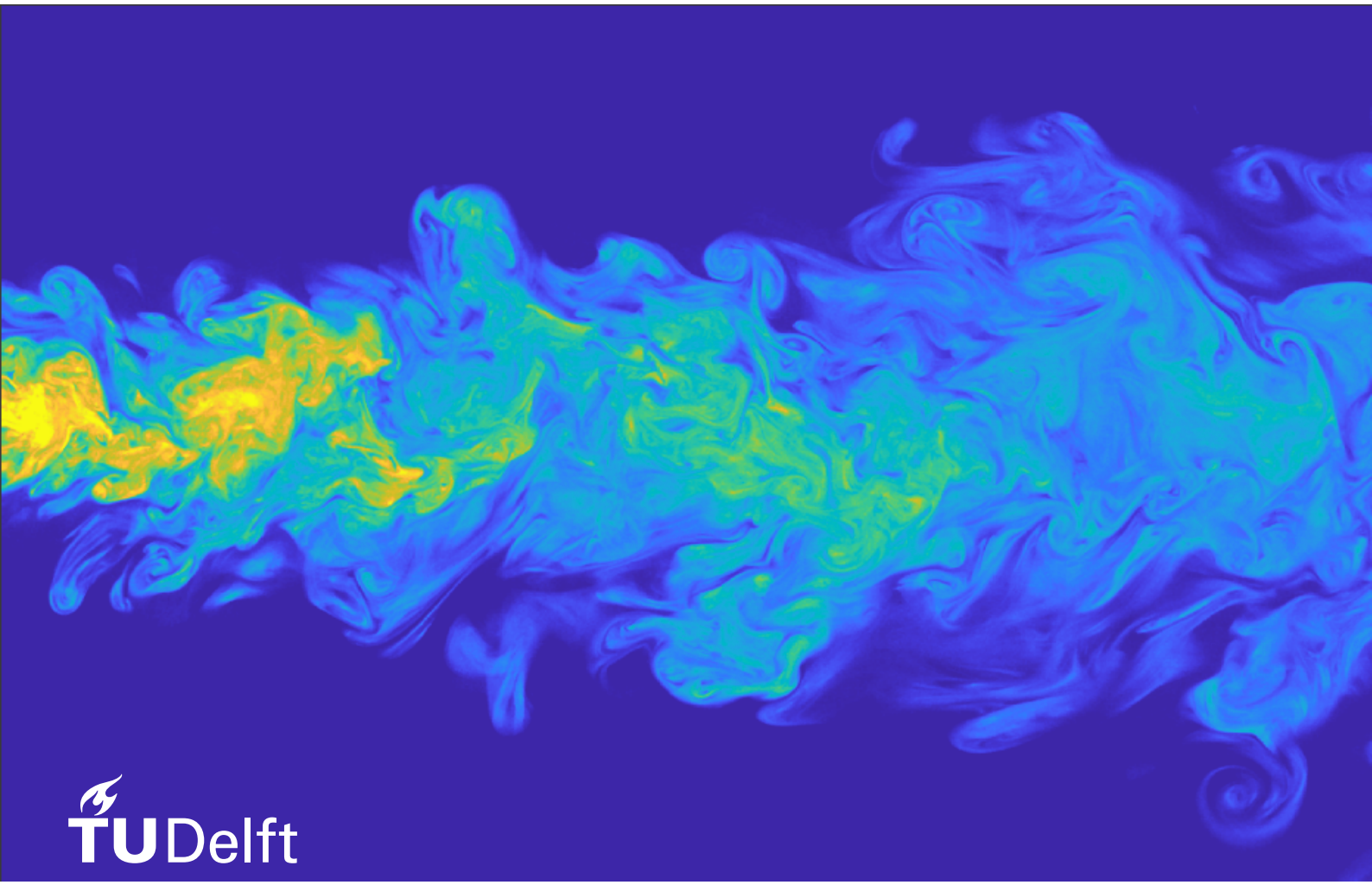

TU Delft

The turbulent/non-turbulent interface of a round jet

Measurements on a large range of Reynolds numbers

by

L.E. van Dalen

to obtain the degree of Master of Science
at the Delft University of Technology,
to be defended publicly on Wednesday April 20, 2022 at 14:00.

Student number:	4487680	
Thesis committee:	Prof. dr. ir. J. Westerweel,	TU Delft, supervisor
	Prof. dr. ir. W. van de Water,	TU Delft, supervisor
	Dr. ir. R. Pecnik	TU Delft, committee member

TU Delft

Acknowledgements

This thesis has been achieved with help from a lot of different people.
First, I would like to thank my supervisors Jerry and Willem, for providing thorough feedback throughout the thesis. Their supervision has helped me gain insight and think critically about the subject, choices I made, my writing and the whole process of doing research.

The experimental setup and measurements could not have been done without the help from different people around the lab. I want to thank Edwin, Gertjan, Jasper and Jan for spending a lot of effort and time in me and my setup; helping me with anything I needed in the lab. Whether it was something practical related to my setup, or just answering one of the many questions.

Furthermore I would like to thank everyone else I had discussions with about the subject. Sometimes a small (or big...) comment or just a listening rubber duck can help move on or solve an issue.

My friends and family are a big part of this, and helped me a lot during this time. I can't thank them enough for the support I've gotten and for being by my side these months.

Lyke van Dalen
Delft, April 2022

Abstract

In this thesis a method of combined PIV and LIF experiments on the Turbulent/Non-Turbulent interface (TNTI) of a round jet is presented.
By varying the distance from the nozzle in the measurements, the Kolmogorov scale of a large range of Reynolds number ($2 \times 10^3 \leq Re \leq 48 \times 10^3$) is kept constant, allowing for a constant resolution. The large range in Reynolds number is needed to identify a difference in scaling of the TNTI, which is difficult to capture due to the weak dependency of the separation of Kolmogorov and Taylor scales on the Reynolds number ($\lambda/\eta \sim Re^{1/4}$). A factor of over 2.5 is achieved in the current work.

An experimental setup for these measurements is presented, as well as the design of experiments for seven Reynolds numbers based on the boundary and initial conditions of the setup. A design for measurements with a camera moving with the flow is presented as well.
Conditional statistics are used on the jet to look at the change of span-wise vorticity over the interface. For the detection of the interface scalar images from LIF are used, where the interface is detected using a threshold of dye concentration (Rhodamine B).
All Reynolds numbers show self-similarity within the measured range, comparable to literature and with a spatial resolution better than 4η. Some small differences between the low and high Reynolds number measurements can be seen. They are not expected to have significant impact on the results and can likely be solved by slight changes in the experimental setup.

The influence of the threshold on the shape and width measurements of the mean conditional vorticity profile is examined, indicating a significant dependency on chosen threshold. Current results indicate a scaling of the interface thickness with the Taylor length scale, around a value of 0.5-0.6λ, or 10-15η. This is in accordance to the literature for low Reynolds numbers. Due to this significant influence of the threshold on the outcome, these results cannot be seen conclusive. For this, further investigation is needed on the dependency of the width on the threshold, and validation of the jet contour.

Universal ways to compute the threshold, jet contour and mean conditional vorticity profiles are currently missing, while they have shown to be potentially of significance on the outcome. Another method of studying TNTI scaling is via the local velocity scales, which can be found via current data, which could provide a comparison of methods. The measurements with the moving camera could help identifying the link between physical processes and the scaling of the interface.

Contents

Nomenclature

Latin Symbols & Acronyms

B_u	Decay rate parameter	[-]
$C_{\max}$	Maximum concentration for linearity of Rhodamine B	g/L
C_{p}	Particle source concentration	g/L
C_{source}	Rhodamine B source concentration	g/L
D_{n}	Nozzle diameter	m
FOV	Field Of View	m
K_u	Spreading rate	[-]
M_0	Image magnification	[-]
N_{F}	Number of frames in the dataset	[-]
Q	Volume flow	m^3/s
$r_{1/2}$	Jet half-width	m
Re	Reynolds number	[-]
TNTI	Turbulent/Non Turbulent Interface	
u'	Velocity fluctuations	m/s
U_{c}	Centerline velocity	m/s
U_{n}	Velocity at the nozzle	m/s
x_0	Virtual origin	m
X_{n}	Distance from nozzle in x-direction	m
y_{i}	Location of the interface	m
Y_{n}	Distance from nozzle in y-direction	m

Greek symbols

Δt	Time between two laser pulses	s
Δx	Vector spacing	m
ϵ	Dissipation	$\mathrm{m}^2/\mathrm{s}^3$
η	Kolmogorov length scale	m
ϕ	Threshold of concentration	g/L
λ	Taylor length scale	m
ν	Kinematic viscosity	m^2/s
ω_z	Out-of-plane instantaneous vorticity field	1/s

1 Introduction

In this thesis, the interface of a round submerged jet is investigated. Turbulent jets can be seen in many applications; think about discharge from pipes or plumes in air, but also more industrial applications like fuel injection in engines. The characteristics of these flows are highly dependent on their geometry, environment, and fluid properties.
Since jets are widely used in mixing applications it is important to study the interaction between a jet and its surrounding fluid. This interaction takes place at the interface between them, which is studied in this thesis.

1.1 Description of a submerged round jet

To quantify the turbulent jet the Reynolds number (Re) is used. For a submerged axisymmetric free jet, the Reynolds number is constant due to the preservation of momentum and can be quantified by the Reynolds number at the nozzle, [32]

$$Re = \frac{U_\mathrm{n} D_\mathrm{n}}{\nu}, \tag{1.1}$$

where D_n [m] is the diameter of the nozzle, U_n [m/s] the mean velocity of the fluid at the nozzle, and ν the kinematic viscosity of the fluid [m^2/s].
An important quality of a jet is its so-called *self-similarity*. Once developed, the scaled radial velocity profile becomes independent of the distance from the nozzle [32]. Before this self-similar region of the jet, there is a development region, as can be seen in Figure 1. The start of this self-similar region is assumed around $30D_\mathrm{n}$, but can differ based on initial and boundary conditions [33, 35, 45, 58]. For a jet bounded by walls, as in this research, the self-similarity of the jet ends at a certain distance from the nozzle and the region has shown to last up to $160D_\mathrm{n}$ in practice [33, 35, 45, 58].
As a jet spreads outwards and its cross section increases, the centerline velocity decreases with the distance from the nozzle according to, [6]

$$\frac{U_\mathrm{c}(x)}{U_\mathrm{n}} = \frac{B_u D_\mathrm{n}}{x - x_0}, \tag{1.2}$$

where $U_\mathrm{c}(x)$ is the centerline velocity, x the distance from the nozzle, and x_0 the virtual jet origin. The constant B_u is called the decay constant (of the velocity) and its value depends on the initial and boundary conditions [6]. The location of the virtual origin x_0 generally lies around 0.5-$10D_\mathrm{n}$ as indicated by experimental data [32].
Using the self-similarity of a jet the radial dependence of the streamwise velocity can be computed at a location x, [6]

$$\frac{U(r,x)}{U_c(x)} = \exp\left(-K_u \left(\frac{r}{x - x_0}\right)^2\right), \tag{1.3}$$

where $U(r,x)$ is the velocity at a distance r from the centerline. This is under the assumption of a Gaussian velocity profile, which is an approximation not uncommonly used in literature [6, 16, 21, 55].
The factor K_u is, again, specific for each jet and determined by initial and boundary conditions. The half-width of the jet is noted by $r_{1/2}$ and is defined by the distance r at which the velocity is equal to $\frac{1}{2}U_\mathrm{c}$. This is assumed to be the large-scale length scale of the flow of the jet. Note that the spreading of the jet and decay of the jet centerline velocity are theoretically independent of Re, and thus B_u and K_u purely differ due to a difference in initial or boundary conditions. A summary of different experimental values for B_u, K_u, and x_0 can be found in Table 9, where they are compared to the constants found in this research.
While a jet is spreading it takes in fluid from outside, a process also known as *entrainment* [32]. This entrainment takes place at the edge of the jet (the interface), where it is in contact with the surrounding non-turbulent fluid. This interface has shown to be a sharp boundary and is called the Turbulent/Non-Turbulent Interface (TNTI) [12].

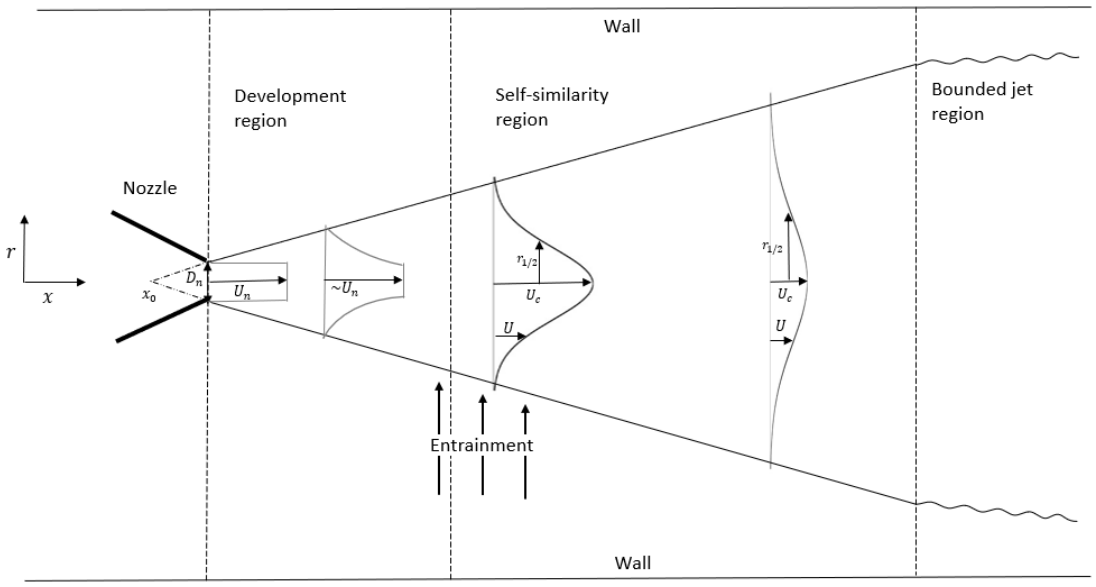

Figure 1: The different regions within a round jet. Showed is the development of the radial velocity profile in streamwise direction x. Including a representation of virtual origin x_0, nozzle diameter D_n, the exit velocity at the nozzle U_n and half-width $r_{1/2}$. Note that the image is not on scale.

1.2 The turbulent/non turbulent interface (TNTI)

The turbulent/non-turbulent interface has been a subject of research for years. Due to the complex nature of entrainment, there are still some uncertainties about the processes at the interface, with the scaling of the TNTI thickness still being unknown. Discovering more about the interface can provide more insight in, for example, mixing processes and possible improvement of mixing. Apart from being present at jets, a similar TNTI can also be found at wakes and mixing layers.

By assuming that the surrounding of the jet is irrotational (i.e. it has zero vorticity) the TNTI is the edge of an irrotational region and a jet, which has a large jump in vorticity. The distinction of jet and non-jet fluid can thus be done by stating that if the fluid is irrotational it belongs to the outer region, and vice versa. In that way entraining of a fluid parcel means it gains vorticity. The outward movement of the TNTI can then be seen as spreading of vorticity. The gaining of vorticity by fluid parcels outside the jet is usually described by two processes called *engulfment* and *nibbling* [27, 54]. Engulfment refers to an inviscid process. It involves large scale ingestion of irrotational fluid by enclosing it within the domain of the jet [12]. Nibbling is a smaller-scale viscous process along the entire boundary of the jet. It has been a point of discussion which of these processes is dominant in different occurrences of the TNTI. Up until recently, it was assumed that engulfment is the primary mechanism. However, recent studies have indicated that for a round jet, which we examine, nibbling is the dominating process [27, 54]. A schematic of these processes can be seen in Figure 2a. Influenced by the working processes at the interface is the thickness. For this, it is still uncertain whether this scales with the Taylor or Kolmogorov scale, defined later in this chapter. The primary way of conducting experiments to measure entrainment or thickness are performed statically.

In order to do measurements on the interface, it has to be detected first. This can be challenging due to the intermittent behaviour of turbulence but can be done in different ways. An interface *envelope* can be defined, representing the contour of the outer extension of the interface [12, 54]. An example of an envelope can be found in Figure 2a. Identifying the location of the envelope can be done in different ways. Since there is no vorticity on the irrotational side of the interface, a threshold of vorticity can be applied to define the jet and non-jet fluid. This method is straightforward, but to accurately determine the vorticity, three-dimensional velocity data is necessary, which is not always a possibility [54]. A solution for this is using a threshold for kinetic energy. The change of kinetic energy, however, is more gradual than that of vorticity, causing a smoother profile and less accurate representation of the interface [8]. Another possibility is a scalar that is advected with the turbulent flow. The most common scalars used for this are temperature differences or a dye. The difficulty is ensuring that the scalar does not diffuse further than momentum, something which is difficult to achieve by using a temperature difference due to high thermal diffusivity of water [54]. The diffusivity of a scalar is usually

described by the Schmidt number (Sc),

$$Sc = \frac{\nu}{\mathcal{D}}, \tag{1.4}$$

where ν is the kinematic viscosity, representing the momentum diffusivity, and $\mathcal{D}$ the diffusivity of mass [35]. In this research it has been chosen to use a dye, Rhodamine B, with Sc equal to 2×10^3 [16]. When using temperature difference, the diffusivity of temperature as scalar is described using the Prandtl number, which is equivalent to the Schmidt number in this case.
Recent studies have shown that inside the envelope of the jet there is a region or layer in which the vorticity and streamwise velocity have a sharp jump in value, from the inside of the jet to the irrotational region. The distance over which this jump ΔU is spread is assumed as the thickness of the layer. This layer is referred to as the TNTI, with the thickness of the layer being the scale of the interface. Another name for this layer is the turbulent sublayer [12]. The jump can also be measured in terms of vorticity, which is what is done in this research, following a method close to that of Ref. [54]. The small amount of vorticity present before the jump is introduced is due to viscous diffusion. Sometimes this layer is referred to as the superlayer, and its thickness is presumably of the order of the smallest length scale of turbulence, the Kolmogorov scale η [12].

To visualize this jump, conditional statistics on the interface are used. By looking at the properties of the flow with respect to the envelope, much sharper gradients in flow variables can be found [12]. Due to the large-scale intermittency of the jet, classical statistics based on large-scale flow conditions smoothen the jump. An example of this difference in the vorticity profile at the interface can be seen in Figure 2b.

Turbulence, and thus the TNTI, is characterized by several length scales. Before, the half-width of the jet is defined, which is the macroscopic length scale of the flow. The Kolmogorov scale η is at the smallest, defined as the size of the smallest eddies [32],

$$\eta = \left(\frac{\nu^3}{\epsilon}\right)^{1/4}, \tag{1.5}$$

where ϵ is the dissipation rate in $\mathrm{m}^2/\mathrm{s}^3$. The Taylor scale λ is an intermediate scale, and the largest of the dissipative scales, [35, 45]

$$\lambda_\mathrm{T}^2 = \frac{15\nu\overline{u'^2}}{\epsilon}, \tag{1.6}$$

where u' are the velocity fluctuations.
As of now, there are a lot of theories on the scaling and behaviour of this interface, some supported by experiments. However, the dependence of the interface on numerous quantities like Reynolds number, flow type, and initial conditions is still unknown [12].

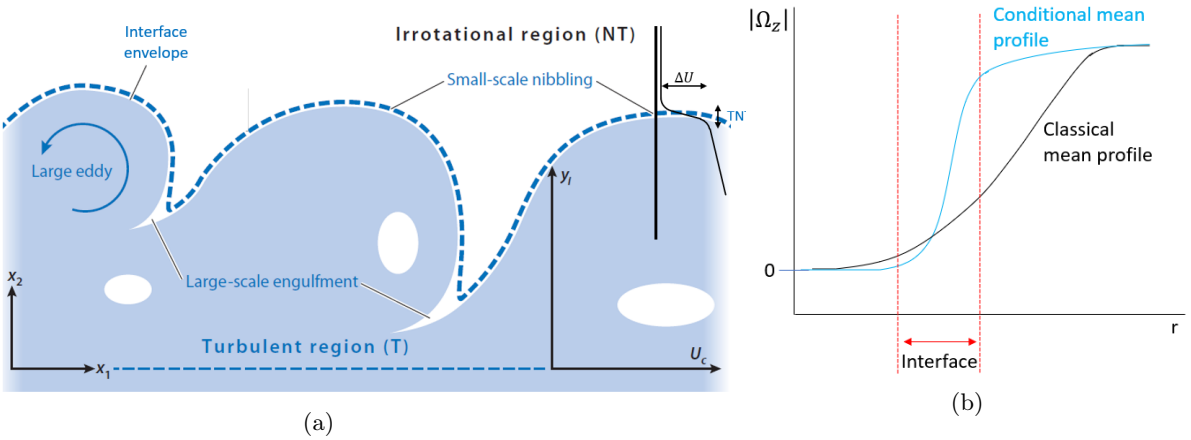

Figure 2: **(a)** A schematic representation of the TNTI. Indicating engulfment, nibbling and the interface envelope at distance y_i from the centerline of the jet. The velocity jump ΔU over the interface can also be seen in the top right. Adjusted from Ref. [12] **(b)** Schematic representation of the difference in vorticity jump achieved by classical statistics based on large-scale flow conditions relative to a fixed location (e.g. the jet centerline) and the conditional profile relative to the TNTI.

1.3 Aim of the research

As stated before, there are still many uncertainties and unknowns with regard to the turbulent/non-turbulent interface. In this thesis, some light is shed on the behaviour and processes at the TNTI of a submerged round turbulent jet.
One focus is the behaviour of the TNTI at different Reynolds numbers, specifically the thickness of the interfacial layer. Most previous research on the interface of jets has been in the lower Reynolds number regime, where the Kolmogorov (η) and Taylor (λ) scales are much closer together than at higher Reynolds numbers. Due to the weak dependence of the ratio of scales on the Reynolds numbers, $\lambda/\eta \sim Re^{1/4}$, a difference of a factor 2 in this ratio needs a factor $2^4 = 16$ difference in range of Reynolds number. Thus to find a dependency on either of those scales, a large range of Reynolds numbers is needed.

Experimental data on round jets at low Reynolds numbers has been obtained, using the vorticity jump to measure the thickness. Ref. [54] found the thickness to be approximately 1.1λ at $Re = 2000$ [43, 54]. Using a similar approach Ref. [23] found a thickness close to 0.5λ at $x = 25D_\mathrm{n}$ for $Re = 3000 - 6500$.
Looking at moderate Reynolds numbers Ref. [17] has done measurements up to $Re = 18440$ in the developing region of the jet ($x \leq 20D_\mathrm{n}$) [17]. They found that the thickness scales with the Taylor scale λ. The focus here however lies on the thickness of the scalar jump in combination with a relatively high diffusivity of the scalar ($\mathrm{Sc} = 0.7$). In other applications, it has been shown that this combination can lead to a different thickness than by using a vorticity jump [4].
Experiments on round jets above $Re = 18440$ have not been performed yet, which inspired the current research.

The interface of plane jets and mixing layers has been studied more extensively, mostly using DNS. Previous research on these other type of flows has shown that in cases with no mean shear the thickness of the layer scales with the Kolmogorov scale [20], indicating that shear has a meaningful influence on the thickness of the interface.
Ref. [43] found via DNS that for increasing Reynolds number the thickness of the interface of a plane jet scales with η dedicating this to the fragmentation of eddies at higher Reynolds numbers [43]. They found a continuous thickness of around 10η, linking this to the assumption that the thickness is equal to the length scale of vortical structures in the vicinity of the interface [42]. This scaling with η would be achieved above a Taylor Reynolds number $Re_\lambda > 200$,

$$Re_\lambda = \frac{u_\mathrm{rms}\lambda}{\nu}, \tag{1.7}$$

where new parameter u_rms is the root mean square of the velocity. $Re_\lambda = 200$ corresponds to Re of $2{\times}10^4$ for a round jet.
Extending this finding, a change in scaling could be expected for round jets at high Reynolds numbers as well. This thesis reports on the scaling of the interface at a larger range of Reynolds numbers than has been done before on a round jet. The measurements are done at a similar Kolmogorov scale for all Reynolds numbers, which, due to the self-similarity of the jet, is possible by measuring closer or further away from the nozzle. This way it is ensured that the flow field at all Reynolds numbers can be resolved, but also that any change in scaling will not be caused by a change in the Kolmogorov scale. If little difference in profiles can be found, indicating scaling with η, this would indicate some form of universality of the interface, and it thus being potentially uncorrelated to multiple other flow features.
As briefly mentioned before, a challenging aspect of the examination of the thickness of the interface is the weak dependence of the separation of scales on the Reynolds numbers. The ratio $\frac{\lambda}{\eta}$ scales with $Re^{1/4}$, meaning that we need a very large range in Reynolds numbers to find a difference or a dependence on either of these scales [32]. This large range in Reynolds numbers is very often a challenge to achieve experimentally due to the decrease in η as Re increases when measuring at a single location. With this research, a set of experiments is designed to achieve a large range in Reynolds numbers experimentally, while keeping η constant. Therefore our focus will be on the dependence of the TNTI characteristics on λ.

PIV and LIF measurements are performed simultaneously on a submerged round jet. By using the concentration field from the LIF results, the position of the interface can be determined [30, 36, 54]. The PIV results are used to determine the flow field and vorticity. With help of conditional statistics relative to the detected interface, the jump in vorticity per Re can be determined and potential changes in scaling identified.

A second part of the thesis describes Lagrangian measurements, that is, moving along with the interface as it is moving outward and further away from the nozzle. By doing Lagrangian measurements a specific part of the interface can be followed, visualizing the processes happening simultaneously and subsequently at the interface.

This is a very different approach than was used previously and the focus is not directly on the statistics or quantification of the TNTI, but merely on visualization. Following Ref. [54] the nibbling process consist of eddies formed by the shear layer and eddy transport. The forming and transport of these eddies, but also the engulfment process, could be captured. With the length scales of the flow changing during the measurement, but the camera moving along, it will be possible to visualize these structures close to the interface and potentially their influence.
These measurements also exist of PIV and LIF simultaneously, but now with a camera moving along with the part of the interface that we want to capture. In this thesis, only the design and processing of these measurements is explained, due to time constraints.

An outline of the Thesis is as follows: The design for both of these measurements is explained in Chapter 4. Before that, a visualisation of a jet is done in Chapter 2 to estimate constants B_u, K_u, and x_0 which are needed to estimate the constraints and further the design of the measurements. The experimental setup is described in 3. The methodology, or data processing, is explained in Chapter 5. Results will be presented in Chapter 6 and conclusion and recommendations in Chapter 7.

2 Visualization

First, a visualization is done of the setup used in Ref. [37] and Ref. [38]. This gives us an idea of the parameters K_u, B_u and x_0, that characterize the jet. Note however that another setup is used in our experiment, meaning that the initial conditions of the jet change with respect to this visualisation. For the visualization, methylene blue was used, which is added to the water emitted through the nozzle. The visualization is filmed using a camera (GoPro 4) on a stand that is aligned with the tank in which the jet flow is created. The tank is $0.6 \times 0.6 \times 2$ m^3 and information about the setup can be found in Ref. [37] and Ref. [38].
The jet Reynolds number is determined by the nozzle diameter D_n and the volume flow rate Q through the nozzle.
Q is measured in two different ways: First the height is measured that the water in the tank has increased during some time. The error of this measurement is estimated using the accuracy of the ruler, 0.05 cm, and time measurements, 0.2 s [10, 15]. Secondly the time is measured to pump 2L out of the reservoir by reading the volume change from the bucket from which the water is pumped from. Assuming a similar time measurement error and an volume error of 0.05L due to the reading scale of the bucket being 0.1L, the error can be estimated. These two measurements differ by 8%, and the estimated error differs only a factor 5, so the average volume flow of these two measurements is used. The error for the reading of the nozzle diameter is assumed to be 0.05 mm [10].
Using $U_n = \frac{Q}{\frac{\pi}{4}D_n^2}$, U_n can be determined. Following Equation (1.1) the Reynolds number of the jet can be found, assuming the literary value for the kinematic viscosity at 20°C of 1×10^{-6} m^2/s [22]. The parameters can be found in Table 1.

Table 1: Values of the parameters of the jet used for the visualization.

Parameter	**Value**	**Error**
Q [m^3/s]	1.2×10^{-5}	$\pm\ 0.14\times10^{-5}$
D_n [m]	4×10^{-3}	$\pm\ 0.05\times10^{-3}$
U_n [m/s]	0.94	$\pm$ 0.06
Re [-]	3.8×10^{3}	$\pm\ 0.2\times10^{3}$
ν [m^2/s]	1×10^{-6}	-

First a general overview of the visualisation is made by averaging 300 snapshots from $t = 0$ to $t = 290s$, which is the total duration of the video. The contrast of the jet and the background is not very clear, mainly when the concentration of the dye gets less at the end of the tank; an effect that is probably also amplified by mixing. To increase the contrast, the image is cropped and the colours of the video re-scaled. The raw averaged image and the image after cropping and re-scaling can be found in Figure 3. The jet starts at $t = 5.6$ s and reaches the end wall around $t = 150$ s.

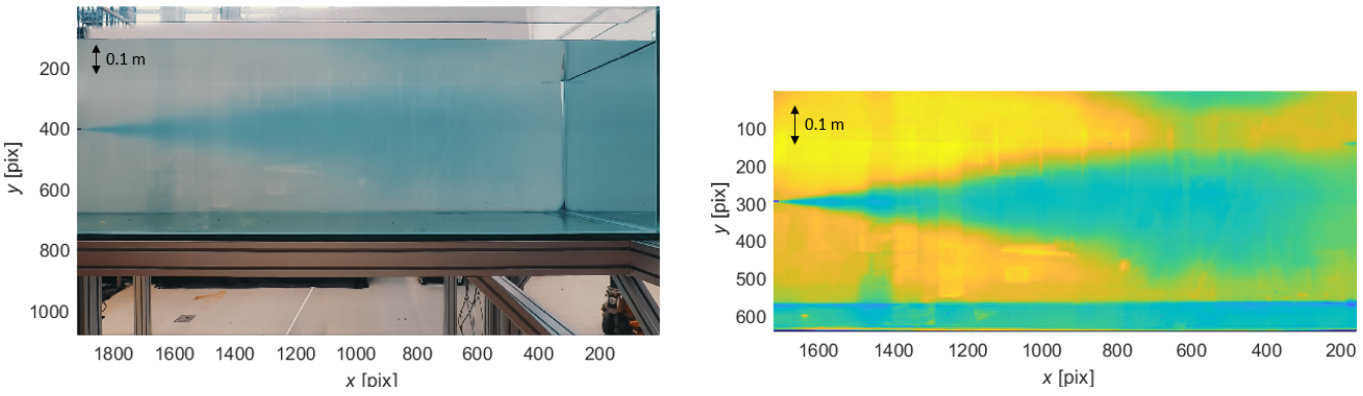

(a) (b)

Figure 3: The visualization video is averaged using 300 snapshots from from $t = 0$ to $t = 290s$ of the jet with $Re = 3.8 \times 10^3$. **(a)** The raw averaged image **(b)** To increase the contrast, the raw image is cropped and the colours are re-scaled.

Looking at Figure 3 it can be seen that the jet does not appear symmetric in this case. This is probably also caused by a small offset of the nozzle, which is located closer to the free surface. At the surface, the jet visually does not seem to be influenced much until the point where the surface is reached. For the lower side of the jet, the shape deviates earlier. This potentially is influenced by the difference in boundary conditions. The surface being shear free, and the bottom with. Some darker and lighter vertical regions can also be seen in both images, distorting the image and potentially giving a non-representative average. In chapter 6 it is shown using PIV there is indeed an asymmetry in the jet.
To translate the pixels of the camera to meters, three known distances are measured in pixels and compared to their actual measurements. The distance from the nozzle to the end of the tank, the height of the tank, and the diameter of the nozzle in pixels and meters are used to calculate an average of 9.8×10^{-4} meters per pixel.

For this first characterization of the jet x_0, K_u and B_u are estimated. These are preferably measured in the self-similar region, with the highest contrast and far away from the boundaries, which is why only the first part of the jet is used.

2.1 Virtual origin and spreading rate

First the virtual origin x_0 and spreading rate K_u are determined. This is done by taking 300 snapshots between 20 (where the contrast is of suffcient level) and 100 seconds (to limit the effects of mixing and the end wall) and averaging them. The range can be seen in Figure 4. It can be noted that the same darker and lighter regions as in Figure 3 deform the appearance of the jet edge. When selecting the interface location these regions are thus avoided.
By extrapolating the function in Figure 4 and converting the coordinates to meters, the intersection with the height of the nozzle (thus virtual origin x_0) can be found at $x_0 = 14.4 \pm 0.7\mathrm{mm} = 3.6 \pm 0.2 D_n$. This result is in correspondence to the literature value in Table 9.
To find the spreading rate K_u of the jet, the half-width of the jet is computed. This is done by assuming that the position of the average jet edge is comparable to the position of the jet interface, y_i. It is assumed $y_\mathrm{i} = 1.93 r_{1/2}$ via Ref. [54] and Equation (1.3) is used to find K_u. The spreading rate K_u can then be found as $\mathrm{K}_u = 73.1 \pm 4.0$. Comparing this to the literature in Table 9 the present value is somewhat low, indicating that the jet is wider. Considering the error this value doesn't seem very odd, but still on the lower side. This is an unusual outcome since with the presence of sidewalls the opposite would be expected [32]. This might be due to the method of determining the interface location, as well as $\mathrm{r}_{1/2}$, which are only indicative. Comparing it to the values found with PIV in Chapter 6 for Cases 2 and 3 (see Tables 2 and 9), this trend of a relative low K_u does seem to be representative of the jets in the final experiments, considering the Reynolds number being closest to Case 3.

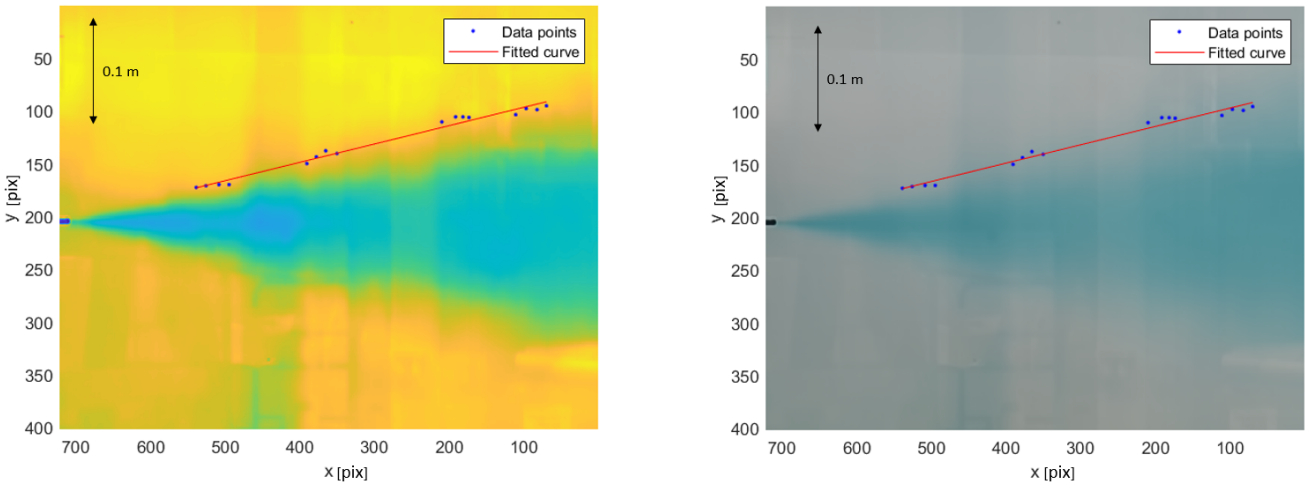

(a) (b)

Figure 4: **(a)** The jet up to $x = 176 D_\mathrm{n}$. The position at the interface is detected at 15 locations between $x = 0.166$ ($41.5 D_n$) to $x = 0.6257$ ($156 D_n$), outside of the deformed regions. A linear fit of $y = 0.1738x + 79.38$ [pix] represents the interface of the jet, at the adapted image **(b)** The interface is verified using the raw image.

2.2 Decay constant

To determine the decay constant snapshots are taking from the video. An example of these snapshots can be found in Figure 5. Since the measurements are taken of a jet entering a tank with stagnant water it will give us different results than an already moving jet.
Ref. [40] and [48] show that the velocity of a jet front is around half of the maximum fluid velocity behind the front. Thus it is assumed that the velocity of the front of this jet is half of the velocity within a moving jet. This indicates that the time to reach a certain distance should be scaled with a factor 0.5 to simulate the centerline velocity of a continuous jet. The raw measurements and scaled measurements can be found in Figure 6a. By using the x_0 found previously and Equation (1.2) B_u can be determined. In Figure 6b it can be seen that these measurements imply that B_u is around 5.8 to 6. Using central difference the average velocity can be determined. Using this velocity and Equation (1.2) B_u can be made quantitative by fitting a line through $\frac{1}{U_c} = \frac{1}{B_u U_n D_n}(x - x_0) = 44.56x - 0.1469$, as can be seen in Figure 6c. This estimates $B_u = 5.97 \pm 0.8$. x_0 can also be found from this line and is estimated as $x_0 = 0.0033 \pm 0.08$ or $x_0 = 0.8 \pm 2D_n$. Due to the small number of measurements however, the estimation of the velocity and virtual origin is not very reliable, as can also be seen by the fluctuations in Figure 6d. Therefore a B_u of 5.9 will be assumed based on Figure 6b, which falls within the estimated error and seems to fit better. This can be compared to the B_u found via PIV for the final jets, as can be found in Table 9. This value seem to be lying within the values found for Case 2 and 3, which does match with the Reynolds number.

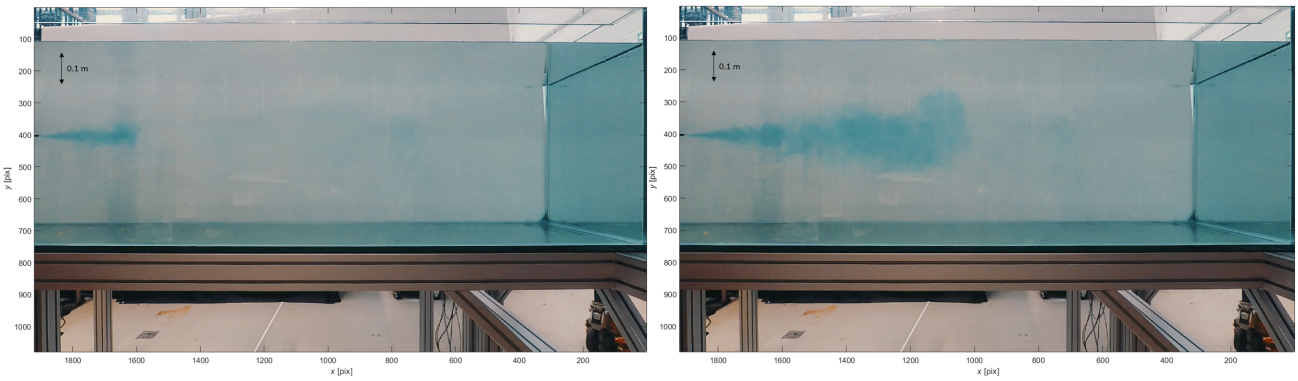

(a) (b)

Figure 5: Example of snapshots taken from the visualisation to determine the decay constant B_u, illustrating the movement of the jet in time. The jet leaves the nozzle at $t_0 = 5.6$ s. Three snapshots are taken between t_0 and 7 s and eight snapshots between 17.5 s and 40 s to stay clear of deformed regions. In each snapshot, the location of the jet that is furthest away from the nozzle is assumed to be the distance it travelled. **(a)** $t = 10$ s **(b)** $t = 40$ s

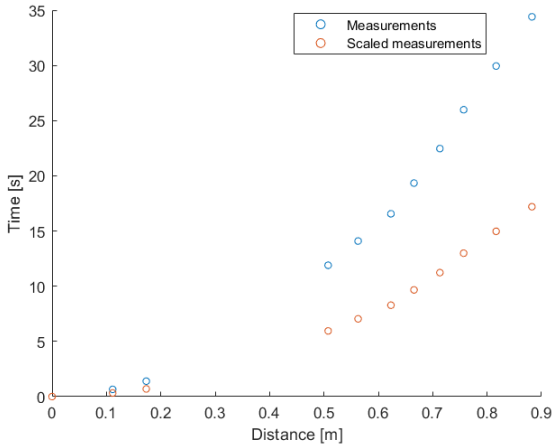

(a)

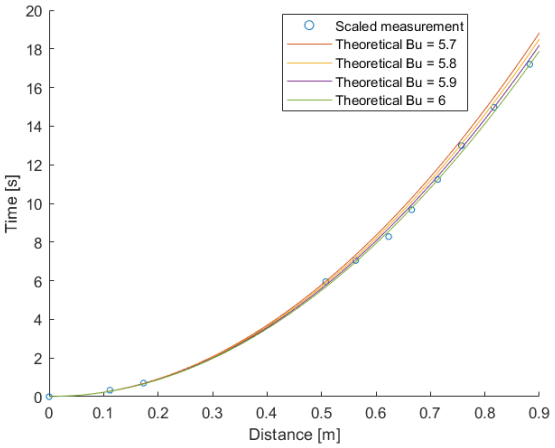

(b)

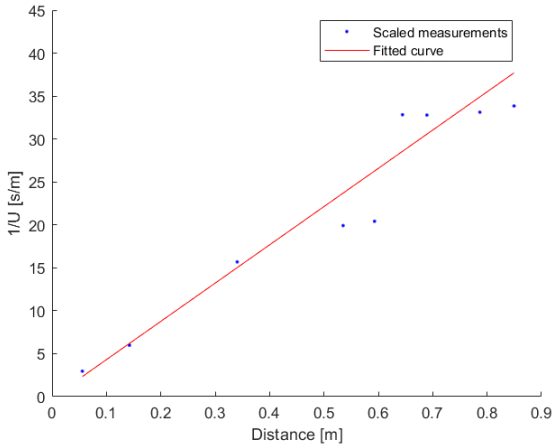

(c)

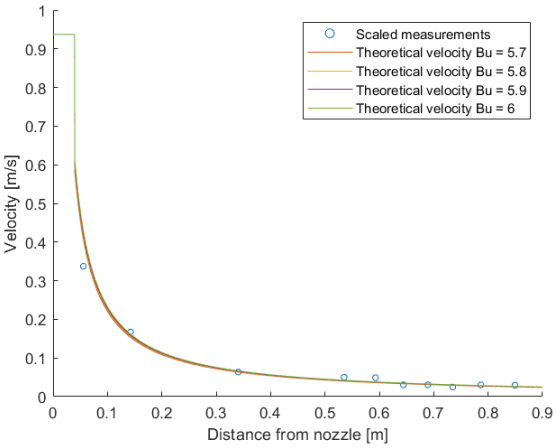

(d)

Figure 6: Results from the measurement done on the jet. **(a)** Raw and scaled measurements of the time it takes from the nozzle to reach a certain distance in the tank **(b)** The scaled measurements together with the theoretical expectation for different B_u. **(c)** The inverse of the estimated velocity using central difference versus distance from the nozzle to obtain B_u. **(d)** The expected velocity for different B_u as comparison to our measurements. Clear fluctuations can be seen in our data.

3 Experimental setup

The design of the experimental setup consists of two parts. First is elaborated on the setup for the supply of the jet and after that on the setup for the PIV/LIF measurements.

3.1 Supply of the jet

3.1.1 Design

To achieve a jet on which measurements can be performed a new setup is built. The measurements are done in a glass tank of size $0.6 \times 0.6 \times 2$ m^3 in which the jet is released. Because of the desired range of Reynolds number a electric centrifugal pump (SAER 32/3) is used to supply the water that is needed [26]. The flow rate can be varied by adjusting the frequency of the pump. The reservoir from which the water is pumped exists of a 60L tank, which is more than enough for multiple measurements and not limiting, as can be seen in Chapter 4.
To link the scaling of the TNTI to the Reynolds number, it is important to know the Reynolds numbers of the jet during the measurements. This is done by placing a flow meter between the pump and the nozzle. For the lower flow rates a turbine flow meter (B.I.O.-Tech FCH-midi-POM) is used with an accuracy of 2%. For the higher flow rates a turbine flow meter with an accuracy of 3% is used (Badger 3012 4F16).
The route to the nozzle can be found in Figure 7b including the dimensions. The length of the straight pipe leading to the nozzle has been chosen equal to the entrance length for turbulent pipe flow L_e. L_e can be found as 0.33 m [57],

$$L_e = 1.6 Re^{1/4} D_{pipe}, \tag{3.1}$$

where inner pipe diameter D_{pipe} is 12 mm, and the maximum Reynolds number at the nozzle ($D_n = 0.01$) is assumed as 1×10^5. As suggested by Ref. [19] the mean pipe velocity profile becomes symmetric again between 20 up to 50 pipe diameters in a similar geometry. The current design would be on the lower side of this, but with spatial constraints a longer pipe length does not seem desirable, as examined in Chapter 4. The asymmetry is further discussed in Chapter 6.
The nozzle is designed as a cone, assuming an angle of 15 degrees with the longitudinal axis and is 3D printed, a schematic representation can be seen in figure 7b. Two different nozzle diameters will be used, $D_n = 0.01$ and $D_n = 0.002$. Since the tank is filled up to 5cm under edge, as seen in Figure 7b, the nozzle was placed off center to have the bottom wall and free surface on equal distance. The empty 5 cm in the tank leaves room in the tank for 60 L, which is equal to the volume of the reservoir. It was decided to not attach anything onto the glass tank to avoid potential stresses in the material.
Since we would like to keep the initial conditions as close together for all Reynolds numbers, but also for practical reasons, it was decided to use the same pump for the lower Reynolds number flow as well. This is done by lowering the volume flow to the nozzle by creating a bypass using needle valves. By adjusting the valves the flow rate towards the nozzle can be managed.
For practicality, but also to avoid the build-up of pressure behind the nozzle, a circulation circuit was designed. Two solenoid valves open and close simultaneously to shift between the path back to the reservoir or the path to the nozzle. In Figure 7a an overview of the setup for the supply of the jet can be found. In Figure 7b the geometry between the solenoid valve and nozzle can be seen.

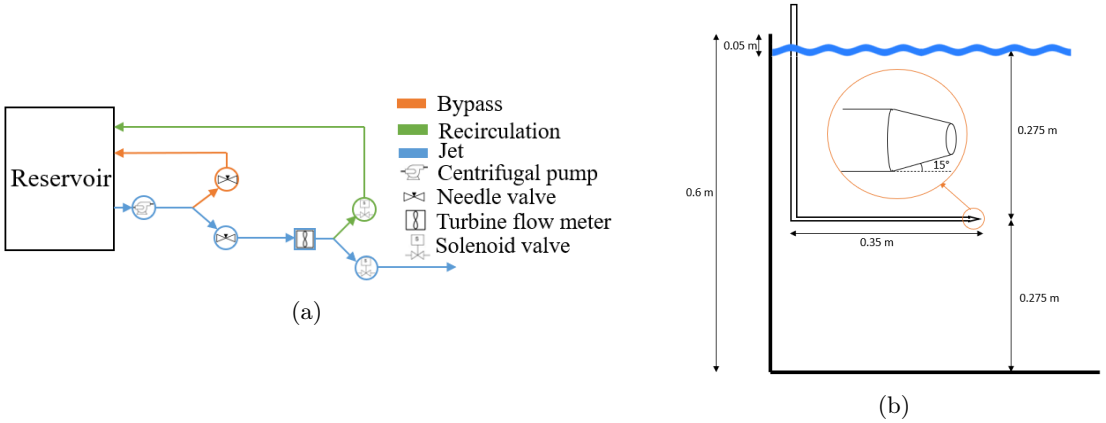

(a) (b)

Figure 7: Design of the supply of the jet. **(a)** Overview of the setup including supply of the jet, recirculation and bypass. **(b)**The geometry after the solenoid valve leading to the nozzle, including dimensions.

3.1.2 Performance

The performance of the setup that supplies the jet is tested by varying the frequency (and thus rotational velocity) of the pump to reach different flow rates, which can be measured using the flow meter.
First the pump characteristics, i.e. the flowrate Q plotted versus the head H of the pump, for different frequencies f are determined. This is done by scaling the pump characteristic for 60 Hz as provided by the manufacturer [26]. Using similarity rules of turbomachinery it can be derived that $\frac{\text{rpm}_2}{\text{rpm}_1} \sim \frac{f_2}{f_1}$, $\frac{Q_2}{Q_1} \sim \frac{\text{rpm}_2}{\text{rpm}_1}$ and $\frac{H_2}{H_1} \sim \left(\frac{\text{rpm}_2}{\text{rpm}_1}\right)^2$ [57]. The pump characteristics for varying frequencies can be found in Figure 8a. By varying the frequency of the pump and reading the flow rate from the flow meter the system characteristic of our setup can be found. This is indicated by the operating point at each frequency; this can be seen in Figure 8b. By assuming D_n = 0.01 m and kinematic viscosity of 1×10^{-6} m^2/s the corresponding Reynolds numbers can be estimated; see Figure 8d. As part of the performance test of the circulation, the system curve was measured and compared to the nozzle system in Figure 8c. It should be noted that there is a slight difference in back pressure between the circulation and the nozzle system. This could mean a slight disturbance in Q when the flow is switched. However, since the difference is minimal, this is assumed not to have any influence on the measured velocity fields. For Reynolds numbers calculations an average Q is used, thus the influence of a difference in back pressure is assumed negligible.

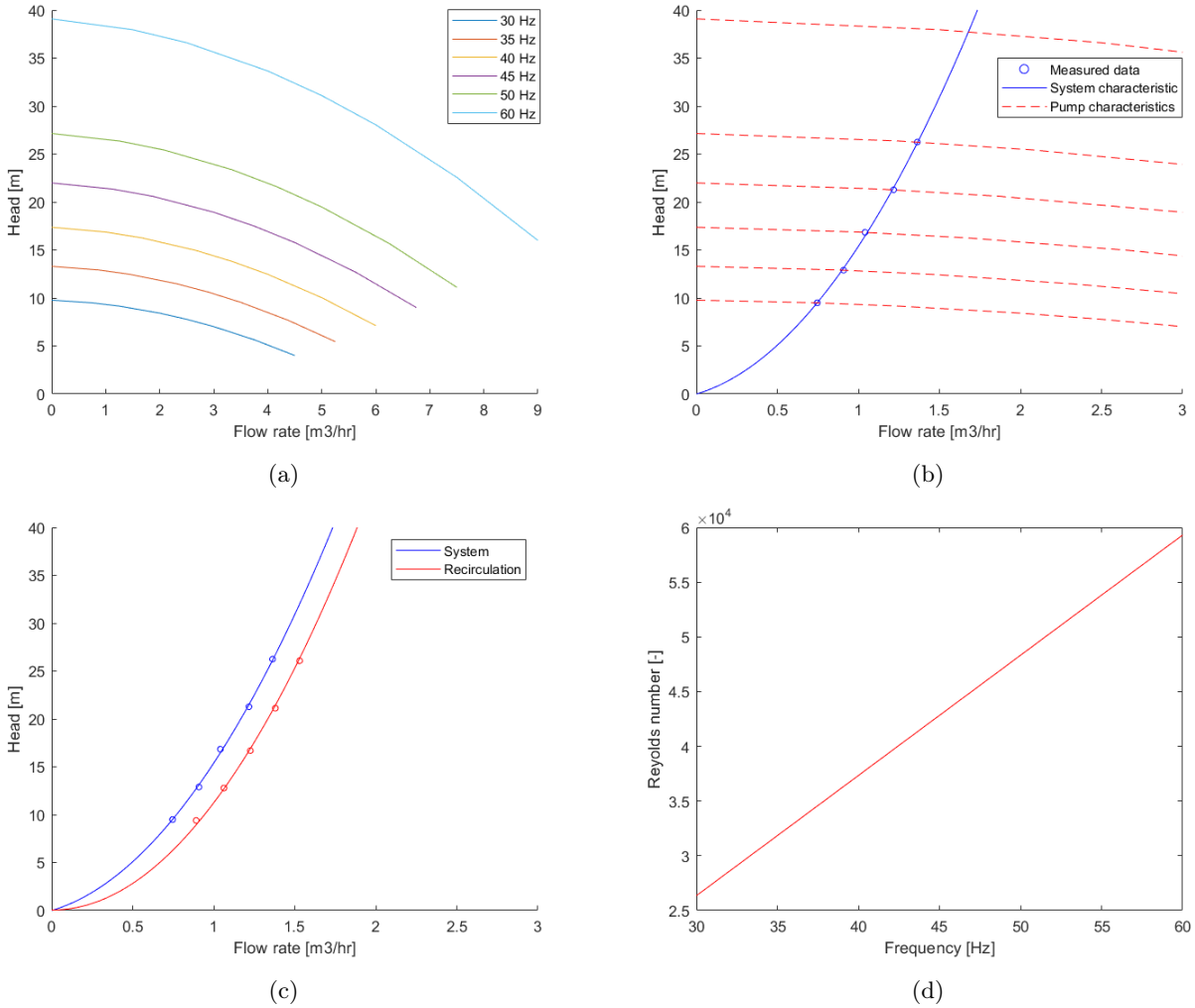

Figure 8: **(a)** The scaled pump characteristics for a load of 50% - 100% on which the present operating points are situated. **(b)** The measured flow rate at the different frequencies super-positioned on the pump characteristics with a fitted curve as the found system characteristic. **(c)** The difference between circulation and the nozzle supply system. This shows that there is less back pressure at the circulation system. **(d)** The estimated Reynolds numbers for given pump. This is estimated using Equation (1.1), $D_\text{n} = 0.01$, $\nu = 1 \times 10^{-6}$ and U_n following from the flow rate.

3.2 Measurement setup

The measurements are done using a double pulsed Nd:YAG laser (Spectra Physics Quanta Ray) which is used to create a sheet from beneath. To position the sheet correctly, three mirrors are used, as can be seen in Figure 9a. In between these mirrors, lenses are used to diverge the laser beam and thinning it in $y-$direction to create a thin laser sheet. The PIV/LIF measurements are performed with two sCMOS-cameras (PCO.edge 5.5, 16-bit, 5 Megapixel). The cameras and the laser are controlled via a PC with Davis 10 via a Programmable Timing Unit. The LIF-camera is positioned 10 cm above the camera used for the PIV measurements on a downward angle of 4 degrees.
The cameras are placed on a traverse mechanism, a construction that can move 2, 1, and 1 meter in respectively x, y, and z direction. The movement is controlled by three stepper motors (MDrive 23 Hybrid, Schneider Electric) via a PC. When performing a measurement with the moving system, the laser is triggered by the position of the traverse to ensure the laser stays at its design frequency of 10 Hz.
During the PIV and LIF measurement, particles and Rhodamine B will enter the tank. To prevent the build-up of these a filter system has been set in place consisting of a pump that passes the water through two filters. First, a 1 μm filter to filter the particles (which have a diameter of 30 μm, Sphericel) and after that a carbon 1 μm filter which can adsorb Rhodamine B [1, 13].

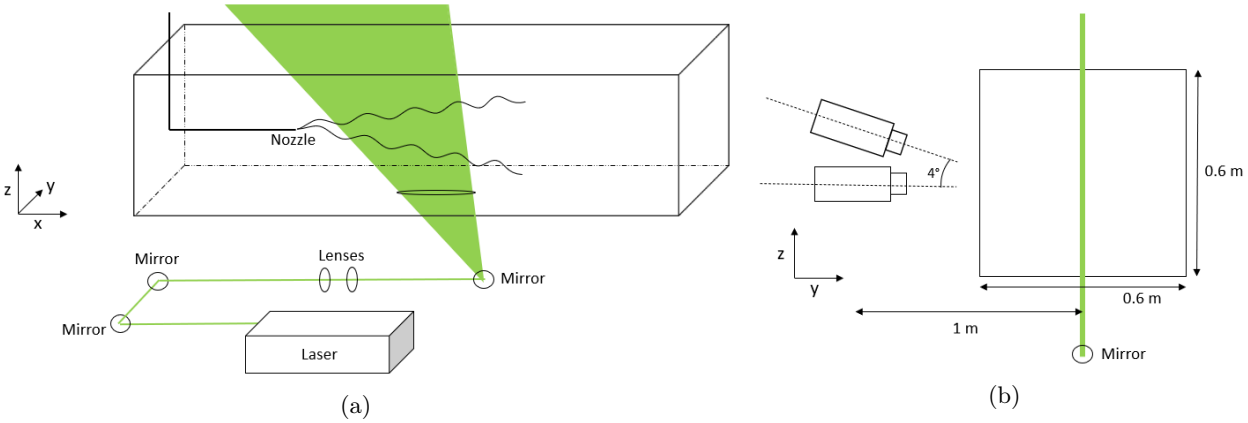

Figure 9: **(a)** Overview of the setup of the laser sheet. From the laser head it is deflected by three mirrors and diverged and thinned by two lenses before entering the water tank in the middle at the bottom. **(b)** The position of the two cameras with respect to the laser sheet.

4 Design PIV/LIF

The design is done using values of B_u of 5.9, $x_0 = 4D_\mathrm{n}$ and K_u of 73 as found in the visualisation in Chapter 2. Reynolds numbers are estimated using a kinematic viscosity ν of $1.0{\times}10^{-6}$ m^2/s.
As mentioned before the intention is to measure at a constant Kolmogorov scale η, thus measuring at a different distance from the nozzle for each Reynolds number. First, it is necessary to look at the constraints on the scales, location, and time of the measurements. First, the extent of the constraints is shown, then an experimental design is proposed, for which the constraints are examined. After this, the final measurements are presented.

4.1 Constraints

4.1.1 Scales

Since all measurements are done around a single value for η at all Reynolds numbers, this already implies some challenges:

- η should occur for the whole range of Reynolds numbers within the distance the jet travels in the tank.
- λ and η should be clearly separated for all Reynolds numbers in order to distinguish them properly.

First the Kolmogorov scale $\eta(x, Re)$ is estimated using Equation (1.5), with ϵ estimated via an empirical relation [33],

$$\epsilon = \frac{0.015 U_\mathrm{c}^3}{r_{1/2}} \tag{4.1}$$

Equations 1.2 and 1.3 can be used to find U_c and $r_{1/2}$. This achieves a range of η in the tank per Reynolds number. The minimum and maximum values per Reynolds number are shown in Figure 10a. By combining Equations (1.5), (1.6), (4.1) and the assumption that $\left(\overline{u'^2}\right)^{1/2} \cong 0.25 U_\mathrm{c}$ at the centerline [33, 54, 58], the separation of the Taylor and Kolmogorov scale can be found as,

$$\frac{\lambda}{\eta} \sim 2.8 \times Re^{1/4} \tag{4.2}$$

and can be seen in Figure 10b.
From Figure 10a it follows that the range of Kolmogorov scales that can be achieved with every Reynolds number is between 1.9×10^{-5} and 1.2×10^{-4} m. The ratio of λ and η seems to be sufficient to accurately separate the scales at all Reynolds numbers. However, for the lower Reynolds number this needs to be verified once the scales are accurately measured.

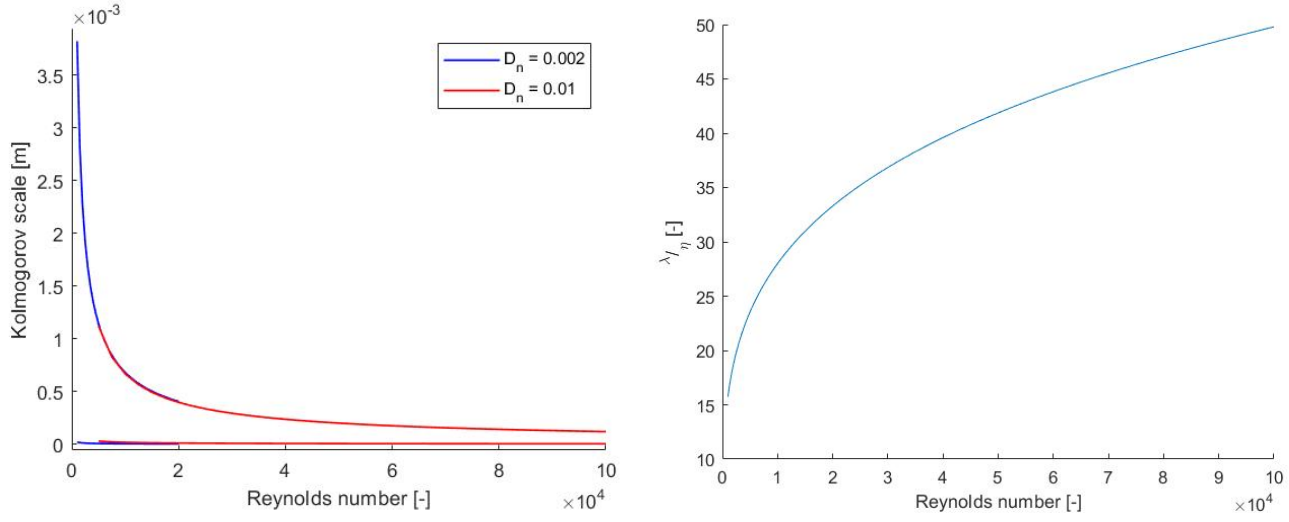

(a) (b)

Figure 10: Constraints of scales within the tank **(a)** The minimum and maximum η per Reynolds number for two different D_n [m] that can be found within the tank. The minimum value occurring at the beginning of the tank and the maximum at the end. **(b)** The estimation of the ratio of the Taylor over Kolmogorov scale per Reynolds number.

4.1.2 Spatial constraints

Since the tank has a finite dimension, this also implies some constraints to ensure the accuracy of our measurement:

- The measurements should be within the self-similar region of the jet.
- The measurements should be sufficiently far away from the end wall to avoid influence of it.
- The location of the interface should be sufficiently far away from the sidewalls and free surface to avoid influence of those.

The self-similar region from the jet can be safely assumed from $40D_\mathrm{n}$ to $140D_\mathrm{n}$. Since the region is dependent on the nozzle diameter, it is different for $D_\mathrm{n} = 0.002$ and $D_\mathrm{n} = 0.01$ m. For both diameters, this region can be found in red in Figure 11. Looking at Figure 11 it can be concluded that for the smaller nozzle diameter all measurements will be far from the end wall and sides. For the nozzle diameter of $D_\mathrm{n} = 0.01$ m the self-similar region is much larger, so it will be necessary consider possible wall effect.
To estimate the distance where the jet will feel an influence of the end wall, the theory of an impinging jet is considered. The distance from the end wall where deflection will occur can be estimated as follows [18],

$$x_\mathrm{deflection} = 0.153\left(1 + \frac{H}{D_\mathrm{n}}\right)D_\mathrm{n}, \quad \text{for } \frac{H}{D_\mathrm{n}} > 6.8, \tag{4.3}$$

where H the total distance from the nozzle to wall. This has been verified for a lower $\frac{H}{D_n}$ compared to the present case and at a Reynolds number of 80.000. It will however give an estimation on the safer side regarding the increased mixing and lower velocity of the present jet.
Influence of the sidewalls can be expected for a jet if $\frac{A_\mathrm{n}}{A_\mathrm{tank}} < 10^{-5}$ affecting the decay and spreading rate of a jet [32]. For $D_\mathrm{n} = 0.01$ m, $\frac{A_\mathrm{n}}{A_\mathrm{tank}} \sim 10^{-3}$, thus an influence on the jet will very likely be present. As long as the effect can be captured in the constants K_u and B_u it is not expected to cause a problem. However, after long times back-flow can be expected, and problems can occur when the interface is close to the sides of the tank. To illustrate this the location of the interface is estimated using $y_\mathrm{i} = 1.93\, r_{1/2}$ and plotted in Figure 11. It can be seen that around $x = 1.6$ m, the interface is very close to the walls. The danger in this is that the entrainment will be disturbed due to the limited fluid available to entrain.

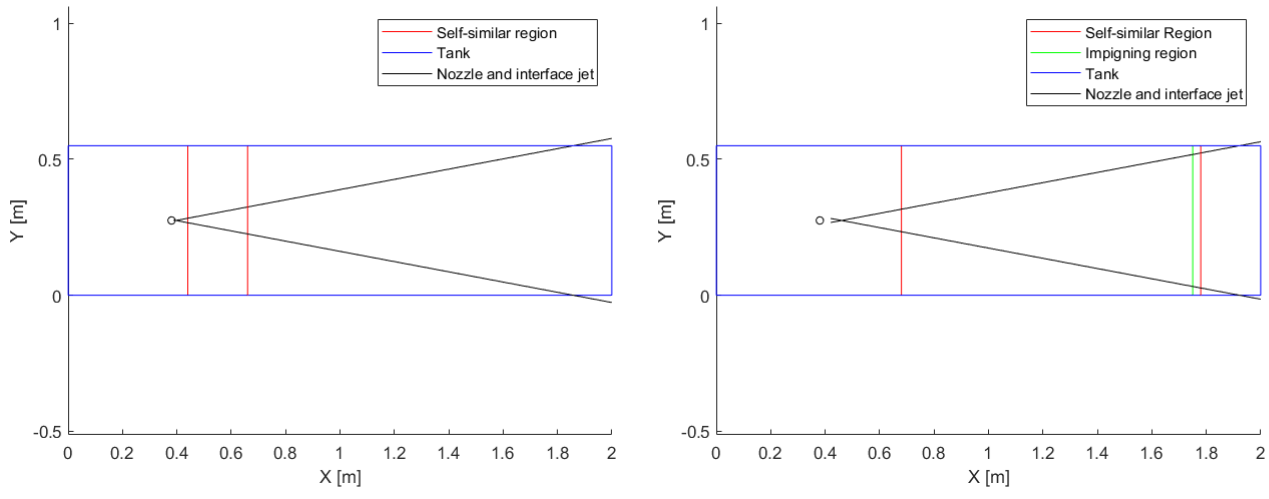

(a) (b)

Figure 11: The spatial constraints within the tank for the two different nozzles (a) $D_\mathrm{n} = 0.002$ m (b) $D_\mathrm{n} = 0.01$ m

4.1.3 Temporal constraints

In terms of time constraints per a single measurement:

- The measurement time should be less than the time it takes before the reservoir is empty.
- Since there is no drainage of water during the measurements, the time is limited to the open space in the tank.
- The measurement time should be less than the time it takes for the flow to become time-dependent due to the boundaries present.
- In the case of moving the camera with the interface the measurement time and distance need to be sufficient to represent the motion and processes at the interface.

The time before the reservoir is empty is dependent on the volume flow of each measurement and, since the nozzle is designed off-center (as explained in Chapter 3), the volume of the open space in the tank is equal to the volume of the reservoir. The maximum time of the measurement due to these are thus the same and equal to $t_{\text{max,reservoir}} = \frac{60}{Q}$. The results of this can be found in Figure 12c; note the log-scale on the y-axis.
To estimate the time before the flow becomes time-dependent due to the presence of the end wall. An estimation of this time was made by integrating the centerline velocity of the jet per Reynolds number. This leaves us at every location with a range of times after which the flow has deflected by the end wall, dependent on the Reynolds number. In Figure 12a and 12b the deflection time for some Reynolds numbers can be found per location.
Moving along with the interface only adds value if one can follow the interface for a longer distance and time. In terms of distance, it has been assumed that the minimum distance one would like to follow the flow is $r_{1/2}$ in streamwise direction. This is the expected scale of engulfment events and notably greater than the Taylor scale. The minimum time to measure $r_{1/2}$ can then be computed by taking into account the velocity the traverse needs to travel to follow the interface. Following the interface in streamwise direction would require a velocity equal to the jump ΔU at the interface which can be estimated as $0.09U_\text{c}$, according to Ref. [54]. With a minimum distance of $r_{1/2}$ and a velocity of $0.09U_\text{c}$ in streamwise direction the minimum measurement time can be computed per location and Reynolds number. The range of measurement times needed per Reynolds number can be found in Figure 12d. Note that motion within this range is thus possible by either measuring at the beginning or at the end of the jet with longer times closer to the nozzle.

To make sure the outward motion of the interface is captured another time scale can be used. As stated before the process of nibbling exists of eddies formed by the shear layer and the transport of eddies. To make sure this is captured one can identify a time scale over which the interface has traveled a notable distance outward. By assuming this distance is of order λ, the minimum time needed for this can be approximated by using the entrainment velocity. The absolute velocity of the interface is $U - E_\text{b}$. With E_b the outward boundary entrainment velocity of the interface and U the mean inward radial velocity at the interface. E_b is given as, [49]

$$E_\text{b} = -2U \tag{4.4}$$

Ref. [54] found that $U = 0.033U_\text{c}$, thus using this the time in which a notable distance has been traveled can be found as; $T = \frac{\lambda}{0.033U_\text{c}}$. This time can be argued to be less than the time to measure a distance of $r_{1/2}$ streamwise, since the velocity differs a factor two but λ and $r_{1/2}$ differ a lot more.

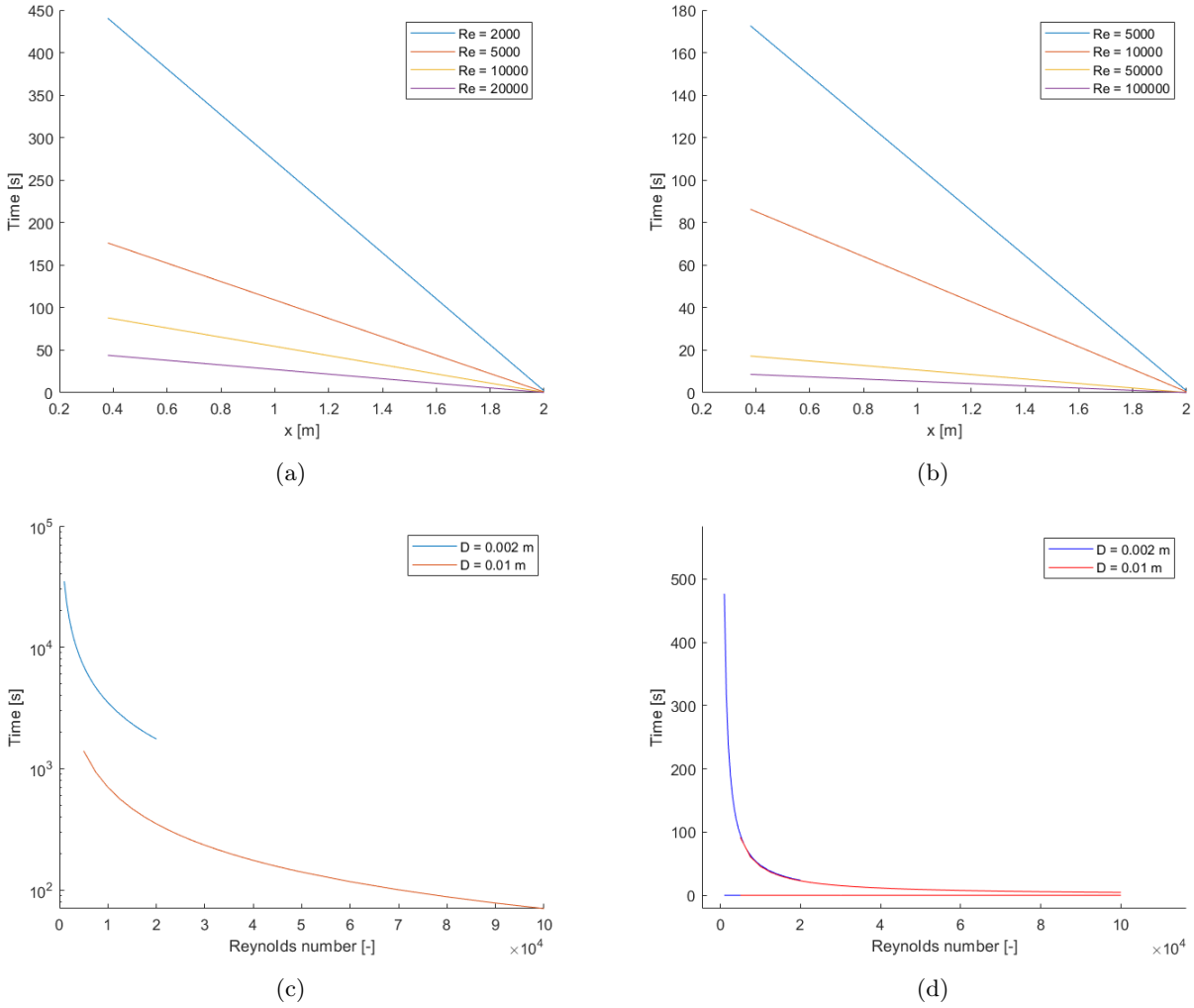

Figure 12: **(a)** The time for a certain x position that deflection from the end wall is expected for different Reynolds numbers and D_n=0.002 m **(b)** Same as **(a)**, but for D_n=0.01 m **(c)** The maximum time before the reservoir of 60L is empty and there is no supply of water to the jet anymore. Note the log-scale on the y-axis. **(d)** The minimum time per Reynolds number necessary to follow the interface over a distance of $r_{1/2}$ for two nozzle diameters. The minimum time occurs closer to the nozzle.

4.1.4 Practical Constraints

Then there are some practical constraints. The design will be tested on these practical constraints in the next chapter.

- η should be big enough to be captured with the available measurement technique (PIV constraint).
- The velocity of the interface should not exceed the maximum velocity of the traverse, which is 0.115 m/s in $x-$direction.
- As more measurements are done (and during), more particles build-up in the tank. This should not have a negative effect on the quality (LIF and PIV constraint).

The constraints for PIV and LIF are verified after the design is presented. These are not included when making the iteration for the design but merely checked afterwards.
As stated before, the velocity in $x-$direction of the interface can be assumed equal to $0.09\,U_c$ [54]. Following the interface outward (z-direction) would require moving at a velocity of $U - E_b$. Using $U = 0.033U_c$ as explained before. The velocity magnitude of the traverse can then be found as,

$$\|U_{trav}\| = \sqrt{(0.033\,U_c)^2 + (0.09\,U_c)^2} = 0.096U_c, \tag{4.5}$$

4.2 Design

From these constraints the following proposal is made. The initial assumption was to measure between a Reynolds number of 2000 up to 100000 using 2 different nozzle diameters (0.002 and 0.01 m) assuming all measurements at a Kolmogorov scale of 0.1×10^{-3} m. Because this means the measurements are conducted at different distances from the nozzle, the centerline velocity will differ per case, since $r_{1/2}$ varies. By varying the time in-between two exposures Δt in PIV, the particle-image displacement can be kept constant.
In Table 2 the designed measurements can be found. For every nozzle diameter, four measurements are planned, two in a safe region and two at the edge of "what can be done" (as will become clear in this chapter). This would make it possible to observe a trend per nozzle diameter. Also, to capture the potential different behaviour per nozzle diameter, $Re = 10.000$ is performed using both D_n.

Table 2: The designed cases, with D_n the nozzle diameter, U_n nozzle velocity, Re the corresponding Reynolds number. X_n is the distance from the nozzle that is necessary to achieve the desired Kolmogorov scale of 0.1×10^{-4} m. The expected separation of scales λ/η is estimated using Equation (4.2).

Case	D_n [m]	Re [-]	U_n [m/s]	X_n/D_n [-]	λ/η [-]
1	2×10^{-3}	2000	1	40	19
2	2×10^{-3}	3000	1.5	53	21
3	2×10^{-3}	5000	2.5	75	24
4	2×10^{-3}	10000	5	123	28
5	1×10^{-2}	10000	1	28	28
6	1×10^{-2}	30000	3	59	37
7	1×10^{-2}	50000	5	84	42
8	1×10^{-2}	100000	10	138	50

4.2.1 Performance of the design

For this design, the spatial and temporal constraints we discussed in the previous section are tested. The constraints are displayed per Reynolds number at the specific distance in Table 2. Note that all these measurement points are thus **not** at the same distance from the nozzle.
First, the Taylor and Kolmogorov scales and the velocity of the traverse is shown in Figures 13a and 13b. The Taylor and Kolmogorov scale for each Reynolds number is estimated using equations 1.5, 1.6, 4.1 and $\left(\overline{u'^2}\right)^{1/2} \cong 0.25U_c$ [33, 54, 58]. It can be seen that the separation of scales is a least 16 (for Case 1). This should be sufficient to accurately distinguish the Taylor and Kolmogorov scale at all Reynolds numbers. Furthermore the separation of scales differs with a factor 2.7, which indicates this range of Reynolds numbers should be sufficient to identify any dependencies.
Using Equation (4.5) the velocity needed to follow the interface can be determined at each location. It can be seen that the desired velocity is much lower than the maximum velocity of the traverse in $x-$direction.

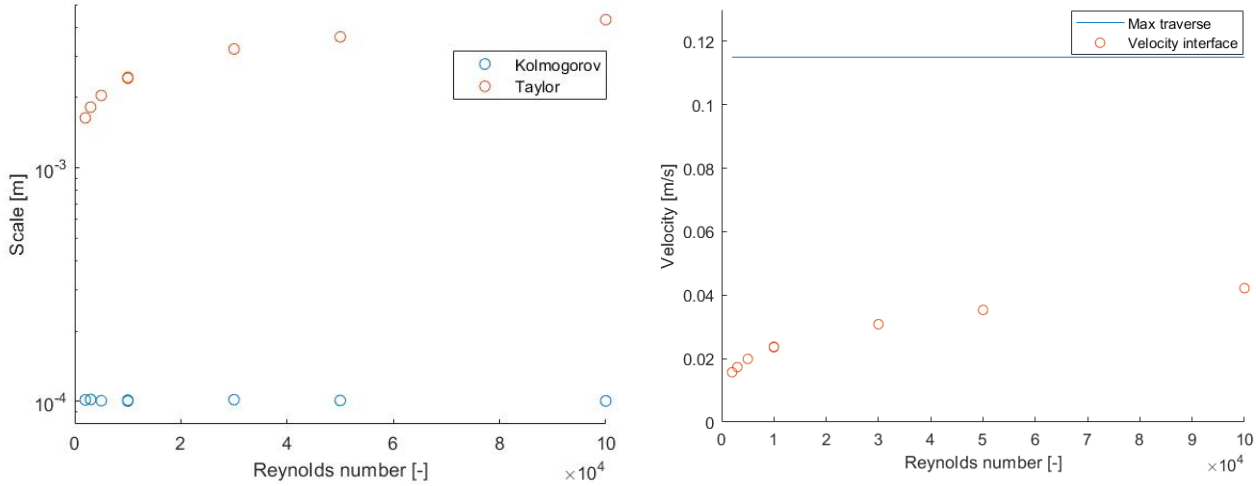

(a) (b)

Figure 13: Performance of the design on the practical constraints **(a)** The Taylor and Kolmogorov scale for the Reynolds numbers at the specific measurement location. **(b)** Maximum velocity of the traverse in x-direction with the anticipated velocity magnitude of the interface.

Now the spatial resolution of the design can be tested. To investigate the possibility to move along with the interface on all positions, $r_{1/2}$ (earlier identified as the minimum travel distance to measure) is plotted centered around our measurement position. This can be seen for the two nozzle diameters in Figures 14a and 14b. For $D_\mathrm{n} = 0.002$ m, there seems to be no problem in the measurement locations that were identified. However, for $D = 0.01$ m at a Reynolds number of 10000, as well as 100000, some problems arise. For $Re = 10000$, the positioning of the measurement area is located outside the self-similar region, here estimated to start at $40D_\mathrm{n}$. This is a safe estimation, so the evaluation of the measured jet data determines if this is unacceptable. Another option would be to focus on a higher η. In Figure 14a it can be seen there is some room for movement. For the Reynolds number of 100000 there are issues: The jet is located very close to the sidewalls and end wall, and potentially on the edge or outside of the self-similar region. By properly quantifying the jet at this location the constraints can be verified. However, as of now it does not seem advisable to do measurements in this region.

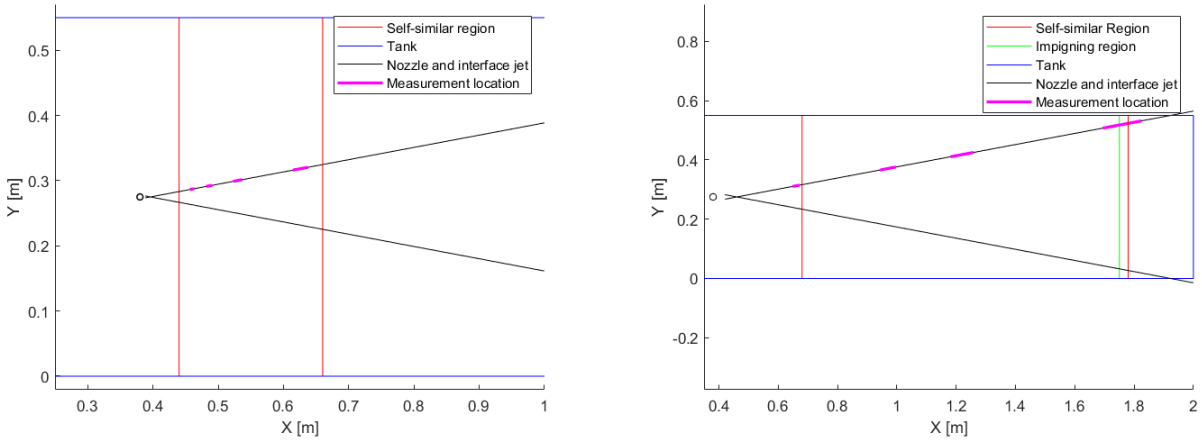

(a) (b)

Figure 14: Performance of the design on the spatial constraints for two nozzle diameters. **(a)** D_n=0.002 m **(b)** D_n=0.01 m

The performance of the design on the temporal constraints can be found in Figure 15. The two maximum measurement time are noted by crosses: i) the time after which deflection from the end wall is expected in red; ii) the time before the reservoir is empty in blue. The two minimum measurement times are noted by circles; iii) the time to measure $r_{1/2}$ in $x-$direction in black; iv) λ in $z-$direction in pink. As expected in the previous

subsection, this second minimum time is a lot less than the first. Note that the figure has a log-scale on the $y-$axis.
From Figure 15 it can be seen that around a Reynolds number of 80000 the time before the jet is deflected from the end wall is less than the minimum time necessary to cover a distance $r_{1/2}$ in streamwise direction while moving with the interface.

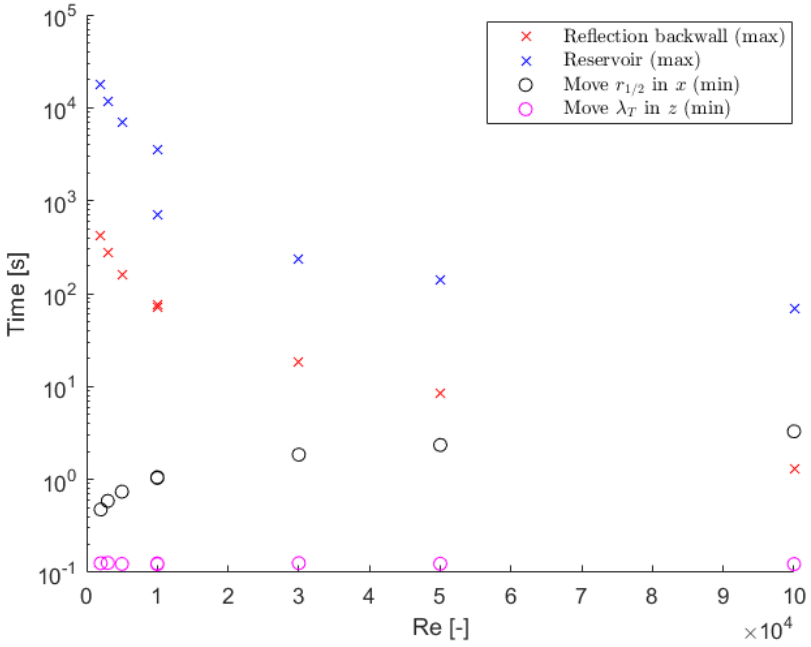

Figure 15: Performance of the design on the temporal constraints with minimum times noted by circles and maxima by crosses (see text).

4.3 PIV & LIF constraints

A constraint that still has to be verified is whether η is big enough to be accurately captured by the available measurement techniques.
It is suggested that the vector spacing required to accurately measure dissipation is around 2η [46]. Assuming an overlap of the interrogation windows of 50% this leads to a window size of 4η. At minimum required to solve the dissipation is solving the maximum of the dissipation spectrum, occurring at 10η, this would also indicate a window size of 5η, which is in line with the general advice of a window $\leq 5\eta$ or $\leq 6\eta$ to accurately capture the Kolmogorov scale η [25, 41, 54].
The probability density function of the location of the interface is approximately Gaussian and quantified as $y_\mathrm{i} = 1.93r_{1/2}$ with a standard deviation of $\sigma = 0.41r_{1/2}$ [54]. When moving along with the flow, as well as for the instantaneous measurements, it is important to make sure that the part of the interface that is captured stays in our field of view (FOV). Assuming a standard deviation of $0.41r_{1/2}$ it is known that to maintain the interface in the FOV 95% of the time a distance of 2σ or $0.82r_{1/2}$ from the expected position on both sides of the interface needs to be captured. This requires a minimum FOV of $1.64r_{1/2}$. Due to the fixed amount of pixels on the image of the camera, a bigger FOV leads to a bigger interrogation window, and thus a coarser spatial resolution.
In Figure 16 the ratio between the FOV in y-direction and $r_{1/2}$ can be found for a window size of 5η and 10η. Note that using an overlap of 50% the vector spacing is thus half the window size.
It can be seen that it is very difficult to fulfill both requirements for the higher Reynolds numbers as it is now. Also since it will practically be impossible to locate the camera exactly at the correct position a bit of margin is desirable.

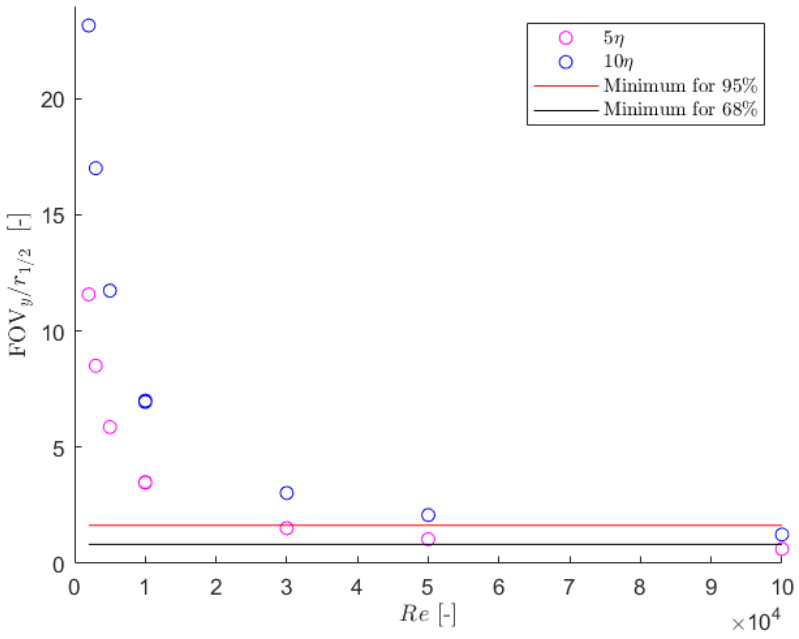

Figure 16: The ratio of FOV in y direction and the half-width of the jet at the measurement location compared to the expected distribution of the interface.

Another practical constraint for PIV and LIF is the build-up of particles and dye in the tank. During a measurement, or when performing multiple runs in a row, there is no constant drainage or filtering of the water in tank. This means the particle and dye concentration increases. Particle build-up can lead to cloudy or even opaque water which affects the quality of the PIV measurements, as it leads to loss of correlation.
The build-up of LIF dye has a potential influence on the identification of the interface. More on this can be found in Chapter 5. The time to empty and refill the tank is approximately 45 - 60 minutes and should therefore be avoided in between tests. As explained in Chapter 3 a 1 μm filter is installed to remove the particles from the water.

4.4 Final design

With the knowledge of the performance of the nozzle setup in Figure 8a and the performance on the previous design on the constraints a new design is made. The expectations for this can be found in Table 3. All are expected at $\eta = 9.5 \times 10^{-5}$ m.

Table 3: The planned measurements and expectations. With (X_n,Y_n) the position with respect to the nozzle, D_n the nozzle diameter, U_n, Re, T_{backfl} and λ_{exp} the expected velocity at the nozzle, the Reynolds number, the time before back flow occurs and the Taylor scale.

Case	X_n/D_n [-]	X_n [cm]	Y_n [cm]	D_n [cm]	U_n[m/s]	Re [-]	T_{backfl} [s]	λ_{exp} [cm]
1	42	8.4	0	0.2	1.2	2.4×10^3	348	16
2	52	10.4	0	0.2	1.65	3.4×10^3	250	17
3	67	13.4	2	0.2	2.33	4.7×10^3	174	19
4	134	26.8	2.5	0.2	6.16	1.2×10^4	60	24
5	30	30	2.5	1	1.23	1.2×10^4	57	24
6	57	57	8	1	3.18	3.2×10^4	18	30
7	76	76	12	1	4.8	4.8×10^4	10	34

Designing PIV settings (Choice of FOV and Δt) Taking into account the expected Kolmogorov scale and expected $r_{1/2}$ the FOV in y chosen to be around 100 mm. Assuming an interrogation window size of 16 pixels this would mean a window size of 6.6η or vector spacing of 3.3η assuming 50% overlap.
Due to the 'intermittency' of the jet, not all snapshots are expected to include the interface of the jet, mainly at high Re. Therefore this has to be checked visually and snapshots without an interface present are excluded.

The time in between two exposures Δt is determined by estimating the maximum centerline velocity U_c using Equation (1.2) and equaling the time to travel a quarter interrogation window. Before each measurement some test snapshots are taken of the jet to verify the choice of Δt, and then altered when needed.
The amount of particles is found for Case 1 by means of adding more and more particles to the source solution until there was no increase in correlation anymore (indicating convergence has been reached). This value is extrapolated to other cases.
In Cases 1 to 3 the number of recorded frames N_F is taken in a single run; Cases 4 and 5 in two runs, and Cases 6 and 7 in 6 and 8 runs, respectively. This to prevent back-flow in the measurements.

Table 4: The actual measurement conditions per case, with Q the measured volume flow and U_n the from there calculated nozzle velocity. Cp is the source particle concentration and M_0 the magnification.

Case	X_n [cm]	Y_n [cm]	Q [L/min]	U_n[m/s]	Re [-]	Δt [ms]	C_p [mg/L]	FOV [cm]	M_0	N_F
1	7.4	0	0.18	0.95	1.9×10^3	0.8	59	8.37x9.92	0.168	817
2	10.4	0	0.23	1.21	2.4×10^3	0.65	76	8.42x9.98	0.167	1032
3	13.4	2	0.43	2.23	4.6×10^3	0.5	240	8.42x9.98	0.167	1032
4	26.8	2.5	1.15	6.10	1.2×10^4	0.45	170	8.41x9.97	0.167	1002
5	30	2.5	5.55	1.18	1.2×10^4	0.45	170	8.43x9.99	0.167	962
6	57	8	14.8	3.14	3.1×10^4	0.35	110	10.3x12.2	0.137	846
7	76	12	22.4	4.76	4.8×10^4	0.3	100	10.3x12.2	0.137	648

Camera moving along the flow For the measurements where the camera moves along the flow it is chosen to perform this at a single Re of around 1.2×10^4 using $D_n = 0.1$ m, the specifics can be found in Table 13. In Figure 16 this Re number is the highest where fewest problems are expected for capturing the interface.
It is chosen to start at $X_n = 0.3$ m, which is the "Begin" location. This is the location where the instantaneous measurements are taken as Case 5 and thus the average flow quantities are known. The measurement is performed at a maximum distance that the light sheet can reach, which is up to $X_n = 0.7$ m, referred to as the "End" location.
Y_n is dependent on the angle of the traverse, which is found by doing some test runs and visually guide adjustment until the interface is at the center of the FOV during the run.
Using Equation (4.5) the expected $U_{i,x}$, the velocity of the interface in x direction, can be estimated. In the full range of the measurements this ranges from 0.9 - 2.34 cm/s. The acceleration of the traverse in x direction is set to its maximum. The final traverse velocity in x direction, $U_{t,x}$, is reached in 0.1 seconds. The acceleration in y direction is set to reach its final velocity in the same time, to ensure that the path of the traverse remains linear.

To be able to resolve the Kolmogorov scale, a similar FOV is used as for the instantaneous measurements. It is chosen slightly bigger to counteract errors in the angle at which the traverse moves. Since η becomes bigger with downstream distance, the resolution of the measurement with respect to η improves downstream. Since there is a large reduction in flow velocity over this longer distance, PIV settings need to be chosen with care.
Assuming that the traverse matches the velocity of the interface, Δt is constrained in multiple ways:

- To reduce loss-of-correlation in the out-of-plane displacement, Δt needs to be smaller than the time for the particles to travel more than $\frac{1}{4}$ of the expected light sheet thickness. This is estimated using the maximum level of expected velocity fluctuations via Figure 30c and an assumed light-sheet thickness of 1 mm.
- Δt needs to be sufficiently large to capture the velocity fluctuations at the interface ($U_{rms,i}$), assumed as $0.1U_c$ following from Figure 30c.

The axial velocity is $0.02U_c$ as maximum, with U_c the local centerline velocity, and thus not of importance. An exposure time-delay Δt of 4 ms is used, translating to an expected displacement by $U_{i,rms}$ of 2.2, 1.3 and 0.8 pixel per distance from the nozzle, respectively. To avoid the loss of in-plane correlation, window shifting can be applied. Since the relative velocity is changing throughout the data set this will be necessary, mainly at the beginning of the set.

Table 5: Settings of the traverse mechanism, with velocities and accerelations in cm/s and cm/s^2.

Case	X_n [cm]	Y_n [cm]	Angle [°]	$U_{t,x}$	Acc_x	Acc_y	C_p [mg/L]	FOV [mm]
Moving	0.3 - 0.7	0.04 - 0.1199281	11.3	2	19	3.2265705	110	101.7x120.6

Table 6: Expected velocities and corresponding exposure time-delay Δt in the FOV of the traverse at the Begin, Mid and End location, as defined in the text.

Location	U_c [cm/s]	$U_{i,rms}$ [cm/s]	$U_{max,rms}$ [cm/s]	$dt_{max,oop}$ [ms]	WS/η [-]
Begin	26	2.6	7.8	3.6	12.3
Mid	15	1.5	3	9.4	6.9
End	10	1	1.25	22.6	4.8

5 Processing

5.1 LIF

Calibration of the LIF data is necessary to form a relationship between the intensity of the image versus the concentration of Rhodamine B in the jet. This calibration is not necessary for interface detection, however, calibrated data make it possible to do quantitative analysis on the turbulent mixing, and thus the entrainment process. The concentration of LIF dye can be described as, [14]

$$C(x, y) = \alpha(x, y)I(x, y), \tag{5.1}$$

where $I(x, y)$ is the image intensity, $C(x, y)$ the concentration of Rhodamine B, and $\alpha(x, y)$ a variable that can be influenced by multiple parameters including laser intensity, dye concentration along the path of the laser beam outside the region of interest, pH and temperature. In this calibration, $\alpha(x, y)$ is assumed to be independent of most, except for the distribution of laser intensity within the field of view. Therefore it is necessary to estimate $\alpha(x, y)$ as a function of location.
This is found by taking snapshots at a homogeneous and known concentration, which is done by lowering a small tank at the location of the jet to mimic the experimental conditions. The distribution of laser light within the sheet is not expected to be linear, thus it is chosen to fit the measured intensities to a third order polynomial (following Ref. [37]),

$$\alpha(x, y) = p_{00} + p_{10}x + p_{01}y + p_{20}x^2 + p_{11}xy + p_{02}y^2 + p_{30}x^3 + p_{21}x^2y + p_{12}xy^2 + p_{03}y^3, \tag{5.2}$$

An example of $\alpha(x, y)$ for Case 2 from Table 2 can be found in Figure 17.
This method is repeated for every Reynolds number separately, since every measurement uses a different positioning (and thus distribution) of the laser sheet. The calibration is performed on the same day as the measurement, limiting the potential error in environmental conditions, such as pH and temperature differences. The coefficients of Equation (5.2) per case can be found in Table 15 in Appendix B.

Linearity In order for Equation (5.1) to be valid and use a single calibration $\alpha(x, y)$ for differing concentrations, the relation between $C(x, y)$ and $I(x, y)$ needs to be linear.
If the concentration is relatively high the fluorescence intensity will saturate. In the extreme situation the fluorescence remains constant with increasing concentration due to full saturation [50]. If the concentration is relatively low, the jet may not be distinguishable from the background due to the lack of fluorescent dye molecules, causing complications identifying jet and non-jet fluid.
Due to these uncertainties it is important to find the concentration for which linear behaviour of the Rhodamine B is guaranteed and stays within this range. This can be found in Figures 19, 20 and 21.
In Figure 19 it can be seen that for Case 2 (see Table 2) a slight variation in linearity per location is found, but the image average seems to be representative to validate linearity. It can clearly be seen that above a certain concentration saturation will occur. In Figure 20 the image average is compared for all Cases. The maximum concentration to guarantee linearity $C_{\max}$ can now be estimated. $C_{\max}$ is safely assumed as the highest measured concentration that lies within 5% of the linear fit, which is fitted on the lowest 3 concentrations. The values of $C_{\max}$ can be found in Table 15 in Appendix B.
For the measurements with moving camera, the linearity is checked on the start and end of the measurement domain, as can be seen in Figure 21. Here as well, saturation is visible for the higher concentrations. $C_{\max}$ is defined in the same way as for the stationary measurements and can be found in Table 15 in Appendix B.

Environmental influences A variation in pH or temperature can lead to a difference in image intensity with constant concentration. The pH of the solution influences the attenuation of the laser light by the Rhodamine, while the temperature of the solution has an impact on the ratio of emittance versus absorption of the molecules [50]. The solution for the jet and calibration are kept in closed reservoirs and the water originates from the same source as the water in the tank. The pH is thus assumed to be constant during the measurements. Furthermore, according to Ref. [11], no effect on fluorescence is found for pH fluctuations between 4 - 12 using Rhodamine B and a Nd:YAG laser.
Ref. [11] did find an effect of 3% on image intensity per a temperature difference of 1°C. This can potentially be substantial assuming day-to-day variation in temperature. To limit the effect of temperature, the calibration is done at the same day as the measurements. This will limit the temperature variations in the surroundings, and the difference in temperature of the water in the tank throughout the day will be assumed negligible.

Bleaching After long exposure to high intensity light the the ability of Rhodamine to fluorescence weakens, a process called bleaching. For the measurements on the jet this is no problem, since every snapshot contains a part of the jet with fresh Rhodamine. However, for the calibration solutions this should be considered. One batch of calibration solutions is not used for more than two calibrations, totalling up to 1000 snapshots, equal to 100 seconds. Ref. [11] reported a deviation in intensity of around 1% after ∼100 s of exposure time for a Nd:YAG laser with similar pulse length and intensity. Taking into account that they operated at a three times higher frequency (but single pulsed) this provides us with a very safe estimation.

Background concentration As mentioned in Chapter 4 there is not drainage of water during the measurement or in-between runs. This means that the background concentration of dye increases during the measurement, potentially causing attenuation of laser light to occur. The fluorescence intensity (assumed to be equal to image intensity) I can be described as, [50]

$$I = I_0 \ 10^{-\epsilon C d}, \tag{5.3}$$

where I_0 is the excitation beam intensity, ϵ the extinction coefficient of around 10^5 L/mol cm [28], C the concentration in mol/L, and d the distance the beam had to travel, which is around 0.25 meters. As C approaches 0, which is true in the absence of background dye concentration, there is no attenuation of the laser beam and $I = I_0$. The maximum increase of background concentration occurred at $Re = 5000$, equal to $2.4{\times}10^{-6}$ gr/L or $4.9{\times}10^{-9}$ mol/L, assuming a molar mass of 479.02 gr/mol [9]. This leads to $I = 0.97I_0$, meaning a potential maximum deviation of $\tilde{3}$ %.
Another effect of background concentration is how it affects the jet visibility. In the limit of too much background concentration the water becomes cloudy and the camera is not able to properly view the measurement plane in the middle of the tank where the jet is located. This effect is similar as a too high concentration of PIV particles. It is assumed that if the water is clean enough to perform quality PIV measurements, the influence on the performance of the LIF is negligible.

Pulse-to-pulse variation The pulse-to-pulse variation of the laser is noted as 3% by the manufacturer [44]. At calibration the minimum amount of 200 snapshots is used for any average, limiting this influence to around 0.23%. However, in the instantaneous snapshots this remains a challenge for the accuracy of the computed concentration. Potential solutions include measuring the intensity per pulse and applying a correction or, when this technique is not available, normalizing the images based on their relative intensity within the data set.

The measured concentrations during the different cases can be found in figure 22. In figure 22a the centerline decay of concentration can be found, plotted using the scalar virtual origin. Cases 1 and 4 seem to have a comparable decay (slope), and so do Cases 2,3 and 5. Case 4 is likely to be influenced by mixing, as will be shown in Chapter 6 as well, but for the others the uncertainty in C_0 is likely to have an influence. Assuming Case 1 is the odd one out, this deviation would translate to a underestimation of around 10-15% of the initial concentration.
The non-linearity of Case 3 that can be seen in figure 22b has consequences for the accuracy of the concentration. It is underestimated due to saturation of the Rhodamine. However, the ratio within the image, and therefore also the TNTI or vorticity profile, won't be seriously affected.

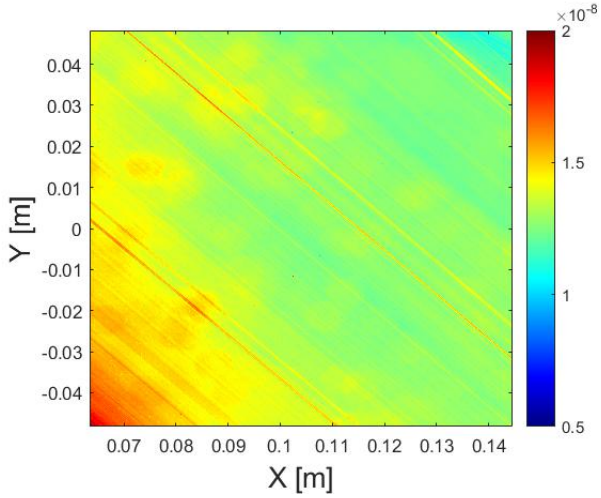

(a)

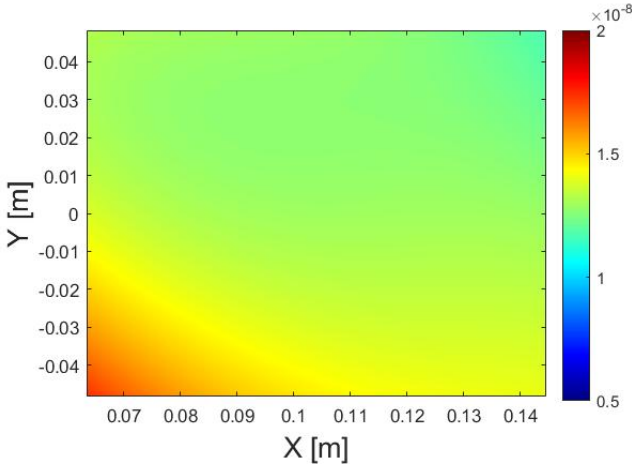

(b)

Figure 17: **(a)** $\alpha(x, y)$ before fitting the polynomial. $\alpha(x, y)$ is found via Equation (5.1) at $C = 2 \times 10^{-5}$ gr/L. $I(x, y)$ is measured as the average of 500 snapshots and corrected using a background measurement at $C = 0$ gr/L. **(b)** For calibration of the intensity data the third degree polynomial of $\alpha(x, y)$ is used, as viewed here. The coefficients can be found in Table 15 in Appendix B

.

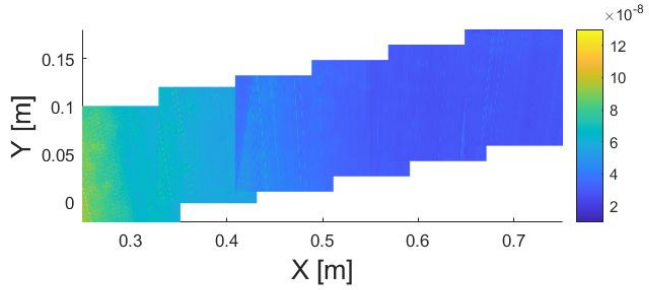

(a)

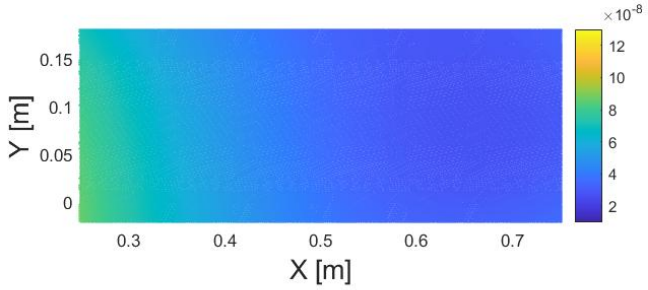

(b)

Figure 18: **(a)** For the moving measurements the calibration is performed for the whole domain by measuring at 6 different locations and combining these fields of views. $\alpha(x, y)$ is found at a $C = 2 \times 10^{-5}$ gr/L. $I(x, y)$ is the average of 100 snapshots to limit the exposure time and corrected for background at $C = 0$ gr/L. **(b)** For calibration of the intensity data the third degree polynomial representation of $\alpha(x, y)$ is used, as viewed here. The coefficients can be found in Table 15 in Appendix B.

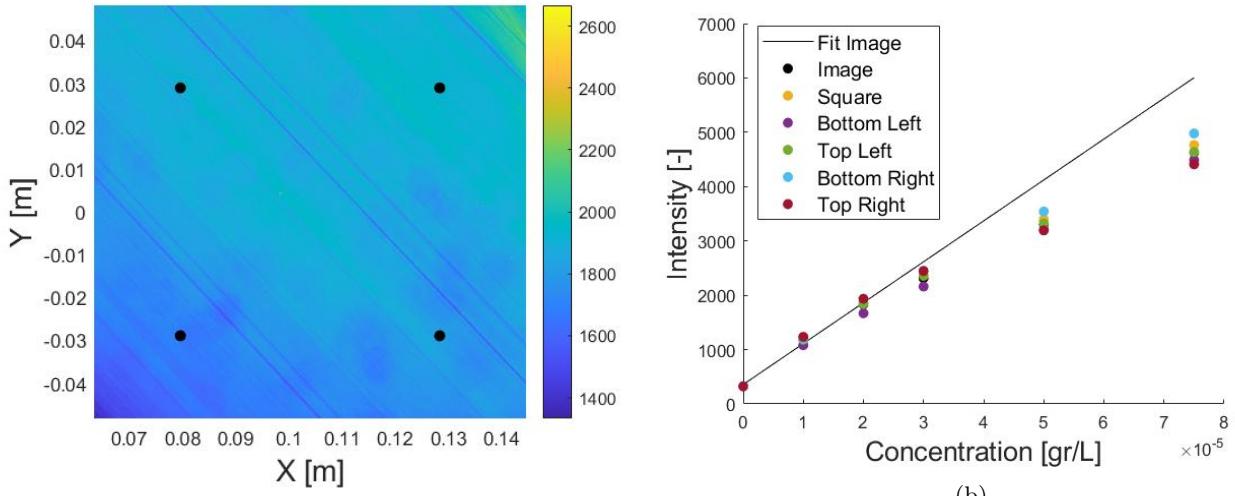

(a) (b)

Figure 19: **a)** Locations of the triangle vertices for which the relation between concentration on intensity is tested. The data are for Case 2 (see Table 2). **b)** The relation between concentration of dye and image intensity found at the 4 locations in **a)**, the average of the rectangle they span and the whole image.

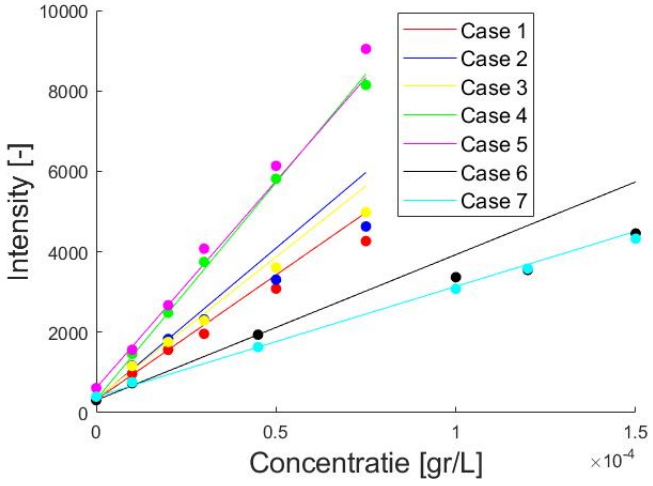

Figure 20: The relation between concentration of dye and image intensity for all Cases (see Table 2).

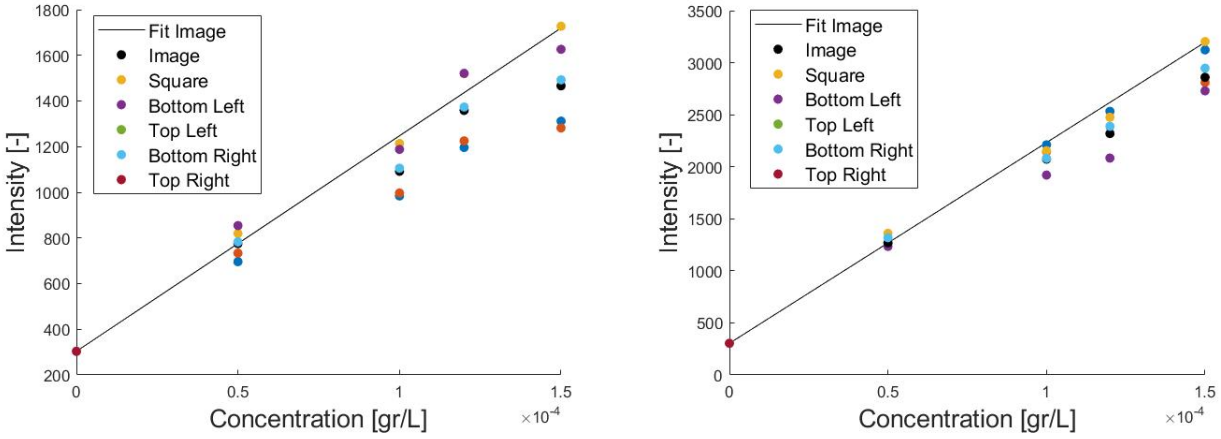

(a) (b)

Figure 21: For the measurements with moving camera the linearity is assessed at the start and end of the domain. The location of the vertices is equal in the FOV as Figure 19a **a)** Linearity at the start FOV of the domain **b)** Linearity at the end FOV of the domain

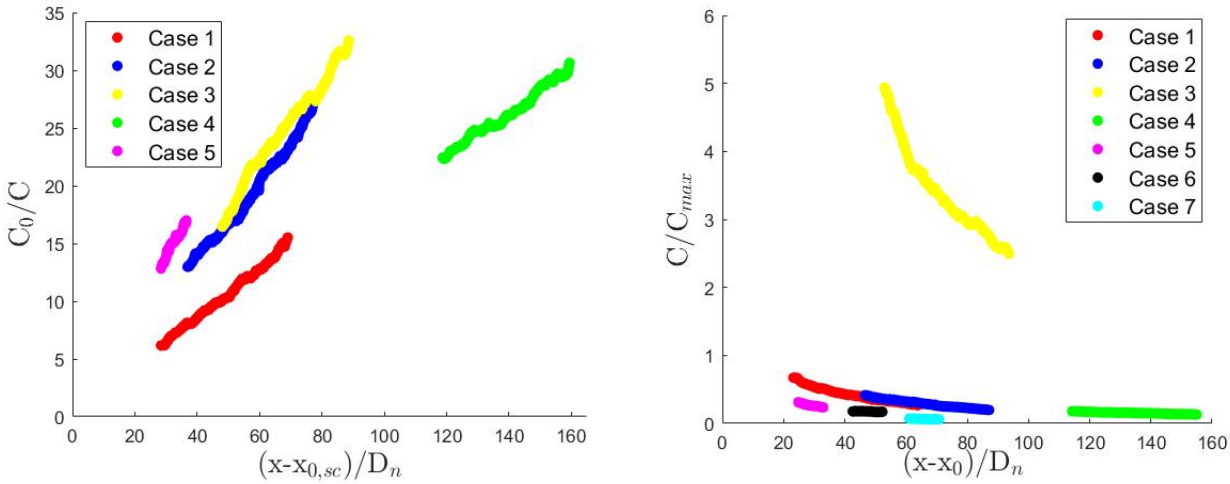

(a) (b)

Figure 22: **(a)** Decay of the concentration at the centerline, scaled with the source concentration C_0. Cases 6 and 7 (see Table 2) did not have the centerline in their FOV and are therefore not included in the figure. **(b)** The maximum measured concentrations in the field of view scaled with $C_{\max}$. It can be seen that only for case 3 linearity can not be assumed, and the actual concentration is likely underestimated.

5.2 Instantaneous data

The processing of the instantaneous data consists of a couple of steps;

- Find the contour of the jet
- Acquire the vorticity field from PIV data
- Compute the conditional vorticity profile

5.2.1 Contour

To find the contour of the jet, the LIF data is used. First the LIF data is corrected for the background using a background image. The background image exists of the average of 500 snapshots that are taken before each measurement. Then the snapshots are corrected for homogeneity in the laser illumination using the calibration

polynomial, transforming the intensity data to concentration data and afterwards filtered using a median filter of 3x3 pixels. This to remove potential contributions from tracer particles scattering fluorescent light [16, 24].
In order to find the contour of the jet, a threshold needs to be found to distinguish 'jet' and 'not-jet' fluid. This threshold is identified using a method adapted from Ref. [36], as seen in figure 23.
The threshold ϕ is found for each frame individually, eliminating the effect of pulse-to-pulse variation in intensity of the laser. It can be noted from figure 23c there is a wide range of thresholds that could potentially identify the transition between 'jet' and 'non-jet' fluid. The currently used method provides a threshold in the middle of this jump in concentration, while other methods or adaptions may find slightly lower or higher thresholds. For example Ref. [54] finds a threshold more on the lower side of this jump.

5.2.2 Sensitivity of the contour

Influence of filtering Before threshold detection the instantaneous LIF data is filtered. The effects of the filtering to threshold detection and location of the interface are examined.
A Gaussian filter with a standard deviation of 3 and 5 pixels and a median filter with a size of 3x3 and 5x5 pixels are compared to an unfiltered image. None of the applied filters caused a change in the detected threshold value. However the contour varied. This can be seen in Figure 24. Due to the nature of the filters, the Gaussian filter is expected to be more smoothing or blurring, but may be more effective at reducing noise.
Following Figure 24, the median filter seems to be effective in removing noise from the concentration profile, without altering the location of the interface. This corresponds to theory and literature, indicating that a median filter should be used when edges are present [34]. In Figure 24d it can be seen that the Gaussian filter type only causes only a slight shift of the edge of the jet, however the morphology of the contour may differ in certain areas, as can be seen in Figure 24c.
The Kolmogorov scale η is expected to be around 3 pixels. Median filters completely remove features up to half the size of the kernel [34]. Therefore a 3x3 px median filter seems on the safe side for our application, and influence on all relevant length scales should be minimal.

Influence of binarization Some authors prefer the binarization to 'jet' or 'non-jet' of the image before identification of the contour [54]. Identifying a contour in a non-binary image will allow interpolating of location in between pixels, while a binary image will give a sharper line or boundary. The effects can be found in Figure 25. The effect of finding the contour after binarization seems to be minimal, and therefore it is not applied.

Influence of threshold Since multiple adaptions of the threshold are used in literature it is interesting to see how sensitive the location of the contour is to the threshold. This can be found in Figure 26 for half and double the detected ϕ. The location of the contour seems to be varying similarly as in Ref. [54] and seems quite invariant to the change, considering a factor four difference. The influence of the difference in threshold on the final results is examined in Chapter 6.

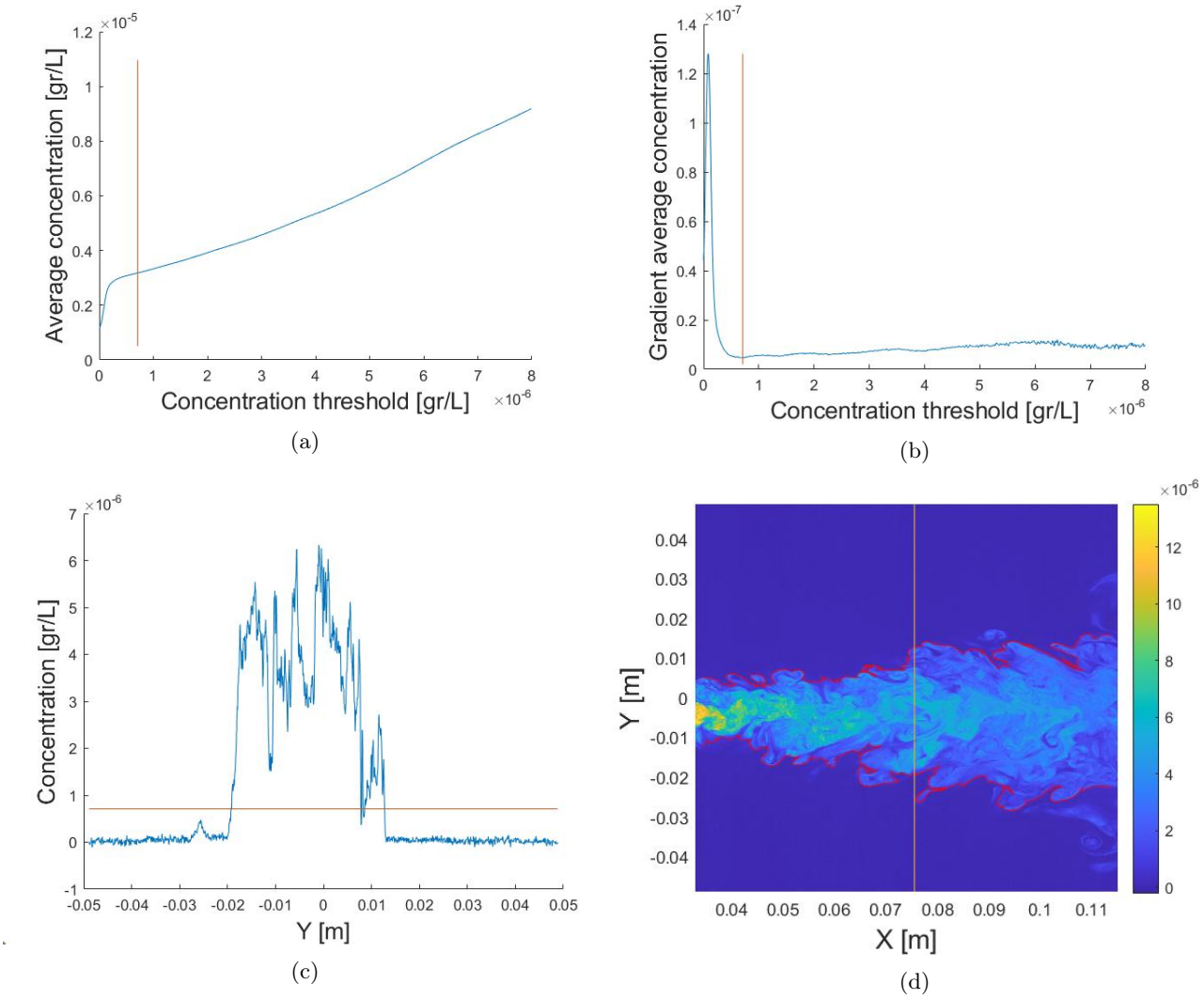

(a) (b) (c) (d)

Figure 23: To identify threshold ϕ the average concentration above a potential threshold is found. Doing this for a range of thresholds exposes a sharp intensity change within the image. The threshold ϕ is assumed as the minimum in the gradient of this curve **(a)** The average concentration as function of potential thresholds, with the found threshold ϕ in orange. **(b)** The gradient used to identify ϕ. **c)** The intensity profile in y including the threshold at the location found noted in **d)**. The threshold is within the correct range, around halfway the 'jump' **d)** The upper and lower contour following as the interpolated isocontour of ϕ.

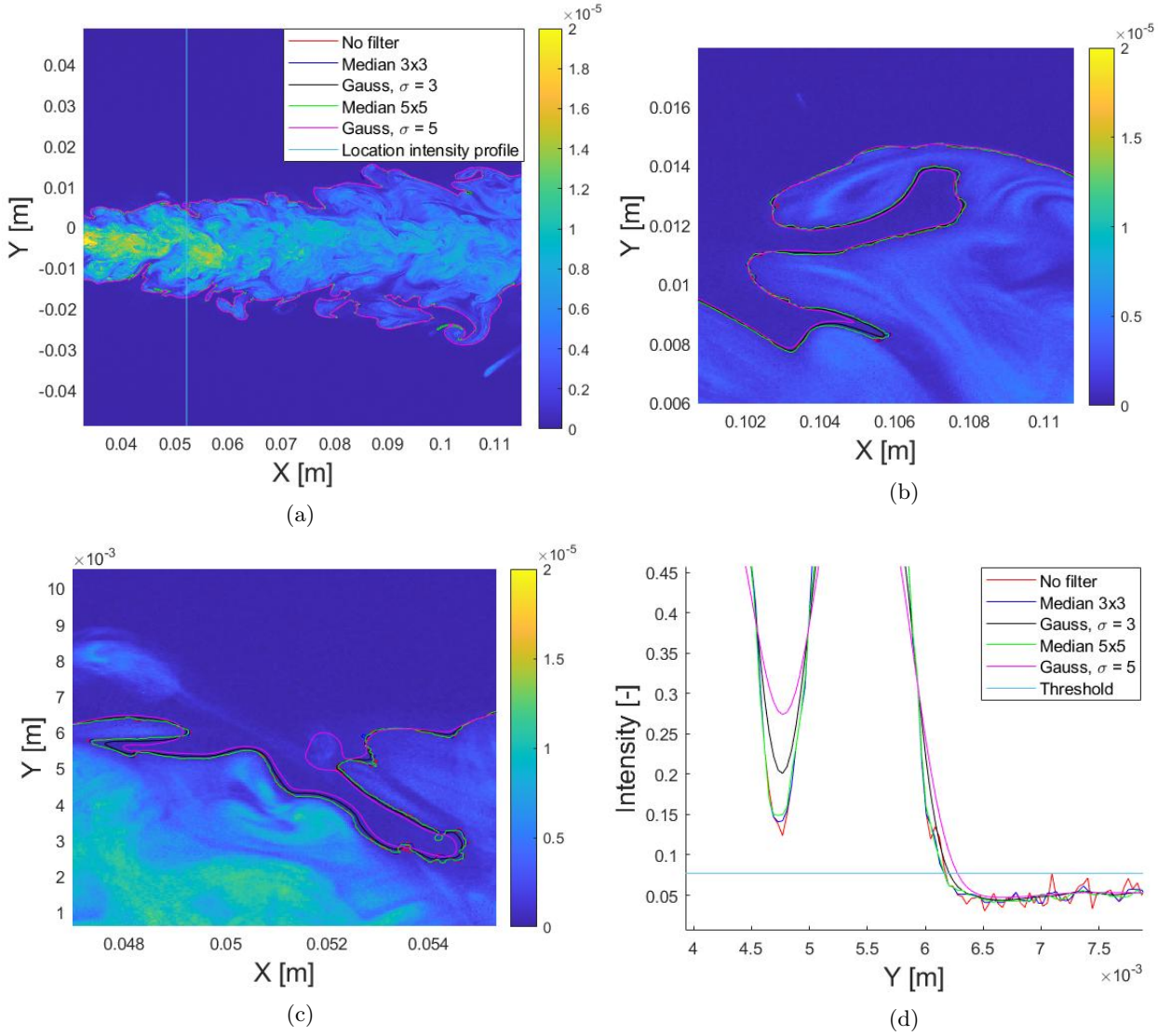

Figure 24: The influence of Gaussian and median filters on the contour is investigated, as explained in the text. **(a)** Overview of the full contour by changing the type of filtering **(b)** Detail of the contour in **(a)**, the unfiltered contour looks prone to noise, while the Gaussian filter with standard deviation of 5 is clearly located more outward. **(c)** Detail of the contour in **(a)**, the Gassian filter with $\sigma = 3$ also appears more outward. **(d)** A detail of the concentration profile in y, at the location specified in **(a)** around the threshold. The blurring effect of the Gaussian filters can clearly be seen.

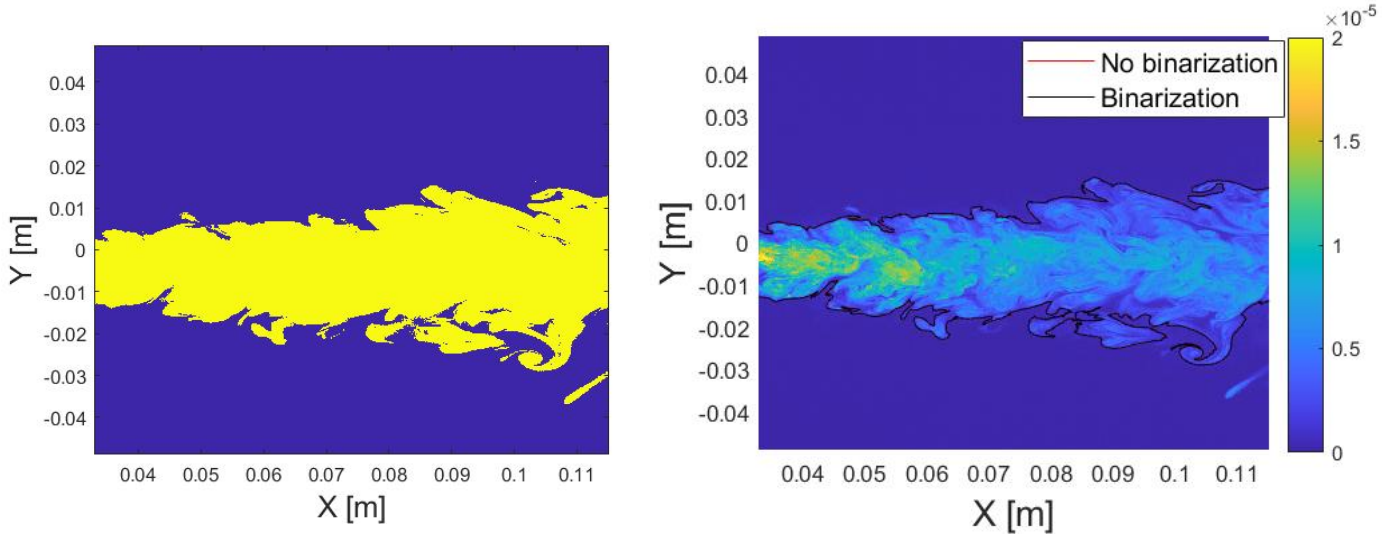

(a) (b)

Figure 25: **(a)** A binary image of the instantaneous image is achieved after the value of each pixel is compared to the threshold. **b)** Comparison of the detected contour on the binary or on the concentration image.

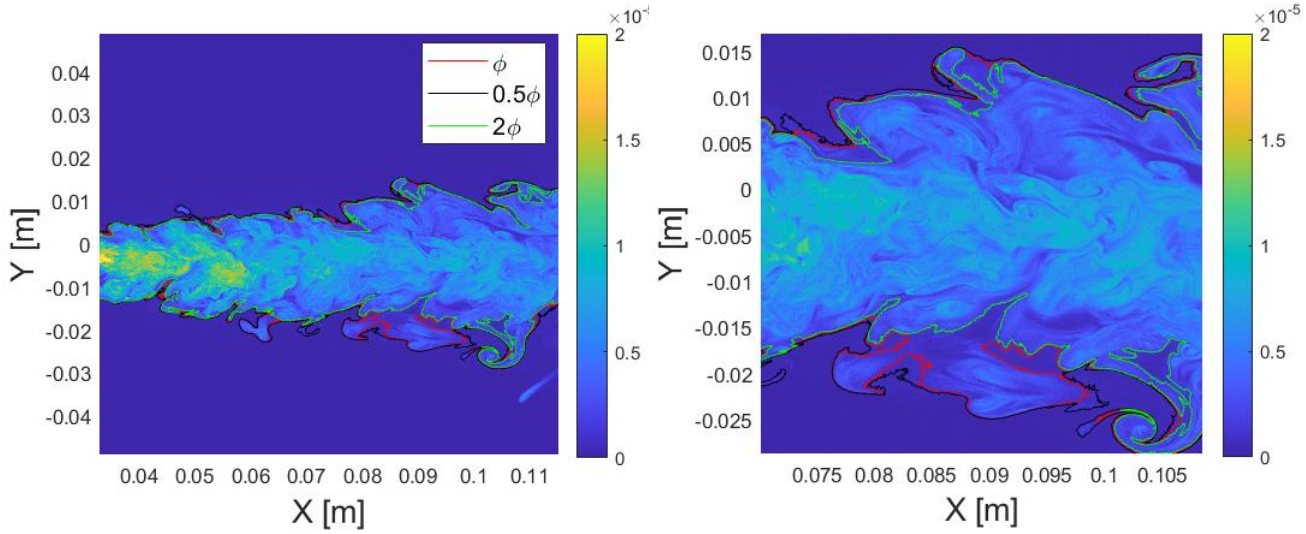

(a) (b)

Figure 26: The sensitivity of the contour location based on the threshold can be visualized by comparing the isocontours of 0.5ϕ, ϕ and 2ϕ. **(a)** Overview of the different contours dependent on threshold **(b)** Detail of the contours, the difference can clearly be seen on the protruding parts of the jet.

5.2.3 Vorticity

The out-of-plane instantaneous vorticity field ω_z is found using flow circulation [2],

$$\omega_z = \lim_{\mathcal{A}\to 0} \frac{1}{\mathcal{A}} \oint_{\mathcal{C}} \mathbf{u} \cdot d\boldsymbol{\ell}, \tag{5.4}$$

where $\mathcal{C}$ is the contour around $\mathcal{A}$ and $\mathbf{u}$ the velocity vector.
This method is an alternative to estimating the curl on velocity data using second-order differences. It has shown to cause less noise and lowers the error [2].
The velocity field is found using PIV. The raw snapshots are filtered using a Min/Max filter of 2x2 pixels and processed using a multi-pass grid analysis. The Min/Max filter is used to normalize the image contrast and remove a potentially slowly varying background [47]. The size is found by optimizing the fraction of valid

displacement measurements in different frames of the Case 1 measurement set (see Table 2).
The multi-pass grid analysis is started with once a 32x32 pixel interrogation window with 50% overlap. After that an interrogation window of size 16x16 is used four times, again with 50% overlap.
For post-processing a median test is applied using Universal Outlier Detection on a 3x3 region [56]. This method compares the median value of a region of neighboring vector to the vector itself to find spurious vectors. Vectors are removed if residual is > 2, and (re)inserted in residual is < 3. Empty spaces are filled via interpolation. For more information about the method, see Ref. [56].
For practicality it has been chosen to use similar settings for all Cases after optimization for Case 1. For all cases these settings are verified to provide sufficient accuracy by looking at the cumulative first and second vector choice. This should be $> 95\%$ in the middle of the jet. This is done for some frames in the beginning, middle and end of the data set.
The instantaneous vorticity field ω_z of Cases 1 and 6 can be found in Figure 27.

5.2.4 Conditional vorticity

The conditional vorticity can be found by defining lines perpendicular to the interface and linearly interpolating the vorticity field on these lines.
Per instantaneous image the intersection with the interface is found, a perpendicular line is drawn, and the scaled vorticity is computed on 2001 points in a range of -2$r_{1/2}$ up to 2$r_{1/2}$. This spacing is, at the highest $r_{1/2}$, slightly larger than the expected Kolmogorov scale. This is done at 810 equally spaced locations in x for which convergence is reached, as further discussed and shown in Chapter 6 and Figure 37b. The vorticity is found using a linearly interpolated function of the vorticity, after which the local half-width $r_{1/2}$ and centerline velocity U_c are used to find the scaled vorticity.
These scaled profiles are averaged per image, and for the whole data set. This method is similar to others in the literature, with some notable differences;

- The lines along which the conditional vorticity profile is computed are perpendicular to the interface instead of vertical, as can be seen in Figure 28.
- Instead of identifying the envelope as the outer pixel in vertical direction above the threshold, and with that including engulfing events in the interface envelope, the interface is defined as the isocontour of ϕ.

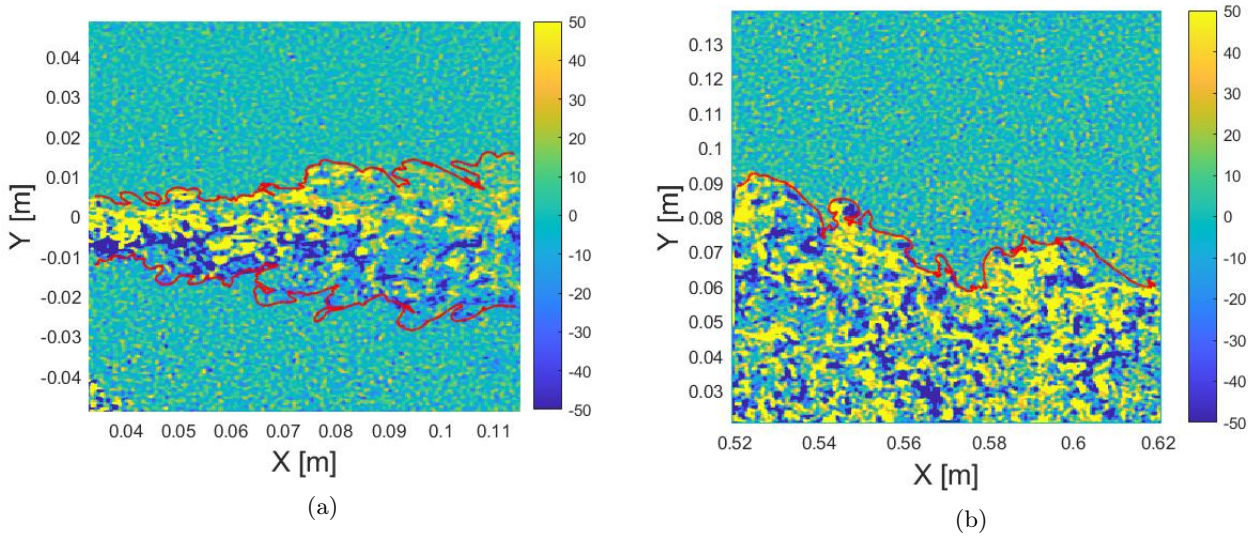

(a) (b)

Figure 27: The instantaneous vorticity field found via the flow circulation in Equation (5.4) together with the detected scalar contour. **(a)** Case 1 **(b)** Case 6

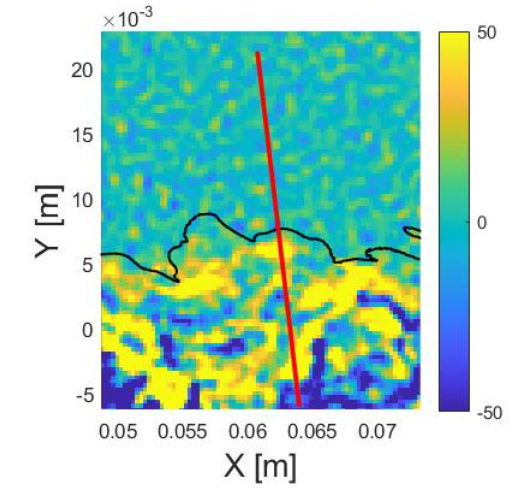

(a)

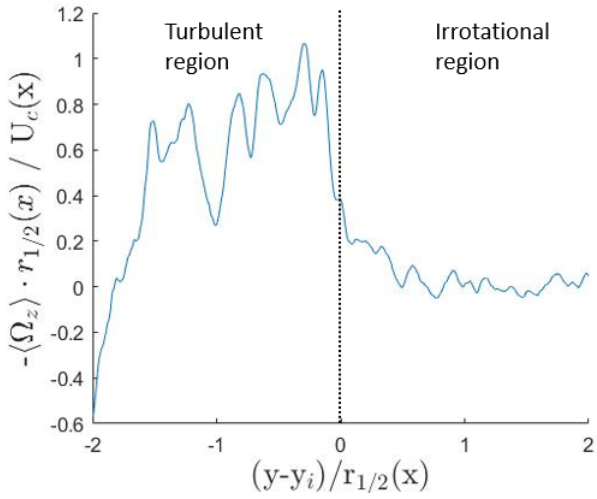

(b)

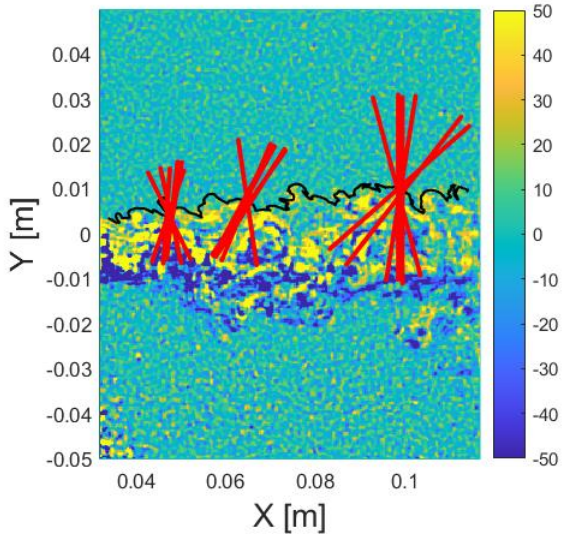

(c)

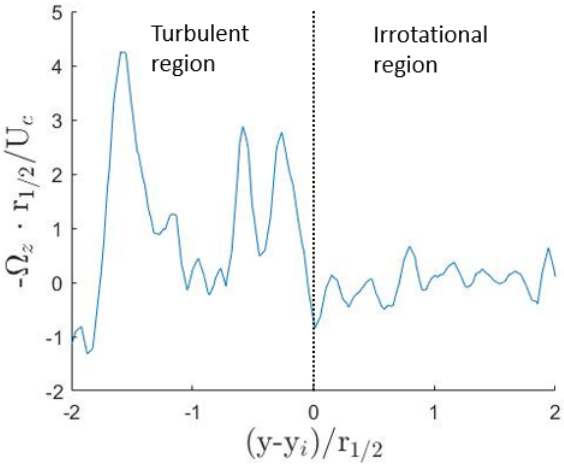

(d)

Figure 28: **(a)** An example of a line along which the conditional vorticity is computed, stretching from -$2r_{1/2}$ to $2r_{1/2}$ distance from the interface. The background represents the instantaneous vorticity field **(b)** The instantaneous conditional vorticity along the line in **(a)** with positive x-axis outside of the contour **(c)** Representation of the lines on difference nozzle distances. Three groups of five lines (with one out of four plotted). It can be noticed that the lines get longer as $r_{1/2}$ increases **(d)** Scaled conditional vorticity profile for one frame, averaged over 810 lines.

6 Results

6.1 Average flow

6.1.1 Self-similarity

In this subsection the self-similarity within each Case and for all Cases relative to each other is considered.
The instantaneous measurements are performed over a large range of Reynolds numbers. Thus, to compare these flows with each other, the principle of self-similarity of the jet is used. For this, large-scale quantities like U_c and $r_{1/2}$ are needed to properly scale and compare the cases. The specific Reynolds number Re per Case can be found in Table 7, which contains repeated data from Table 4.
Self-similarity within each Case is verified and for Case 1 plotted in Figure 29b to 29d. Since these measurements are the closest to the nozzle they are expected to be the earliest in development. The data is compared to these of Ref. [16] with a comparable Reynolds number of 2×10^3. While the profile of velocity fluctuations of Ref. [16] is clearly still developing, Case 1 seems self-similar in velocity, velocity fluctuations and Reynolds stress for $x/D_n \leq 30$s. The developed profile seems to be comparable, apart from the fluctuations outside of the jet. This will be compared to the measurement accuracy in the next paragraph. The profile for Reynolds stress seems to be developed as well. There is no data of Ref. [16] to compare this to, but other experiments have shown similar peak values of around 0.02, after similar normalization with the centerline velocity [33, 39]. The half-width of the jet, which is used for the scaling, is found as a function of distance from the nozzle by finding the distance where the velocity is half of the velocity at the center in the average velocity profile, as can be found in Figure 29b.

To map the behaviour of the jet of different Reynolds numbers in comparison with each other, these profiles are computed by scaling the profile at all velocity grid points and averaging them. This can be found in Figure 30b to 30d. The velocity profile in Figure 30b seems to be comparable for all cases and to the data of Ref. [16]. In Figure 30c the velocity fluctuations are compared. The fluctuations of the velocity are clearly differing from Case 1 and the results of Ref. [16]. Other than Case 1 they seem to be comparable. The difference in Case 1 may be due to the low Re, which is slightly below 2×10^3. At this Reynolds number the jet might not be fully turbulent [29]. Comparing the rest of the cases to results from a higher Reynolds number study of Ref. [58] and Ref. [39], who both found a value of around 0.29 for $\frac{u_{\text{rms}}}{U_c}$, the result of 0.3 as peak value is not irregular.
Again, it can be seen that the velocity fluctuations for all cases outside of the jet are higher than would have been expected comparing to Ref. [16]. This might be due to noise in the PIV measurement. This difference can be translated to pixel displacement for every every case, by converting the u_{rms} in the center of the FOV to pixel displacement using pixel size and Δt from Table 4. Assuming a safe maximum difference in $\frac{u_{\text{rms}}}{U_c}$ of 0.05, the displacement ranges from 0.12-0.21 pixel. This is in line with expected random errors in PIV, considering a window size of 16 pixels [2].
This can be extended to find the error in the velocity profile. By assuming the $\frac{u_{\text{rms}}}{U_c} = 0.05$ in the background, where the average velocity is assumed to be zero, as seen in Figure 30b, to be equal to standard deviation of the velocity, σ_u. This can be extended to find the standard deviation of the average,

$$\sigma_{\bar{u}} = \frac{\sigma_u}{\sqrt{N_F}} \tag{6.1}$$

where N_F is the number of frames, which is a very conservative assumption to the amount of the independent data-points used for the average. Including a confidence interval of 95% this translates to an error range for the scaled average velocity $\frac{U}{U_c}$ of 3.7×10^{-3} to 4.7×10^{-3}, dependent on the Case.

Table 7: The Reynolds number per Case. Repetition of data from Table 4.

Case	1	2	3	4	5	6	7
Re	1.9×10^3	2.4×10^3	4.6×10^3	1.2×10^4	1.2×10^4	3.1×10^4	4.8×10^4

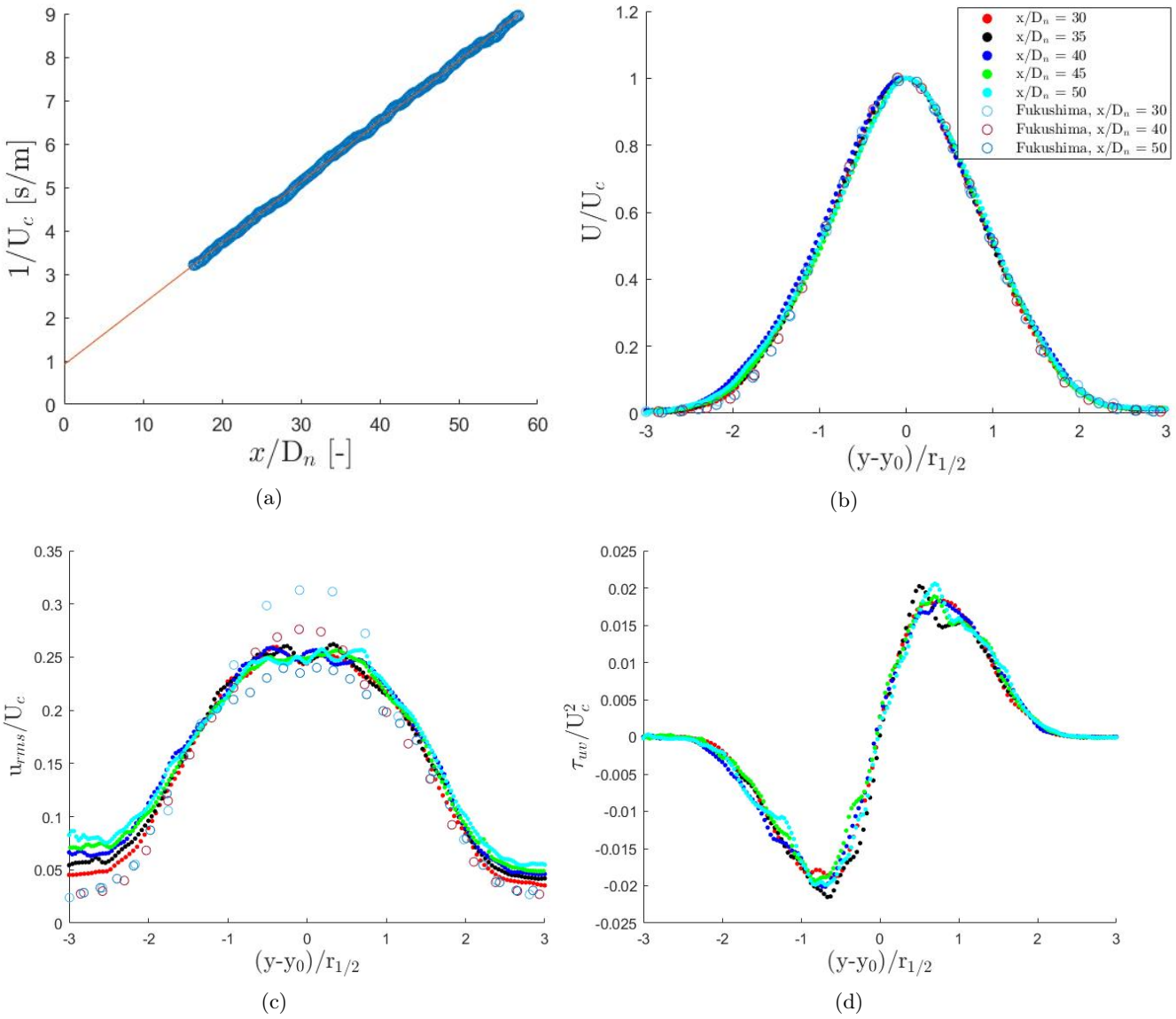

Figure 29: **(a)** The inverse centerline velocity used to identify B_u and x_0 shown for Case 1. **(b)-(d)** The comparison of respectively the velocity, velocity fluctuations and Reynolds stress in y throughout the FOV of Case 1 to data of Ref. [16], noted as Fukushima in the legend. Shown at different distance from the nozzle, to investigate self-similarity within the Case.

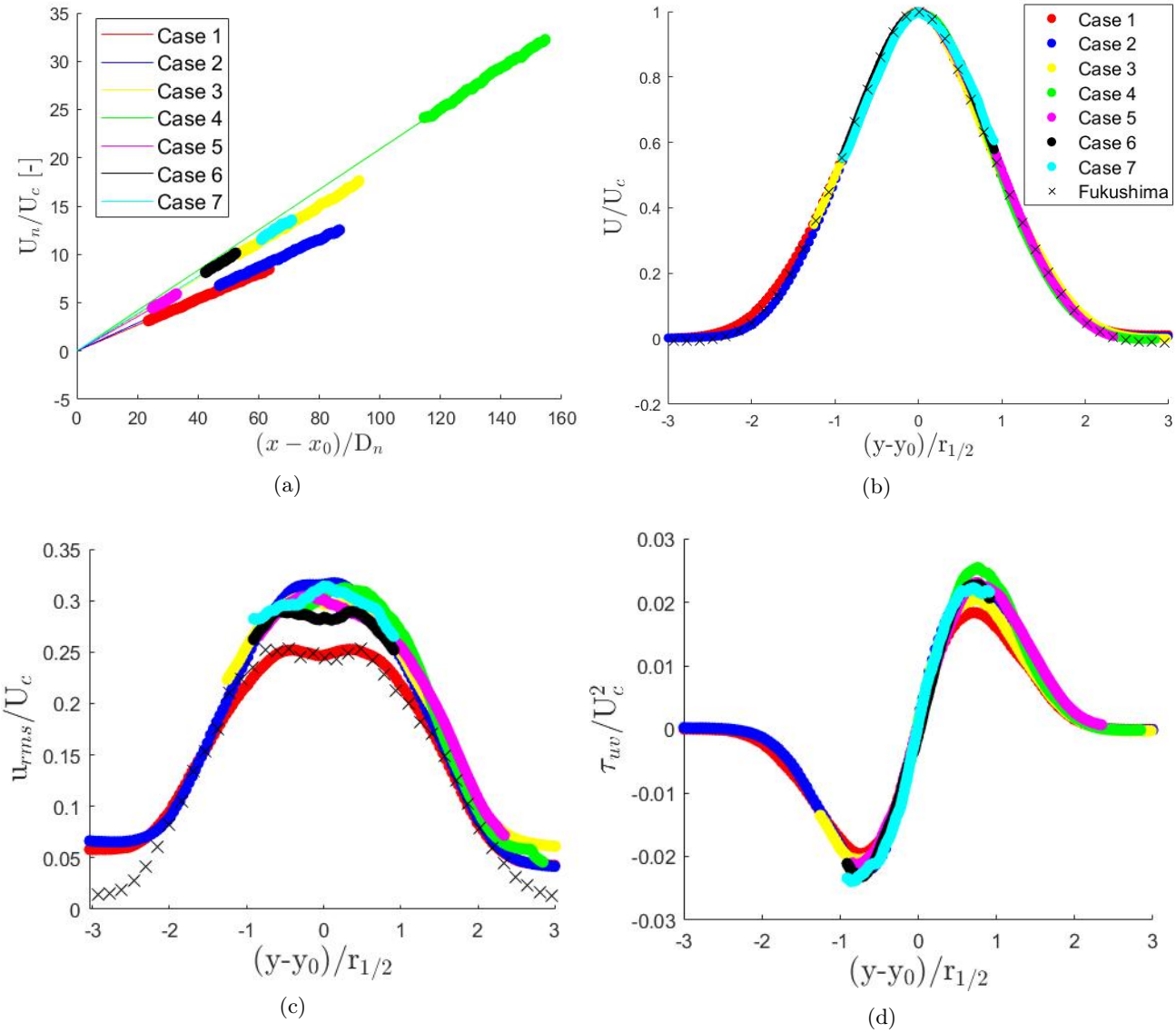

Figure 30: **(a)** The inverse centerline velocity scaled with U_n for all cases. **(b)-(d)** The comparison of the scaled average of respectively the velocity, velocity fluctuations and Reynolds stress in y for all Cases to data of Ref. [16], noted as Fukushima in the legend.

6.1.2 Length scales

The length scales within each Case can be found in Figure 31. The Kolmogorov scale η is found by using Equations (1.5) and (4.1). The outcome can be found in Figure 31a. Comparing this to our design η of 9.5×10^{-5} m the length scale is slightly higher with 9.4-14$\times10^{-5}$ m at the center of the FOVs. All Cases capture η in the range 9.6-10$\times10^{-5}$ m and are thus very comparable to each other and the estimated η in chapter 4. The spatial resolution for each measurement, estimated as the dimension of the interrogation domain, ranges from 2.3η-4.0η based on the Kolmogorov scale in the middle of the FOVs. This spatial resolution is comparable to other research, for example Ref. [7] and Ref. [53], and is sufficient to assume the velocity data as fully resolved [51]. The Taylor scale is estimated using Equation (1.6) at the centerline of the jet. The separation in scales is estimated using the ratio in the middle of the FOV. In Figure 31c it can be seen that the ratio of $\frac{\lambda}{\eta}$ ranges from 16 to 42, a factor of over 2.5 in range. This Figure also includes the assumed separation during the design of experiments, as computed via Equation 4.2. As can be seen the separation of scales is as expected.

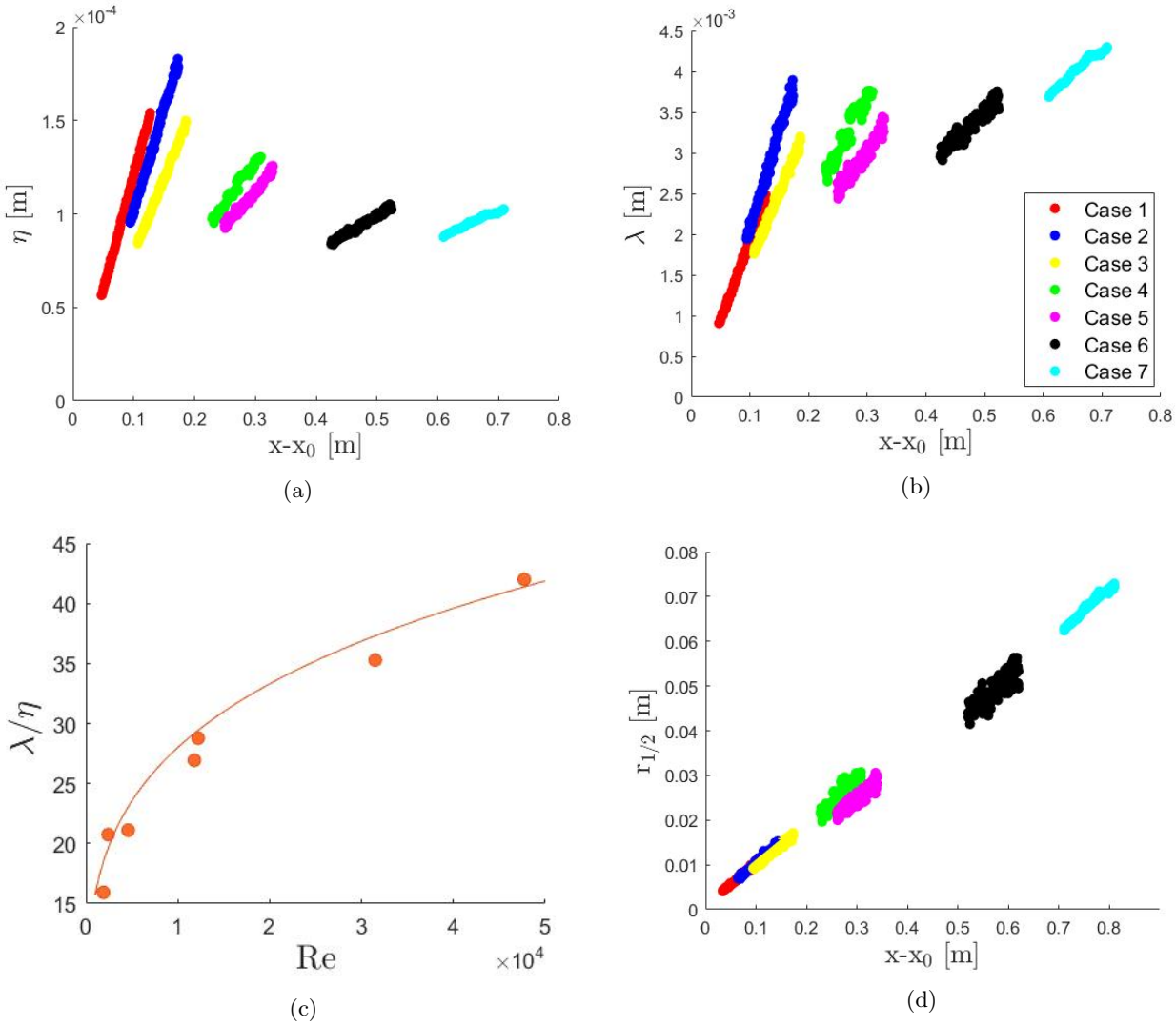

Figure 31: The length scales for all cases. (a) The Kolmogorov scale η. **(b)** The Taylor scale λ. **(c)** Separation of the scales per Case as measured. Included is the theoretical line found by Equation 4.2 and plotted in Figure 10b. **(d)** The jet half-width $r_{1/2}$.

Table 8: The Reynolds number per Case. Repetition of data from Table 4.

Case	1	2	3	4	5	6	7
Re	1.9×10^3	2.4×10^3	4.6×10^3	1.2×10^4	1.2×10^4	3.1×10^4	4.8×10^4

6.1.3 Decay rate, spreading rate and virtual origin

The decay rate B_u and virtual origin x_0 are identified using Figure 30a in combination with Equation (1.2). The virtual origin x_0 is assumed as the distance for which $\frac{1}{U_c} = 0$. The spreading rate K_u is found via Equation (1.3). The location of $r_{1/2}$ is found and by linearly fitting this relative per distance from the nozzle one value for K_u can be found. All constants per Case can be found in Table 9.

Most of the cases seem to have similar decay of the jet, with the exception of Cases 1,2 and 4. Case 1 and 2 have a higher decay constant than the other cases. This might be due to the influence of the initial velocity profile at the nozzle, as investigated by Ref. [6]. They found that a top-hat initial velocity profile, which is comparable in this case to a not fully developed turbulent outflow at the nozzle, will result in higher decay. This could be an explanation for the difference seen here, with Case 2 lying in between Case 1 and the other cases since it is more developed but not completely developed yet.

Case 4 seems to have a lower decay constant than expected. This Case is measured a relatively longer distance from the nozzle. It is possible that these measurements are performed slightly out of the self-similar region and

into the mixing region, which could explain the lower decay rate.
For the spreading rate, it again seems that Case 1 and Case 2 are slightly deviating. This is again assumed to be due to the difference in velocity profile at the nozzle exit, which can lead to a difference in the spreading rate as described by Ref. [6].
Another difference in spreading can be noted between the lower and higher nozzle diameter. There is difference explanations as to why this might be, one of them being the influence of the sidewalls. As mentioned in Chapter 4, influence is expected for $\frac{A_n}{A_{tank}} < 10^{-5}$. This is the case for the larger nozzle diameter, but not for the smaller. Another cause might be a difference in relative roughness. The nozzles are fabricated using a 3D printer in ABS plastic. Ref. [3] found a roughness in width of ABS of order 40 μm under comparable printing conditions, this would lead to a relative roughness at the nozzle of order 0.02 for $D_n = 2$ mm and 0.004 for $D_n = 10$ mm. A smoother pipe leads to a flatter velocity profile in the middle-section of the pipe, and a flatter profile can lead to a lower spreading of the jet [6].

Table 9: Overview of values for B_u, K_u and x_0 as computed per each case. Supplemented with values obtained in experiments and simulations from literature, Adapted from Ref. [6] and Ref. [32].

Case (see Table 7)	*Re*	Decay rate B_u	Spreading constant K_u	Virtual origin x_0
1	1.9×10^3	7.5	74.3	-6.5D_n
2	2.4×10^3	6.9	74.5	-15D_n
3	4.6×10^3	5.3	79.8	-6.3D_n
4	1.2×10^4	4.8	55.2	-0.1D_n
5	1.2×10^4	5.6	102.8	1.1D_n
6	3.1×10^4	5.2	104.3	9.6D_n
7	4.8×10^4	5.2	94.1	10D_n
Ref. [16]	2.0×10^3	6.7	84.9	6.8D_n
Ref. [6]	2.4×10^3	5.9	76.1	4.9D_n
Ref. [33]	1.1×10^4	6.1	75.2	-
Ref. [39]	8.7×10^4	5.9	93.7	-
Ref. [58]	$\sim 10^5$	5.7	93.7	3D_n
Ref. [21]	$\sim 10^5$	5.8	78.4	4D_n

6.1.4 Symmetry and back-flow

The difference between a sidewall and the free surface is investigated and plotted in Figure 32. For the velocity, the two cases seem to overlap very well. However it can be noticed that there is a slight asymmetry for both. The lower side of the jet is wider than the upper side. As mentioned in the previous subsection, a change in width of the jet can be due to multiple factors, one being initial conditions. This asymmetry doesn't fall into measurement accuracy, as determined previously, thus this difference is assumed to be due to initial or boundary conditions.
In terms of initial conditions, previous research has found an asymmetry in velocity profile after a bend in the pipe, similar to our geometry [19]. As suggested by Ref. [19] this asymmetry in the mean velocity profile should be gone before 50 pipe diameters, with the current setup around 30 pipe diameters between the bend and the nozzle.
In terms of boundary conditions, there is a difference in boundary conditions of a free surface on the upper side and a wall at the lower side. However, it is unlikely for the two Reynolds numbers to be affected in a similar way by this, due to the difference in relative distance from the boundaries relative to the diameter of the nozzle, as discussed in Chapter 4.
In Figure 32b it can be noticed that the relative fluctuations in the center are different for both Reynolds numbers. It could already be noticed at Figure 30c that Case 2 is the odd one out here. For Case 2 the symmetry is only off for $\frac{|y-y_0|}{r_{1/2}} > 2$. As found previously for u_{rms}/U_c this falls within the measurement accuracy.
In Figure 33 we look at the back-flow within Case 4. This is done by virtually releasing particles in the top of the average flow field of the whole data set, and examine these streamlines of the flow. In Figure 33a, it can be seen that the streamlines in the average flow field are not vertical all the way through the image, meaning on average there is a flow towards the nozzle in the background there.
To see whether this a time-dependent issue, the average streamwise velocity of different regions is investigated in Figure 33b. This shows the average streamwise velocity in time for the whole image, square 1 and square 2, as indicated in Figure 33a. There seems to be no trend in these velocities, so the amount of back-flow did not seem to be changing throughout the measurement. If the back-flow would be changing, this would suggest

it may be caused by , which would make our flow time-dependent. However, due to the consistency of the observed back-flow, it is more likely a consequence of the finite flow domain [32]. This could be verified or further investigated by looking at measurements closer and further away from the nozzle, to see if similar behaviour at similar distance from the wall or surface is noticed.

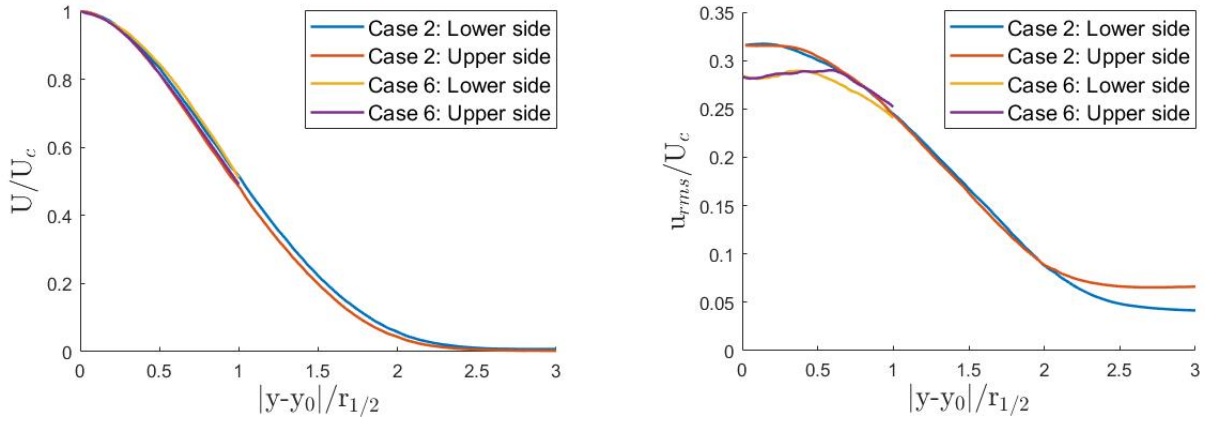

(a) (b)

Figure 32: The symmetry of the jet is investigated at Case 2 and 6. This is done by comparing scaled averages of the whole image of the upper and lower part of the jet.**(a)** The averaged scaled velocity as a function of the distance from the centerline of the jet, scaled with the half-width.**(b)** The scaled velocity fluctuations as a function of the distance from the centerline of the jet, scaled with the half-width.

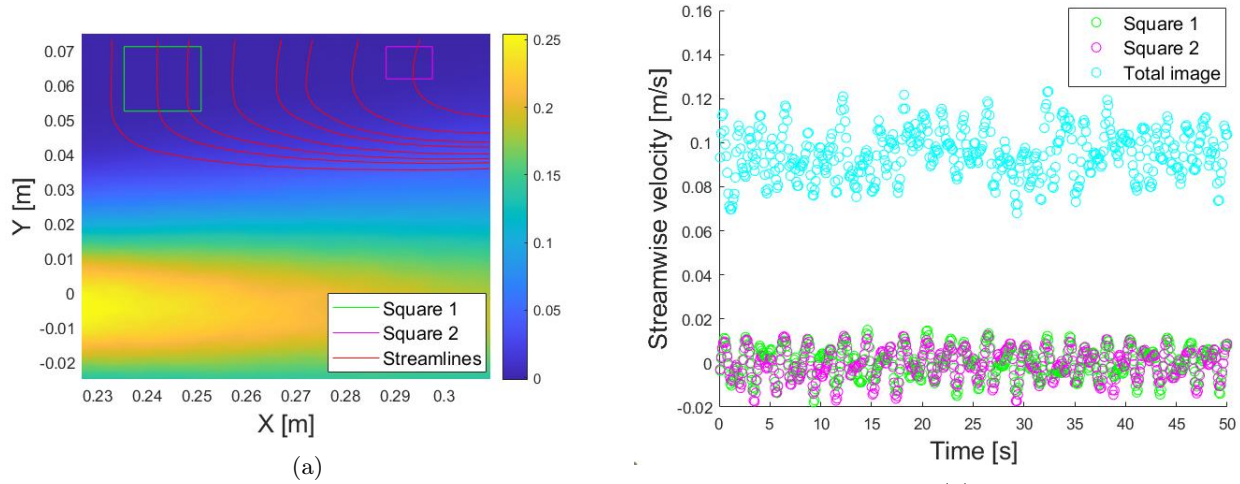

(a) (b)

Figure 33: **(a)** Streamlines for the average velocity field of Case 4. The color-scale represents the streamwise velocity. **(b)** The average streamwise velocity within the squares in **(a)** as well as the total image over the total duration of the measurement.

Table 10: The Reynolds number per Case. Repetition of data from Table 4.

Case	1	2	3	4	5	6	7
Re	1.9×10^3	2.4×10^3	4.6×10^3	1.2×10^4	1.2×10^4	3.1×10^4	4.8×10^4

6.2 Conditional average

In this section the results from the conditional averages can be found. First, the results of the profile for the conditional averaged vorticity over the interface of the jet as a function of the threshold will be discussed in subsection 6.2.1, after which the results for the whole range of Reynolds numbers will be presented in subsection 6.2.2. The measured width and scaling of the interface is shown and compared to literature in subsection 6.2.3. The validity of the profiles is discussed in 6.2.4, and in 6.2.5 potential improvements are investigated.

6.2.1 Threshold dependency

In Chapter 5 it was shown that the position of the instantaneous jet interface varies with the chosen threshold. The change in location between these contours can also be seen in Figure 34a for a wider range for Case 1. It can be noticed that close to the nozzle the contours are very close to each, overlapping even, while further away they differ. This is found to be an effect of decreasing concentration as the jet widens further from the nozzle, as will be shown in section 6.2.5.
Since there is different theories on the computation of the contour, as explained in chapter 5, the difference in mean conditional vorticity profile per threshold is examined. In Figure 34b it can be seen there is a significant difference. It is remarkable though that, even with the inwards movement of the contour further away from the nozzle, a clear jump can still be noticed. The inward movement might however be balanced by the omitting of data points when there is no contour present, which is likely to happen for these higher thresholds further away from the nozzle. Note that all these thresholds are all still within the sharp jump in concentration profile, as can be seen in Figure 34c and 34d, in which the first is closer by the nozzle than the latter. In order to quantify this change in profile the slope, and from that width, of the jump are considered.
All profiles in Figure 34b have a clear linear region, and by fitting a tangent line on these regions the slope of the profile can be found. By identifying where the profiles start deviating from the tangent a vertical jump or 'height' of the jump can be defined. The locations at which the tangent starts deviating more than 1%, and thus from where the height is calculated, are plotted in figure 34b as points. The height together with the slope provides us with an estimation of the width of this jump, equal to the width of the linear region.
The slope and width as a function of the threshold for Case 1 can be found in Figures 34e and 34f. The slope seems to be very dependent on threshold, while the measured width of the jump seems to be relative insensitive on the used threshold.
This leaves the question what profile can be considered the 'correct' one and provide accurate slope/width measurement. It can be seen that the slope works towards a peak value at a threshold of ϕ. From this, the assumption is made that the correct shape is that of the the profile for ϕ.
For the width it can be seen that mainly the profile for 0.25ϕ gives a very different outcome. From Figures 34c and 34d it can be noticed it does lie above the noise level of concentration around the jet and on the jump of concentration at the jet edge. It can however also be seen that there are some sides where the jump is less sharp, and this could have an influence. It might also be that that noise level of vorticity is higher, reaching above 0.25ϕ, but this would have to be verified.
The weak dependency of the position of the contour on threshold is often used as support of the insensitivity of the results on the threshold [43, 54], however, it can be seen that it can have a significant effect on the profile, measured slope and potentially width, depending on the method of computation of the latter.
Also, the presence of a sharp jump is often used to ensure the interface detection has succeeded [31, 54]. However, it can be noted this jump can be found for a variety of thresholds. And this thus doesn't necessarily indicate an appropriate threshold is chosen. A shape similar to Ref. [54] can be seen around 0.5-1ϕ, of which the value of peak of the mean vorticity, $\sim 0.6 U_c / r_{1/2}$ and the scaled constant value, $\sim 0.55 U_c / r_{1/2}$ seem to be comparable to our results. The shape for the vorticity profile found in Ref. [31] is more similar to the contour of 0.25-0.33ϕ.
It would be very interesting to see whether this change of shape is similar on other Reynolds numbers, and if the change in slope follows a similar trend. This would help in defining more universal ways of quantifying the interface.

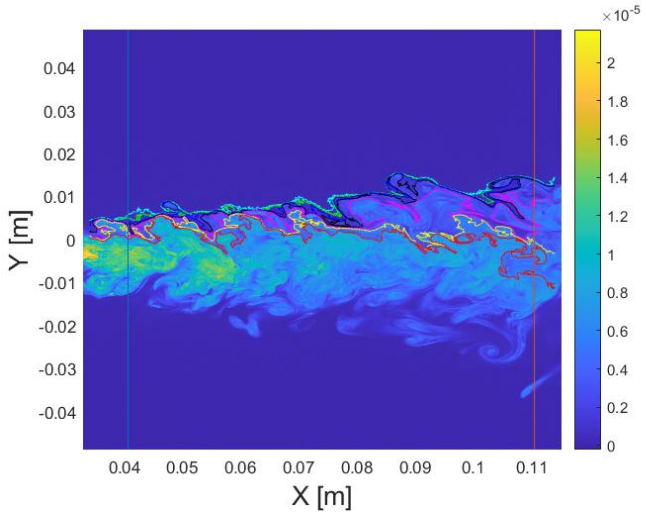

(a)

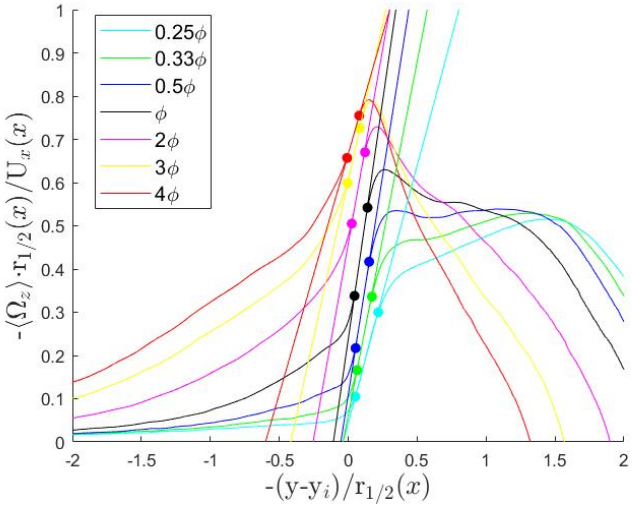

(b)

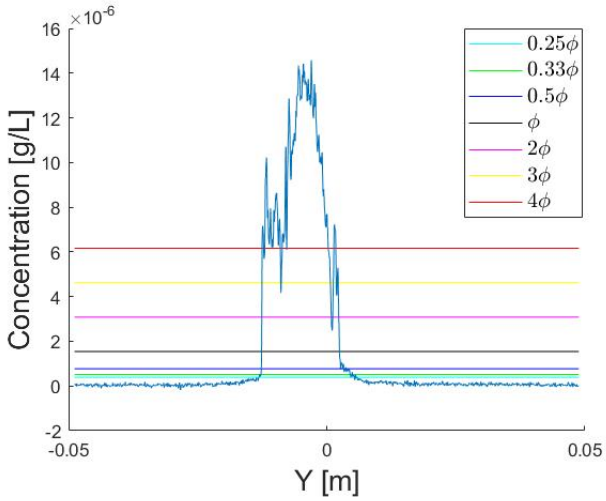

(c)

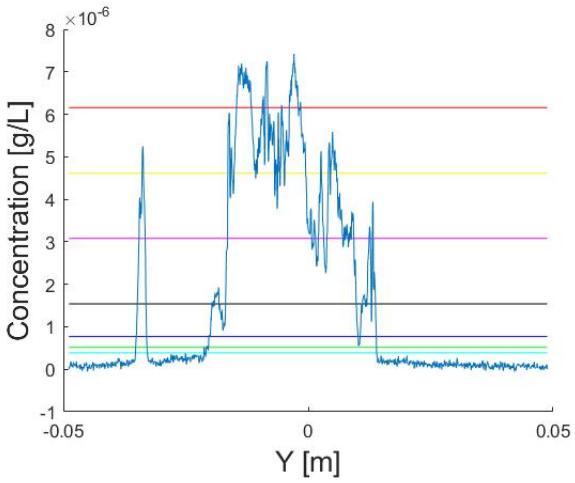

(d)

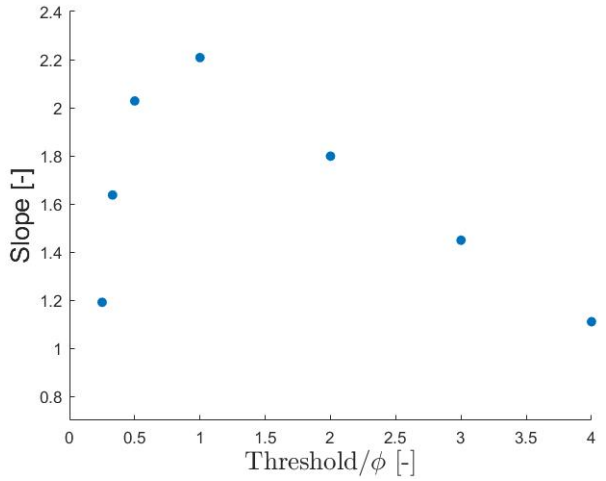

(e)

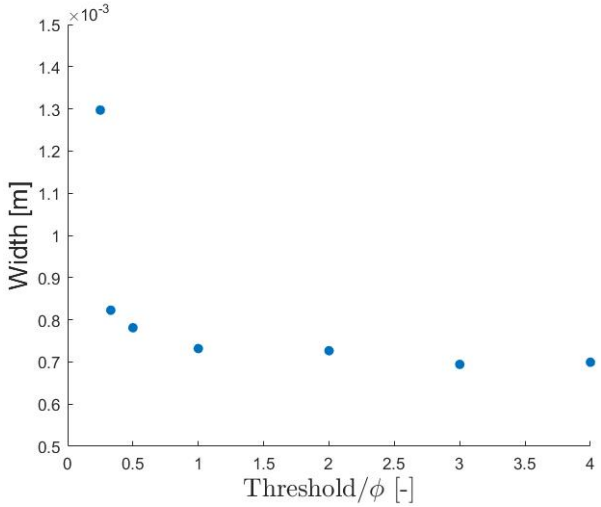

(f)

Figure 34: **a)** Different upper contours on the jet in Case 1 of frame 400 for thresholds varying from 0.25ϕ up to 4ϕ. **b)** Scaled conditional vorticity profile for the range of thresholds. It can be clearly seen that the shape of the profile is very dependent on the choice of threshold. Added are the tangents and points used to determine the slope and width of the profile. **c)** The concentration profile in $y-$direction along the blue vertical line **a)**. **d)** The concentration profile in $y-$direction along the orange vertical line in **a)**. **e)** The slope of the profile as a function of the threshold. **f)** The width of the profile as a function of the threshold.

6.2.2 Conditional vorticity profile

In Figure 35a the mean conditional vorticity profiles can be found for all Cases. It can clearly be seen that their shape differs significantly for the different Reynolds numbers. As shown in the previous section, one of the possibilities for such a difference in shape is a difference in threshold. We assumed the correct profile as the profile for ϕ based on the slope in the previous section and the profiles from the other Cases can be compared to that. By linking the shapes of the conditional vorticity profiles in Figure 35a to those in Figure 34b, it can be estimated whether the slope and width will be over- or underestimated per case. The comparisons to shapes from Figure 34b can be found in table 11 together with the scaling of the slope of Case 2, 4, 5 and 6 according to this.
In Figure 35b it seems clear that there is a dependency of the slope on Reynolds number. It is a lot more sensitive to threshold than the width. However, the slope of a linear region leaves little room for interpretation differences and could be a more stable way to compare different research. The investigating of the change of slope per threshold on a variety of Reynolds numbers, as proposed in the previous subsection, could, together with this results on Reynolds number dependency, help universalise this method of interface scaling. It could also help to verify the validity of the jet contour in a more quantitative way.
The variety of different contour shapes make it difficult to compare the profiles to each other in a well-defined way. This emphasizes the importance for an universal and stable procedure for determination of the jet contour, for which the difficulties are explained in Chapter 5.

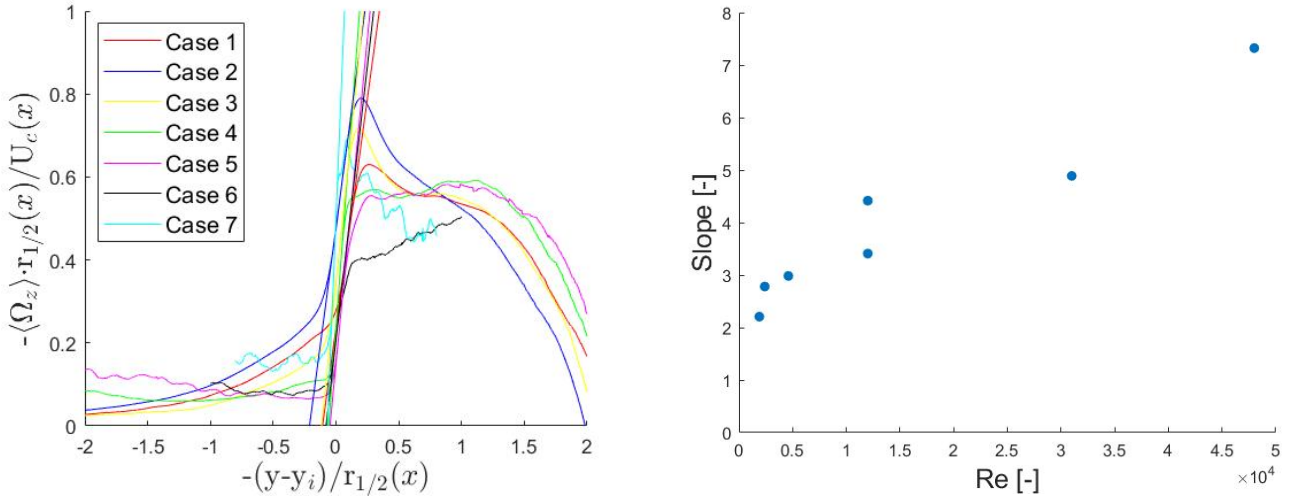

(a) (b)

Figure 35: **a)** The mean conditional vorticity as a function of the distance from the interface for all cases. The tangents of the jump are added to each Case to find the slope. **b)**The slope as a function of the Reynolds number.

Table 11: The linking of the shapes from all Cases in Figure 35a to the threshold dependent shapes in Figure 34b. All profiles that do not link to the shape of ϕ are scaled according to Figure 34e.

Case	Re	Similar shape	Old slope	New slope
1	1.9×10^3	ϕ	3.1	-
2	2.4×10^3	2ϕ	2.3	2.8
3	4.6×10^3	ϕ	3.0	-
4	1.2×10^4	0.5ϕ	4.1	4.4
5	1.2×10^4	0.5ϕ	3.1	3.4
6	3.1×10^4	0.25ϕ	2.6	4.9
7	4.8×10^4	ϕ	7.3	-

6.2.3 Width and scaling

Next, we can look at width of the interface, and its relation to the length scales of the flow. In order to find a trend for the scaling of the interface, it is necessary to perform some error estimations. Since the error might be differing per Case, this is done for Case 1 and 7 to get a idea of the whole range.
The accuracy of the vorticity measurements is found by estimating the standard deviation of the vorticity in the background region, where the flow is expected to be irrotational. This is done by averaging the vorticity in each frame over a rectangle; extending over the whole $x-$domain while staying clear of the boundaries and the jet. It is assumed that the standard deviation of the vorticity of this data-set from the background is similar in the jet.
Using this standard deviation σ_ω the standard deviation of the conditional mean profile $\sigma_{\bar{\omega}}$ can be computed using Equation (6.1) and the 95% confidence interval via $1.96\sigma_{\bar{\omega}}$. By using U_c and $r_{1/2}$ for scaling, the error in the conditional vorticity profiles can be estimated. The error in the slope is found by considering the minimum and maximum slope in-between the error bounds and from there the error in width.
The width for all Reynolds numbers including error bars is plotted compared to respectively the Kolmogorov and the Taylor scale in Figures 36a and 36b.
The width seems to increase strongly with the increase of the Reynolds numbers. For the lower Reynolds numbers, the width seems to be around 10-15η, or around 0.5-0.6λ. This is very comparable with values found in literature, where values of around $\mathcal{O}(\lambda)$ and around an order of magnitude higher than η are found for the interface thickness for comparable Re [5, 23, 43, 52, 54].
For axisymmetric jet there are no results for our highest Reynolds numbers. As mentioned in Chapter 1 a scaling on η has been found for plane-jets by Ref. [43], finding an interface thickness of around 10η for a large range of Reynolds numbers. In the current results there seems to be a deviation of this scaling, with the results for Case 7 around a factor three higher.
It has to be noted that these error bars are representing the error due to PIV in the vorticity. As noticed in Figure 34f a potentially significant source for error could be an inappropriate threshold. For Case 6, resembling the 0.25% profile from Case 1, this could mean a difference of a factor 1.8 in width. This would lead to a result of around 10-15η, which would indicate a scaling with η.
In order to present conclusive results on this, it is necessary to review the highest two Reynolds numbers. Either by doing a similar analysis as for Case 1; varying the threshold and identifying the different (and correct) threshold via there. Or, since current method is used for its ability to do threshold detection on all Cases, look in more detail on the specific ways for threshold determination for these Cases.
Throughout the literature multiple definitions to define the thickness of the interface are being used. Another way of calculating the width is by using the entrainment velocity to find a characteristic length scale [30]. It would be interesting to do this for current data using two consecutive LIF frames in combination with the velocity vectors from PIV.
Another step in this would be to link this scaling and velocity to the physical process of entrainment, nibbling and engulfment, as explained in Chapter 1. The measurements that are performed with a moving camera, following the design in Chapter 4, could be of help for that.

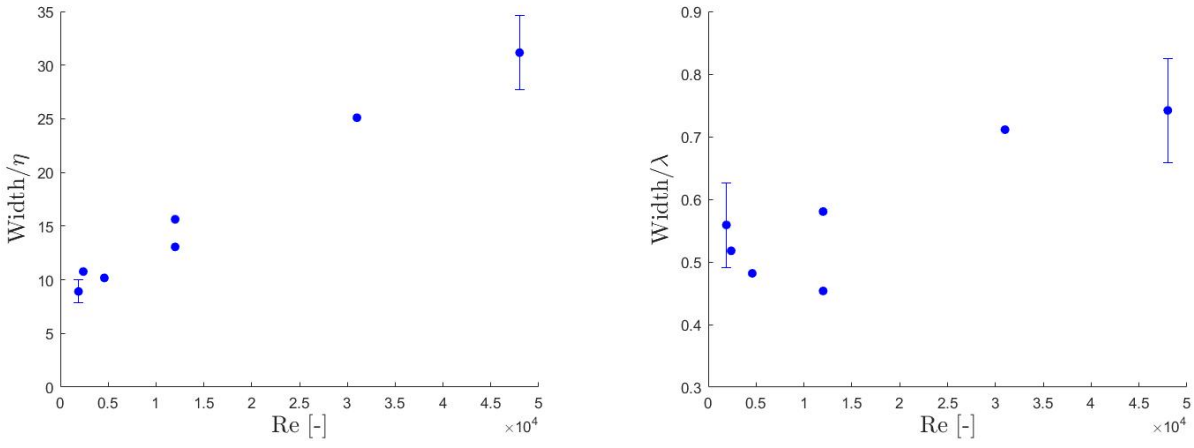

(a) (b)

Figure 36: **a)** The width scaled with Kolmogorov scale. Error bars are added for Case 1 and 7. **b)** The width scaled with Taylor scale. Error bars are added for Case 1 and 7.

6.2.4 Validity of the profiles

In order to draw a conclusion on the scaling of the thickness, it is important that the interface is resolved. This can be validated by comparing the conditional vorticity jump with the PIV spatial resolution. In Figure 37a the scaled conditional profiles are plotted for Cases 1, 4 and 6. The spacing between data points equals the PIV vector spacing, which is equal to 1/2 the interrogation window width. It can be noticed that for Case 1 the interface is covered by at least 4 data points and assuming that the spatial resolution of a PIV measurement is given by the interrogation window width, the interface width is resolved in this case. For Cases 4 and 6 the interface is covered by more data points. Thus, also in these cases the interface is properly resolved.

The conditional vorticity profiles are averaged over lines the intersect the contour perpendicularly. To ensure that a converged profile is reached, a different spacing for these lines is considered. This is done for Case 1, as can be seen in Figure 37b. The profile is computed by using a spacing of 1, 1/2, 1/3 and 1/4 times Δx in-between perpendicular lines on the interface. It can be seen that convergence is reached at a spacing of $\Delta x/3$, which is what has been used for all cases.
It can still be noted in Figure 35a however that some profiles appear to be smoother than others. This is caused by the varying number of data point in the conditional average due to other factors. The amount of data points is influenced by multiple factors; Among others the spatial resolution and the total amount of frames in the data set. But data is also taken away whenever the perpendicular line goes out of range of the FOV, or whenever there is no interface or an interface which is only partially present in the FOV. In Figure 37c the average amount of data points N_{dp} that is used for the final conditional vorticity profile can be found.
For the higher Reynolds numbers, the relative size of the FOV compared to the half-width of the jet (and therefore the deviation of the interface location [54]), is a limiting factor. In Figure 37c this ratio can be found, which shows it has an influence of the total amount of data points used. This becomes even more clear in Figure 37d, where the distribution is shown for the maximum and minimum case. For Case 7 it can be seen that this relative small FOV causes the line to go out of range.
Because of this it has been chosen to only plot the region closer to the interface, the 'core', for Case 6 and 7 in Figure 35a. For Case 3 it can be seen that inside the jet there is a asymmetrical loss in data points. This is assumed to be due to interface not being located in the center of the FOV, causing the perpendicular line to exceed beyond the boundaries of the FOV on one side more than the other.
There is a couple of things that can be done to create a smoother profile for the higher Reynolds numbers as well. In order to increase the interface more present, the FOV could be increased, this would however decrease the spatial resolution. As found in Chapter 4 there is some room for that, however, this is limited and will probably not significantly reduce the issue. It is also possible to take more snapshots of the jet and increase the amount of data points due to that. However, the deflected flow from the end wall and build up of particles and dye (as discussed in Chapters 4 and 5) makes this unpractical in the current experimental setup.

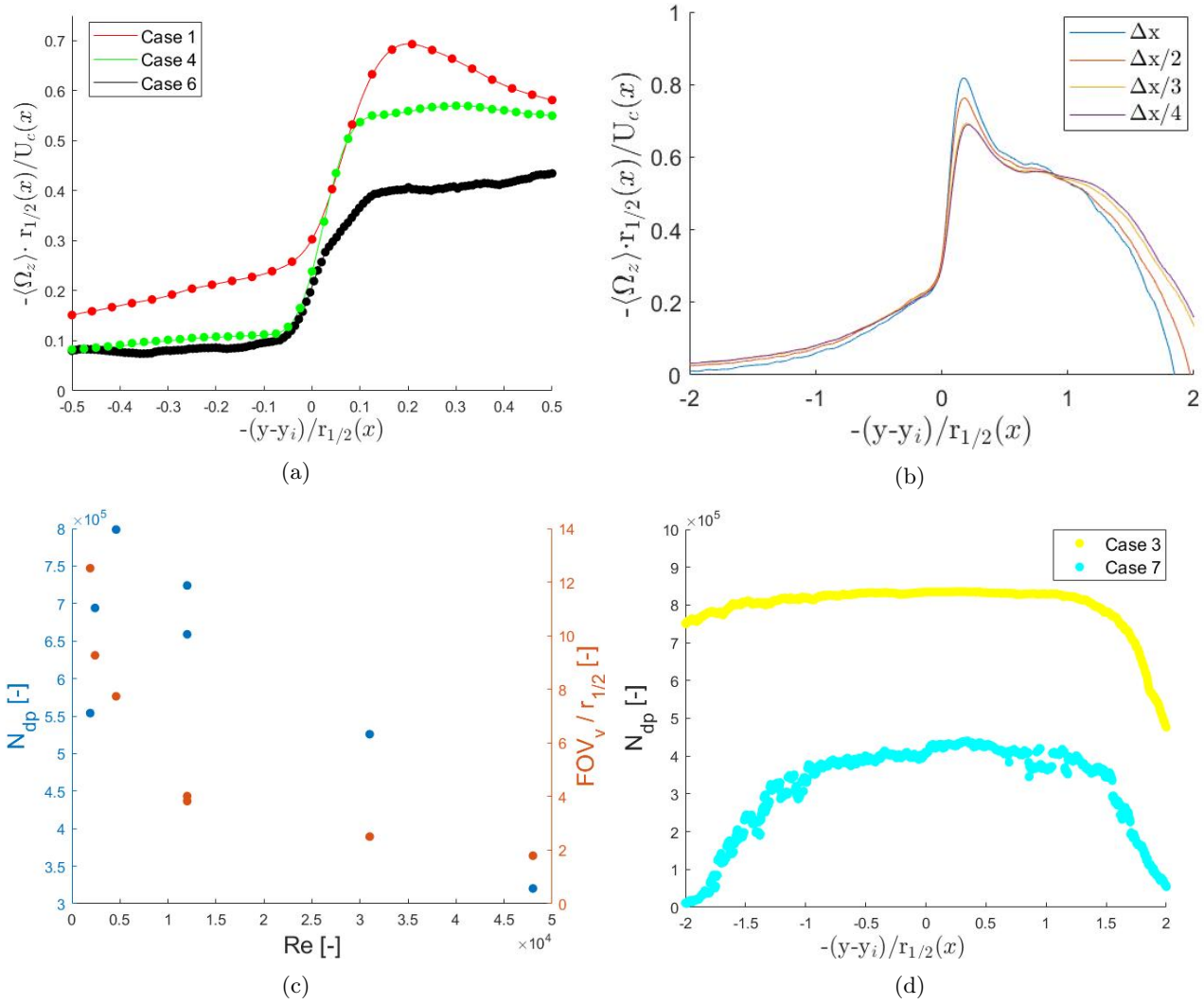

Figure 37: **a)** Visualization of the vector spacing Δx on the mean conditional vorticity profiles of Case 1, 4 and 6 where the points note the vector spacing. **b)** The influence of the spacing in x between the perpendicular lines on the interface on the profile of Case 1, for varying vector spacing Δx. **c)** The average amount of data points used as and the ratio of the FOV and half-width per Reynolds number. **d)** The distribution of the amount of data points used along the vorticity profile for the minimum and maximum case of **c)**.

Table 12: The Reynolds number per Case. Repetition of data from Table 4.

Case	1	2	3	4	5	6	7
Re	1.9×10^3	2.4×10^3	4.6×10^3	1.2×10^4	1.2×10^4	3.1×10^4	4.8×10^4

6.2.5 Difference in computation definitions

As mentioned in section 6.2.1, the contours in Figure 34a have a tendency to run more to the center of the jet, mainly for higher thresholds. Looking at Figure 34c and 34d it can be seen that the same threshold represents a very different part of the jet closer or further away from the nozzle, indicating that an average threshold for the whole image might not be representative for the larger range of concentrations in x. When it is not representative, the contour will be lying more on the inside of the jet further away from the nozzle. This hasn't shown to be a problem in previous research. However, the current range in centerline concentration is greater. To test this hypothesis the concentration of Case 1 is scaled with the average centerline concentration as seen in Figure 22a. The threshold for the scaled data is found to be equal as for the non-normalized data, by using the same method as described in Chapter 5. Comparing the contours in Figure 34a and 38a the isolines of concentration that the contours follow seems to be more as expected.
It would be interesting to see the of location of these contours, also with respect to the mean conditional vorticity profile in Figure 38b. Their relative position could be compared to interfacial thickness and visualize how far from the vorticity jump they are situated. This could give us more insight in the differing of the conditional vorticity profiles based on the threshold.
The intensity profile at two different locations found in Figure 34a and 38a can be seen in Figure 34c, 34d, 38c and 38d. The relative positions of the threshold before and after the scaling with the centerline concentration can be compared. The scaling with the centerline concentration causes a threshold to be along the same relative height closer and further away from the nozzle. It would thus be advisable to always scale with regards to the mean centerline concentration in the future.
By comparing Figure 34b and 38b a difference can be noted in the vorticity profile as well. The vorticity before the jump, outside the jet, seems to be lower, however there is still some vorticity present outside the jet contour before the jump, even when the threshold is low and the contour should theoretically be lying outside the jet boundary.
This can be explained by looking at the conditional concentration profile in Figure 38e. The same trend as before can be observed; a small amount of concentration can be found before the jump, lying outside of the jet. This has not been seen in previous works. Since the trend is found in vorticity and concentration data, it can be argued that this is caused by a difference in the computation of the conditional vorticity profile. In Figure 38f a schematic representation is shown of the difference of computation compared to Ref. [54], where the interface envelope is defined as the most outward point in y and the conditional statistics are computed vertically instead of perpendicular to the interface. It can be noted that by taking vertical lines in combination with an envelope including engulfment more concentration (and thus vorticity) on the 'outside' of the jet is prevented. According to this explanation the small dip just outside the jet, as seen in Figure 38e, can be linked to the average length scale of separation between two interfaces.
A solution to the extra vorticity would be to stop the computation when the interface is crossed again. Due to the shape of the interface, this would drastically limit the amount of data to be averaged over, which is something to consider. Another downside of this method is that it would likely remove more data point of certain orientations. Mainly further away from the jet (as more data points are removed), this could have consequences for the outcome. It is shown by Ref. [5] that for the interface of a turbulent wake there is an influence of interface orientation to the mean conditional vorticity profile. This is also something that might influence the results using a method where the mean conditional profile is computed over vertical lines, thus assuming a certain orientation, or if only the contour with a certain orientation is considered.

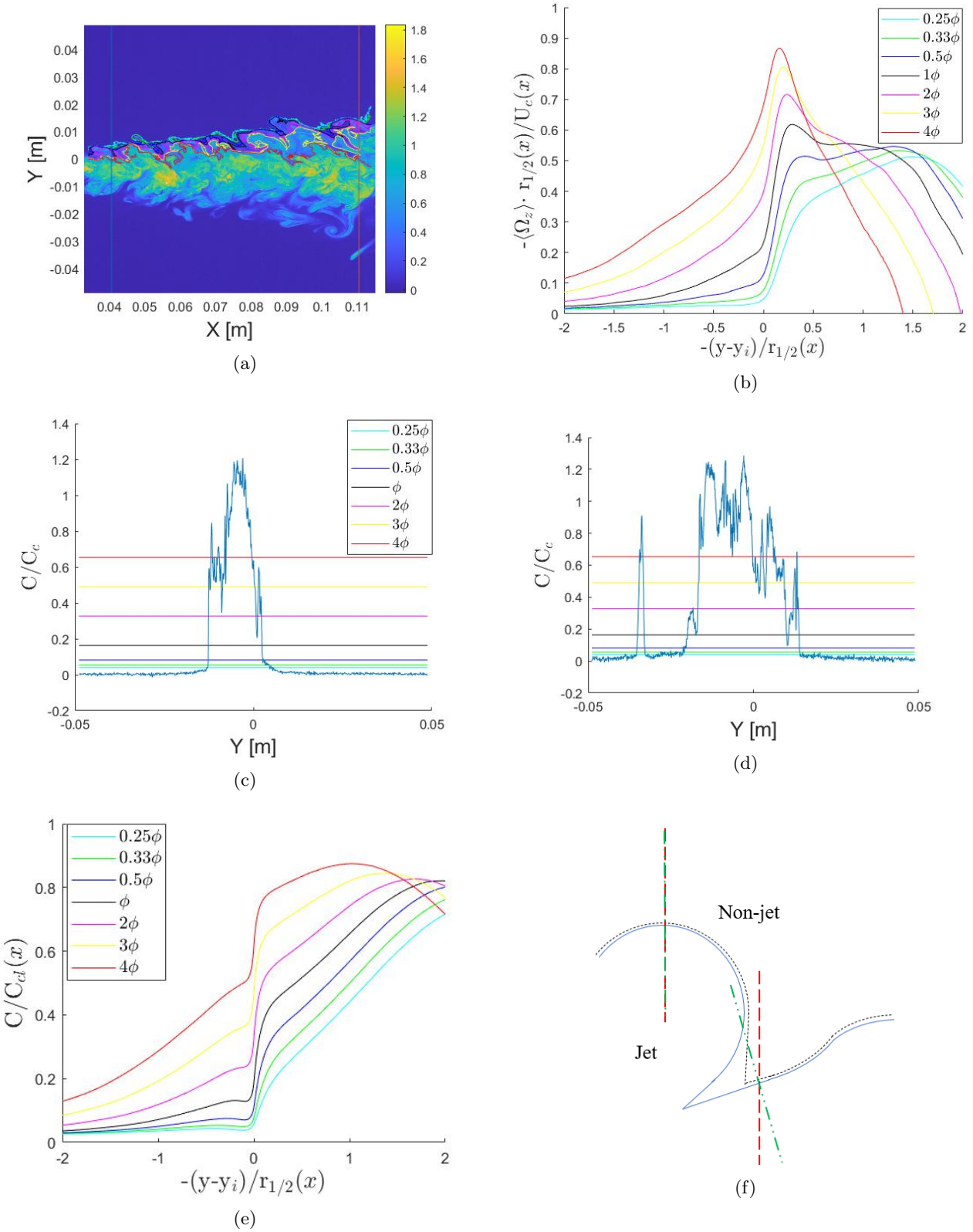

Figure 38: **a)** Different upper contours on the jet in Case 1 for thresholds varying from 0.25ϕ up to 4ϕ after scaled with the centerline concentration. **b)** The scaled conditional vorticity profile for the range of thresholds based on the contours in **a)**. **c)** The vertical concentration profile at the blue location in **a)** including varying thresholds. **d)** The concentration profile on the orange location in **a)** including varying thresholds. **e)** The conditional concentration profile per threshold for Case 1. **f)** The difference in definition between Ref. [54] (red) and present work (green). Note that image is not on scale.

7 Conclusions and recommendations

This thesis describes a novel way of approaching measurements on a large range of Reynolds numbers on the Turbulent/Non-Turbulent interface of an axisymmetric jet. The results of the combined PIV and LIF measurements on the interface over a range in Reynolds number of 1.9-48 $\times 10^4$ cover a total separation of scales (λ/η) of over 2.5 (see Figure 31c). This is similar as designed for and should be sufficient to capture a dependency in scaling of either length scale. This separation of scales is difficult to achieve in simulations or experiments, due to the large range of Reynolds numbers needed to achieve this and the related difficulty of ensuring a sufficient spatial resolution on all Reynolds numbers.

The method proposed in this thesis to perform these measurements at a similar Kolmogorov scale by changing the measurement distance from the nozzle has shown to remove this problem with spatial resolution.The Kolmogorov scale of all measurements range from 9.4-14$\times 10^{-5}$ m at the center of the FOVs, with all Cases capturing the range 9.6-10$\times 10^{-5}$ m. This is very close to the design η of 9.5$\times 10^{-5}$ m (see Chapter 4). The spatial resolution is, with a maximum of 4η, sufficient and slightly better than designed.

By varying the distance from the nozzle to perform measurements, other constraints are introduced, one being a difference in boundary conditions at different locations. The constraints of the experimental setup are outlined in Chapter 4. These constraints can partially be seen in the average flow results of the jets at different Reynolds numbers. A difference in the two used nozzle diameters is noted in the spreading of the jet (see Figure 31d), which is likely caused by the influence of the sidewalls and free surface on the large nozzle diameter. The influence of a side wall versus a free surface might also be the reason for the asymmetry found in Figure 32.

Another possibility for these difference is the nozzle setup. The relative roughness within the nozzle and proximity of the pipe bend could cause the flow to be perturbed and cause asymmetry or a difference in spreading of the jet.

A solution for these issues could be by placing a grid in the pipe leading up to the nozzle to straighten the flow and create homogeneous turbulence. By optimizing the shape and smoothness of the nozzle this could be prevented, and the initial conditions for all Cases will be more alike. This could also solve the issue of Cases 1 and 2 potentially not being fully turbulent, as indicated by Figure 30a.

With one nozzle being more affected by the sidewalls than the other, it would be better for the comparison of all the Reynolds number to have initial and boundary conditions as similar as possible. A tank with a wider cross sectional area could achieve comparable boundary conditions for both nozzles, also preventing the back-flow caused by the walls, as investigated for Case 4 in Figure 33. This is assumed to be due to the presence of the water surface, since it is not a time-dependent issue, but this could be further verified by looking at the other cases. A longer tank would create more practical measurement conditions, with the the end wall limiting the frames per set and sets per day that can be taken.

Regardless of these small differences, the potential of performing measurement in this way is clear. The results show in Section 6.1 that the experimental setup provides self-similar jets for all Reynolds numbers, comparable to the literature in terms of scaled velocity, velocity fluctuations and Reynolds stress with the noise levels in the velocity in line with expectations, verifying the PIV settings designed in Chapter 4.

For the LIF measurements it can be concluded that most cases fall within the linear behaviour of the fluorescence of the Rhodamine, as shown in Figure 22b, except for Case 3. The computed concentration for this case will deviate from the actual concentration due to saturation of the dye. However, this is expected to have no influence on our final results, because the concentration data is solely used for contour detection.

The identification of the threshold to define the contour is challenging due to a few different aspects. The pulse-to-pulse variation of the intensity of the laser causes a difference in intensity in every image, causing a threshold per frame to be needed. Also, there is multiple different methods across the literature to estimate the appropriate threshold without an objective way to validate it. This is of importance though, as shown in the significant influence it has on the mean conditional vorticity profile, as seen in Figure 34b. This could explain why a variety of shapes of mean conditional profiles can be found in literature.

Figure 34b shows there is a necessity for a less subjective and more universal way to determine the threshold and contours of the jet, or a way to remove the importance of choosing the appropriate threshold. The latter could be done by doing more research on the dependency of the slope and width on the shape of the conditional vorticity profile.

It can be concluded from Figures 34b and 35a that in this Thesis the threshold is not ideal for all Cases. The thresholds are chosen by one method for all Cases, but taking a more individual approach per Case might lead

to more accurate results. This could ease the comparison in between Cases and the scaling of the slope and width as a function of Reynolds number.

The slope of the jump, scaled according to the shape of the profile, increases for higher Reynolds numbers. The width found for the low Reynolds numbers, around 10-15η or 0.5-0.6λ, is very comparable with values found in literature for the TNTI of different type of shear flows. For higher Reynolds numbers, there is no data for axisymmetric jets to compare with. Following from Figures 36a and 36b there seems to be a dependency on the Taylor scale, with the width changing around a factor 3 of η over the whole range of Reynolds numbers. With such a difference in scaling, this behaviour should also be able to be noted with a smaller range of Reynolds numbers in the high range, to provide more data in that region. The dependency of the width on the threshold does prevent to draw conclusive results on the scaling of the interface per Reynolds number. For this, additional research is needed for Cases 6 and 7. Either by looking at the threshold dependency for these specific cases, or by optimizing the threshold determination for these cases specifically.

A thing to consider for this is that throughout the literature multiple definitions to find the threshold, contour, mean conditional profiles and thickness of the interface are used. Methods that stop computation when crossing the interface again, define an outer contour or may lead to leaving out part of the interface with certain orientations. This may lead to a bias in (parts of) the conditional mean profile, considering there might be a dependency on interface orientation, as previously shown for wakes [5].

Definitions for defining the thickness of the interface are also varying throughout literature, affecting the ability to compare different research. Another method that is used to find a trend in scaling uses the entrainment velocity. It would be interesting to do this for current data using two consecutive LIF frames in combination with the velocity vectors from PIV. Using the measurements that are performed with a moving camera, as designed in Chapter 4, more insight in the physical process of entrainment, nibbling and engulfment, could be gained as well.

A Measurement conditions

Table 13: Measurement conditions and settings of the traverse mechanism for the measurements with moving camera.

Parameter	Value
X_n [cm]	0.3 - 0.7
Y_n [cm]	0.04 - 0.1199281
D_n [cm]	1
Angle [degrees]	11.3
$U_{trav,x}$ [cm/s]	2
$Acc_{trav,x}$ [cm/s^2]	19
$Acc_{trav,y}$ [cm/s^2]	3.2265705
C_p [mg/L]	110
C_{source} [mg/L]	330
FOV [cm]	10.2x12.1
$T_{water,tank}$ [°C]	22.3
Δt [ms]	4
f-stop PIV camera	8
f-stop LIF camera	5.6

Table 14: Measurement conditions and PIV settings for the stationary measurements.

Case	X_n [cm]	Y_n [cm]	D_n [cm]	Δt [ms]	C_p [mg/L]	C_{source} [mg/L]	f-stop PIV	f-stop LIF	T_{water} [°C]
1	7.4	0	0.2	0.8	59	83	11	5.6	21.6
2	10.4	0	0.2	0.65	76	108	11	5.6	21.6
3	13.4	2	0.2	0.5	240	1625	11	5.6	21.6
4	26.8	2.5	0.2	0.45	170	301	11	5.6	21.1
5	30	2.5	1	0.45	170	301	11	5.6	21.1
6	57	8	1	0.35	110	367	8	5.6	22.3
7	76	12	1	0.3	100	733	8	5.6	-

B LIF concentration constants

Table 15: Source concentration C_0, maximum concentration $C_{\max}$ and coefficients of the polynomial of $\alpha(x, y)$ as described in Equation (5.2) for all cases.

Case	1	2	3	4	5	6	7
C_0 [gr/L]	8.3×10^{-5}	10.8×10^{-5}	162.5×10^{-5}	30.1×10^{-5}	30.1×10^{-5}	36.7×10^{-5}	73.3×10^{-5}
$C_{\max}$ [gr/L]	2×10^{-5}	2×10^{-5}	2×10^{-5}	7.5×10^{-5}	7.5×10^{-5}	4.5×10^{-5}	15×10^{-5}
p_{00}	1.805×10^{-8}	1.949×10^{-8}	4.279×10^{-8}	-8.257×10^{-8}	-1.228×10^{-7}	-4.492×10^{-7}	2.154×10^{-6}
p_{10}	-4.028×10^{-8}	-9.48×10^{-8}	-5.15×10^{-7}	1.109×10^{-8}	1.412×10^{-6}	2.452×10^{-6}	-8.199×10^{-6}
p_{01}	-2.376×10^{-8}	-1.265×10^{-7}	-1.872×10^{-7}	3.064×10^{-7}	3.915×10^{-7}	6.623×10^{-8}	-2.338×10^{-6}
p_{20}	-7.937×10^{-8}	2.276×10^{-7}	2.917×10^{-6}	-4.456×10^{-6}	-5.024×10^{-6}	-4.378×10^{-6}	1.042×10^{-5}
p_{11}	1.02×10^{-6}	2.18×10^{-6}	2.064×10^{-6}	-2.497×10^{-6}	-2.826×10^{-6}	-2.909×10^{-7}	6.002×10^{-6}
p_{02}	5.228×10^{-7}	1.022×10^{-6}	8.583×10^{-7}	-1.187×10^{-6}	-1.332×10^{-6}	2.027×10^{-7}	8.974×10^{-7}
p_{30}	2.167×10^{-6}	7.595×10^{-7}	-5.264×10^{-7}	5.926×10^{-6}	5.926×10^{-6}	2.594×10^{-6}	-4.395×10^{-6}
p_{21}	6.948×10^{-6}	-9.334×10^{-6}	-5.251×10^{-6}	5.14×10^{-6}	5.14×10^{-6}	2.904×10^{-7}	-4.11×10^{-6}
p_{12}	-5.687×10^{-6}	-8.157×10^{-6}	-1.932×10^{-6}	4.521×10^{-6}	4.521×10^{-6}	-3.944×10^{-7}	2.79×10^{-7}
p_{03}	-5.202×10^{-6}	-4.021×10^{-6}	-4.685×10^{-6}	2.411×10^{-6}	2.411×10^{-6}	3.544×10^{-7}	-2.585×10^{-6}

Table 16: Source concentration C_0, maximum concentration $C_{\max}$ and coefficients of the polynomial of $\alpha(x, y)$ as described in Equation (5.2) for the measurements with the moving camera.

Case	Moving
C_0 [gr/L]	33.3×10^{-5}
$C_{\max}$ [gr/L]	5e-4
p_{00}	1.721×10^{-7}
p_{10}	-4.206×10^{-7}
p_{01}	-6.507×10^{-8}
p_{20}	2.967×10^{-7}
p_{11}	1.667×10^{-7}
p_{02}	-3.636×10^{-7}
p_{30}	2.427×10^{-8}
p_{21}	-2.884×10^{-7}
p_{12}	1.555×10^{-6}
p_{03}	-1.425×10^{-6}

References

[1] N. Abdolrahimi and A. Tadjarodi. Adsorption of Rhodamine-B from Aqueous Solution by Activated Carbon from Almond Shell. In The 23rd International Electronic Conference on Synthetic Organic Chemistry, page 51, Basel Switzerland, nov 2019. MDPI.

[2] R. J. Adrian and J. Westerweel. Particle Image Velocimetry. Cambridge University Press, 2011.

[3] M. S. Alsoufi and A. E. Elsayed. Surface Roughness Quality and Dimensional Accuracy—A Comprehensive Analysis of 100% Infill Printed Parts Fabricated by a Personal/Desktop Cost-Effective FDM 3D Printer. Materials Sciences and Applications, 09(01):11–40, 2018.

[4] A. Attili, J. C. Cristancho, and F. Bisetti. Statistics of the turbulent / non-turbulent interface in a spatially developing mixing layer. Journal of Turbulence, 15(9):555–568, 2014.

[5] D. K. Bisset, J. C. R. Hunt, and M. M. Rogers. The turbulent/non-turbulent interface bounding a far wake. Journal of Fluid Mechanics, 451:383–410, 2002.

[6] B. J. Boersma, G. Brethouwer, and F. T. M. Nieuwstadt. A numerical investigation on the effect of the inflow conditions on the self-similar region of a round jet. Physics of Fluids, 10(4):899–909, 1998.

[7] M. Breda and O. R. H. Buxton. Behaviour of small-scale turbulence in the turbulent/non-turbulent interface region of developing turbulent jets. Journal of Fluid Mechanics, 879:187–216, 2019.

[8] G. Cafiero and J. C. Vassilicos. Non-equilibrium Scaling of the Turbulent-Nonturbulent Interface Speed in Planar Jets. Physical Review Letters, 125(17):174501, 2020.

[9] Carl Roth GmbH & Co. Safety data sheet Rhodamine B (C.I. 45170) for microscopy, 2019.

[10] Mitutoyo Co. Quick Guide to Precision Measuring Instruments.

[11] M. C. J. Coolen, R. N. Kieft, C. C. M. Rindt, and A. A. Van Steenhoven. Application of 2-D LIF temperature measurements in water using a Nd:YAG laser. Experiments in Fluids, 27(5):420–426, 1999.

[12] C. B. Da Silva, J. C. R. Hunt, I. Eames, and J. Westerweel. Interfacial layers between regions of different turbulence intensity. Annual Review of Fluid Mechanics, 46:567–590, 2014.

[13] V. da Silva Lacerda, J. B. López-Sotelo, A. Correa-Guimarães, S. Hernández-Navarro, M. Sánchez-Báscones, L. M. Navas-Gracia, P. Martín-Ramos, and J. Martín-Gil. Rhodamine B removal with activated carbons obtained from lignocellulosic waste. Journal of Environmental Management, 155:67–76, may 2015.

[14] J. Eisma. Pollutant dispersion in wall-bounded turbulent flows and experimental assesment. TU Delft University, page 289, 2017.

[15] D. A. Faux and J. Godolphin. Manual timing in physics experiments: Error and uncertainty. American Journal of Physics, 87(2):110–115, 2019.

[16] C. Fukushima, L. Aanen, and J. Westerweel. Investigation of the mixing process in an axisymmetric turbulent jet using PIV and LIF. Laser Techniques for Fluid Mechanics, pages 339–356, 2002.

[17] M. Gampert, V. Narayanaswamy, P. Schaefer, and N. Peters. Conditional statistics of the turbulent/non-turbulent interface in a jet flow. Journal of Fluid Mechanics, 731:615–638, sep 2013.

[18] F. Giralt, C. J. Chia, and O. Trass. Characterization of the Impingement Region in an Axisymmetric Turbulent Jet. Industrial and Engineering Chemistry Fundamentals, 16(1):21–28, 1977.

[19] L. H. O. Hellström, M. B. Zlatinov, A. J. Smits, and G. Cao. Turbulent pipe flow through a 90° bend. 7th International Symposium on Turbulence and Shear Flow Phenomena, TSFP 2011, 2011-July:1–6, 2011.

[20] M. Holzner, A. Liberzon, N. Nikitin, B. Lüthi, W. Kinzelbach, and A. Tsinober. A Lagrangian investigation of the small-scale features of turbulent entrainment through particle tracking and direct numerical simulation. Journal of Fluid Mechanics, 598:465–475, 2008.

[21] H. J. Hussein, S. P. Capp, and W. K. George. Velocity measurements in a high-Reynolds-number, momentum-conserving, axisymmetric, turbulent jet. Journal of Fluid Mechanics, 258:31–75, 1994.

[22] J. Kestin, M. Sokolov, and W. A. Wakeham. Viscosity of liquid water in the range -8°C to 150°C. Journal of Physical and Chemical Reference Data, 7(3):941–948, 1978.

[23] M. Khashehchi, A. Ooi, J Soria, and I. Marusic. Evolution of the turbulent/non-turbulent interface of an axisymmetric turbulent jet. Experiments in Fluids, 54(1):1449, jan 2013.

[24] D. Krug, M. Holzner, B. Lüthi, M. Wolf, A. Tsinober, and W. Kinzelbach. A combined scanning PTV/LIF technique to simultaneously measure the full velocity gradient tensor and the 3D density field. Measurement Science and Technology, 25(6), 2014.

[25] P. Lavoie, G. Avallone, F. De Gregorio, G. P. Romano, and R. A. Antonia. Spatial resolution of PIV for the measurement of turbulence. Experiments in Fluids, 43(1):39–51, jul 2007.

[26] Lenntech. Horizontal stage electric pumps. OP series., 2013.

[27] J. Mathew and A. J. Basu. Some characteristics of entrainment at a cylindrical turbulence boundary. Physics of Fluids, 2065(14), 2002.

[28] N. O. Mchedlov-Petrosyan and Y. V. Kholin. Aggregation of Rhodamine B in Water. Russian Journal of Applied Chemistry, 77(3):414–422, mar 2004.

[29] K. J. Mcnaughton and C. G. Sinclair. Submerged jets in short cylindrical flow vessels. Journal of Fluid Mechanics, 25(2):367–375, 1966.

[30] D. Mistry, J. Philip, and J. R. Dawson. Kinematics of local entrainment and detrainment in a turbulent jet. Journal of Fluid Mechanics, 871:896–924, 2019.

[31] D. Mistry, J. Philip, J. R. Dawson, and I. Marusic. Entrainment at multi-scales across the turbulent/non-turbulent interface in an axisymmetric jet. Journal of Fluid Mechanics, 802:690–725, 2016.

[32] F. T. M. Nieuwstadt, B. J. Boersma, and J. Westerweel. Turbulence, introduction to Theory and Applications of Turbulent Flows. Springer, 2015.

[33] N. R. Panchapakesan and J. L. Lumley. Turbulence Measurements in Axisymmetric Jets of Air and Helium. Journal of Fluid Mechanics, 246:225–247, 1993.

[34] R. Paranjape. Fundamental Enhancement Techniques. In Handbook of Medical Image Processing and Analysis, pages 3–18. Elsevier, second edition, 2009.

[35] S. B. Pope. Turbulent Flows. Cambridge University Press, 2000.

[36] R. R. Prasad and K. R. Sreenivasan. Scalar interfaces in digital images of turbulent flows. Experiments in Fluids, 7(4):259–264, 1989.

[37] J. Reijtenbagh. The organization of scalar mixing by coherent structures. Master's thesis, 2020.

[38] J. Reijtenbagh, J. Westerweel, and W. Van De Water. Large-scale structures of scalar and velocity in a turbulent jet flow. Physical Review Fluids, 6(8), 2021.

[39] W. Rodi. A new method of analysing hot-wire signals in highly turbulent flow, and its evaluation in a round jet. DISA Information, 17, 1975.

[40] A. I. Ruban and K. N. Vonatsos. Discontinuous solutions of the boundary-layer equations. Journal of Fluid Mechanics, 614:407–424, 2008.

[41] P. Saarenrinne and M. Piirto. Turbulent kinetic energy dissipation rate estimation from PIV velocity vector fields. Experiments in Fluids, 29(7):S300–S307, 2000.

[42] C. B. Silva and R. R. Taveira. The thickness of the turbulent / nonturbulent interface is equal to the radius of the large vorticity structures near the edge of the shear layer. Physics of Fluids, 121702(2010), 2010.

[43] T. S. Silva, M. Zecchetto, and C. B. da Silva. The scaling of the turbulent/non-turbulent interface at high Reynolds numbers. Journal of Fluid Mechanics, 843:156–179, may 2018.

[44] Inc. Spectra-Physics Lasers. Pulsed Nd: YAG Laser for Particle Image Velocimentry, 1997.

[45] H. Tennekes and J. L. Lumley. A first course in Turbulence. The MTI press, 1972.

[46] S. Tokgoz, G. E. Elsinga, R. Delfos, and J. Westerweel. Spatial resolution and dissipation rate estimation in Taylor–Couette flow for tomographic PIV. Experiments in Fluids, 53(3):561–583, sep 2012.

[47] C. Tropea, A. Yarin, and J. Foss. Handbook of Experimental Fluid Mechanics. Springer, 2007.

[48] J. S. Turner. The 'starting plume' in neutral surroundings. Journal of Fluid Mechanics, 13(January):356–368, 1962.

[49] J. S. Turner. Turbulent entrainment: the development of the entrainment assumption, and its application to geophysical flows. Journal of Fluid Mechanics, 173:431–471, 1986.

[50] D. A. Walker. A fluorescence technique for measurement of concentration in mixing liquids. Journal of Physics E: Scientific Instruments, 20(2):217–224, 1987.

[51] J. Wallace and J. F. Foss. The Measurement of Vorticity in Turbulent Flows. Annual Review of Fluid Mechanics, 27(1):469–514, jan 1995.

[52] T. Watanabe, Y. Sakai, K. Nagata, Y. Ito, and T. Hayase. Enstrophy and passive scalar transport near the turbulent/non-turbulent interface in a turbulent planar jet flow. Physics of Fluids, 26(10), 2014.

[53] J. Westerweel, C. Fukushima, J. M. Pedersen, and J. C. R. Hunt. Mechanics of the turbulent-nonturbulent interface of a jet. Physical Review Letters, 95(17):1–4, 2005.

[54] J. Westerweel, C. Fukushima, J. M. Pedersen, and J. C. R. Hunt. Momentum and scalar transport at the turbulent/non-turbulent interface of a jet. Journal of Fluid Mechanics, 631:199–230, 2009.

[55] J. Westerweel, T. Hofmann, C. Fukushima, and J. Hunt. The turbulent/non-turbulent interface at the outer boundary of a self-similar turbulent jet. Experiments in Fluids, 33(6):873–878, dec 2002.

[56] J. Westerweel and F. Scarano. Universal outlier detection for PIV data. Experiments in Fluids, 39(6):1096–1100, 2005.

[57] F. M. White. Fluid Mechanics 7th edition. McGraw Hill, 2011.

[58] I. Wygnanski and H. Fiedler. Some measurements in the self-preserving jet. Journal of Fluid Mechanics, 38(3):577–612, 1969.